

UC Santa Barbara

UC Santa Barbara Electronic Theses and Dissertations

Title

What Causes Ultrahigh-Temperature Metamorphism? A Case Study from Southern Madagascar

Permalink

<https://escholarship.org/uc/item/4d6588c3>

Author

Holder, Robert M.

Publication Date

2018

Supplemental Material

<https://escholarship.org/uc/item/4d6588c3#supplemental>

Peer reviewed|Thesis/dissertation

UNIVERSITY OF CALIFORNIA

Santa Barbara

What Causes Ultrahigh-Temperature Metamorphism? A Case Study from Southern
Madagascar

A dissertation submitted in partial satisfaction of the
requirements for the degree Doctor of Philosophy
in Earth Science

by

Robert McCarley Holder

Committee in charge:

Professor Bradley Hacker, Chair

Professor John Cottle

Professor Roberta Rudnick

Professor Frank Spera

September 2018

The dissertation of Robert McCarley Holder is approved.

John Cottle

Roberta Rudnick

Frank Spera

Bradley Hacker, Committee Chair

June 2018

What Causes Ultrahigh-Temperature Metamorphism? A Case Study from Southern
Madagascar

Copyright © 2018

by

Robert McCarley Holder

ACKNOWLEDGEMENTS

This dissertation would not have been possible without the extensive support of my wife and fellow graduate students. Thank you.

VITA OF ROBERT MCCARLEY HOLDER

June 2018

EDUCATION

Bachelor of Arts in Geology, Gustavus Adolphus College, May 2012 (summa cum laude)

Bachelor of Arts in Scandinavian Studies, Gustavus Adolphus College, May 2012

(summa cum laude)

Master of Science in Earth Science, University of California, Santa Barbara, June 2014

Doctor of Philosophy in Earth Science, University of California, Santa Barbara,

September 2018 (expected)

PROFESSIONAL EMPLOYMENT

2009: Field Technician, Great Basin Unified Air Pollution Control District

2010: Inductively-Coupled-Plasma Mass Spectrometry Intern, Gustavus Adolphus College

2009–2012: Teaching Assistant, Gustavus Adolphus College

2016: Teaching Associate, University of California, Santa Barbara

2012–2018: Teaching Assistant, University of California, Santa Barbara

2018–2020 (planned): Postdoctoral Fellow, Johns Hopkins University

PUBLICATIONS

Holder, R.M. (in preparation). Book Review: *Petrochronology: Methods and Applications*,

Reviews in Mineralogy and Geochemistry Volume 83 (2017) edited by Kohn, M. J.,

Engi, M., Lanari, P.

- Holder, R. M., Hacker, B. R., Horton, F., Rakotondrazafy, A. F. M. (2018). Ultrahigh - temperature osumilite gneisses in southern Madagascar record combined heat advection and high rates of radiogenic heat production in a long - lived high - temperature orogen. *Journal of metamorphic Geology*. doi:10.1111/jmg.12316.
- Peřestý, V., Lexa, O., Holder, R. M., Jerabek, P., Racek, M., Štípská, P., Schulmann, K., Hacker, B. (2016). Metamorphic inheritance of Rheic passive margin evolution and its early Variscan overprint in the Teplá-Barrandian Unit, Bohemian Massif. *Journal of Metamorphic Geology*. doi:10.1111/jmg.12234.
- P. Štípská, P., Powell, R., Hacker, B., Holder, R. M., Kylander-Clark, A. R. C. (2016). Uncoupled U/Pb and REE response in zircon during the transformation of eclogite to mafic and intermediate granulite (Blanský les, Bohemian Massif). *Journal of Metamorphic Geology*. doi:10.1111/jmg.12193.
- Horton, F., Hacker, B., Kylander-Clark, A. R. C., Holder, R. M., Jöns, N. (2016). Focused radiogenic heating of middle crust caused ultrahigh temperatures in southern Madagascar. *Tectonics*. doi:10.1002/2015TC004040.
- Holder, R.M., Hacker, B. R., Kylander-Clark, A. R. C., Cottle, J.M. (2015). Monazite trace-element and isotopic signatures of (ultra)high-pressure metamorphism: examples from the Western Gneiss region, Norway. *Chemical Geology*. doi:10.1016/j.chemgeo.2015.04.021.
- Hacker, B. R., Kylander-Clark, A. R. C., Holder, R. M., Andersen, T., Peterman, E., Walsh, E., Munnikhuis, J. (2015). Monazite response to ultrahigh-pressure subduction from U–

Pb dating by laser-ablation split-stream ICP-MS. *Chemical Geology*.
doi:10.1016/j.chemgeo.2015.05.008.

Štípská, P., Hacker, B. R., Racek, M., Holder, R. M., Kylander-Clark, A. R. C., Schulmann, K., Hasalová, P. (2015). Monazite Dating of Prograde and Retrograde P–T–d paths in the Barrovian terrane of the Thaya window, Bohemian Massif. *Journal of Petrology*.
doi:10.1093/petrology/egv026.

Broussolle, A., Štípská, P., Lehmann, J., Schulmann, K., Hacker, B. R., Holder, R. M., Kylander-Clark, A. R. C., Hanzl, P., Racek, M., Hasalová, P., Lexa, O., Hrdličková, K., Buriánek, D. (2015). P–T–t–D record of crustal-scale horizontal flow and magma assisted doming in the SW Mongolian Altai. *Journal of Metamorphic Petrology*.
doi: 10.1111/jmg.12124.

AWARDS

Postdoctoral Fellow, Johns Hopkins University, 2018

UCSB Doctoral Student Travel Grant, 2017

Outstanding Student Poster Award, EGU 2017

UCSB Alumni Graduate Award in Research Excellence, 2017

UCSB Earth Science Graduate Student Opportunity Award, 2017

UCSB ERI Summer Research Fellowship, 2017

Tanya Atwater Global Field Travel Fund, UCSB, 2016

George Tunell Memorial Fellowship, UCSB, 2016

Microanalysis Society Early Career Scholar Award, 2016

United States Antarctic Service Medal, 2015

Lloyd & Mary Edwards Field Studies Fellowship, UCSB, 2015

Tanya Atwater Global Field Travel Fund, UCSB, 2015

Imperial Barrel Award Competition, UCSB team, PSAAPG, 2014

UCSB Earth Science Graduate Award for Research Excellence, 2014

Sigma Xi Scientific Research Society, 2012

Undergraduate Speaker, Phi Beta Kappa Annual Meeting, Gustavus Adolphus College, 2012

Phi Beta Kappa Academic Honor Society, 2011

Chester O. Johnson Geology Scholarship, Gustavus Adolphus College, 2010

ABSTRACT

What Causes Ultrahigh-Temperature Metamorphism? A Case Study from Southern Madagascar

by

Robert McCarley Holder

This dissertation is an attempt to gain a better understanding of the tectonic significance of a particular subset of metamorphic rocks—ultrahigh-temperature metamorphic rocks—that are prevalent throughout Earth’s history, but for which there is no consensus as to how they form. The dissertation consists of three chapters: (1) a case study of an ultrahigh-temperature terrane exposed in southern Madagascar, (2) the development of a new technique for calculating the maximum temperatures reached by a metamorphic rock—one of the most fundamental data types upon which tectonic interpretations are made—based on the oxygen-isotope composition of minerals within the rock, and (3) an empirical evaluation of how quickly elements diffuse in the mineral titanite to gain a better understanding of the geological significance of U–Pb titanite dates obtained from high-temperature rocks. Ultrahigh-temperature metamorphism in southern Madagascar is found to have been the result of combined magmatic advection, high rates of radiogenic heat production, and a thin mantle lithosphere. Peak temperatures of metamorphism can be recovered from the oxygen isotope compositions of minerals so long as one of the minerals has a sufficiently high

closure temperature (such as garnet or sillimanite). Elemental diffusion in titanite is sufficiently slow that U–Pb dates likely reflect the time and conditions of titanite (re)crystallization, not cooling ages, in all but the highest grade rocks. Data tables referenced in the main text are available as spreadsheets in the supplementary materials accompanying this dissertation.

TABLE OF CONTENTS

INTRODUCTION.....	1
CHAPTER 1: WHAT CAUSES ULTRAHIGH-TEMPERATURE METAMORPHISM? A CASE STUDY FROM THE ANOSYEN DOMAIN OF SOUTHERN MADAGASCAR	5
CHAPTER 2: <i>LinT</i>, A SIMPLIFIED APPROACH TO OXYGEN-ISOTOPE THERMOMETRY AND SPEEDOMETRY OF HIGH-GRADE ROCKS	50
CHAPTER 3: INTERPRETING TITANITE U–Pb DATES AND Zr THERMOMETRY; EMPIRICAL CONSTRAINTS ON ELEMENTAL DIFFUSIVITIES OF Pb, Al, Fe, Zr, Nb, AND Ce.....	61
APPENDICES.....	103
BIBLIOGRAPHY	110

INTRODUCTION

Granulite-facies and ultrahigh-temperature metamorphism (UHTM: $>900^{\circ}\text{C}$ in the granulite facies) represent the thermal limit of processes within Earth's crust (Kelsey & Hand, 2015). Due to the large volumes of granitic melt that can be generated during UHTM (Bea, 2012), understanding how UHT terranes form is fundamental to understanding 1) how crust differentiates (Sawyer, Cesare, & Brown, 2011) and 2) how lithosphere is weakened during (Nelson et al., 1996) and strengthened after (Sandiford & McLaren, 2002; Sandiford, McLaren, & Neumann, 2002) orogenesis. UHTM has been reported in Archean through Cenozoic rocks (Brown, 2006) and is thought to be occurring in the mid to lower crust of Tibet today (Hacker et al., 2000; Hacker, Ritzwoller, & Xie, 2014). Despite the ubiquity of UHTM in the geologic record, the relative importance of processes that led to UHTM in individual terranes is often unclear.

UHTM has been attributed to advection of heat through asthenospheric upwelling, juvenile magmatism, and/or lithospheric extension; these processes are inferred to occur in arcs and back-arcs (Bohlen, 1987; Brown, 2006; Kemp, Shimura, & Hawkesworth, 2007; Pownall, 2014; Sandiford & Powell, 1986). Rigorously assessing the role of these heat sources in ancient rocks is difficult because of their inherent transience. Direct support for advective heating comes from exposed UHT rocks in the still-active arc of Japan (Kemp et al., 2007) and UHT rocks associated with Miocene-to-Recent lithospheric extension in Indonesia (Pownall, 2014). Indirect support comes from UHTM inferred at depth from high heat-flow measurements in back-arcs and in continental crust undergoing extension (Hyndman, Currie, & Mazzotti, 2005; Sandiford & Powell, 1986).

UHTM can also occur from heat sources internal to the crust. UHTM can occur if the crust has high concentrations of radioactive elements and is thick for a prolonged period (>40 Myr: Bea, 2012; Clark et al., 2015; Horton, Hacker, Kylander-Clark, Holder, & Jöns, 2016; Jaupart, Mareschal, & Iarotsky, 2016). In this case, no high-temperature magmatism is required. Support for this hypothesis includes ongoing UHTM in the middle to lower crust of modern central Tibet (Hacker et al., 2000, 2014), long UHT durations (40–100 Myr: e.g., Harley, 2016), and an apparent correlation of UHTM with supercontinent amalgamation (Brown, 2006). UHTM might also occur as a result of strain heating in shear zones (Nabelek, Whittington, & Hofmeister, 2010; Whittington, Hofmeister, & Nabelek, 2009), but strain heating is generally thought to be incapable of causing regional UHTM on its own due to the anticorrelation between rock strength and temperature, the anticorrelation between strength and degree of melting, and the tendency for strain to be partitioned into weaker layers where strain heating is less effective (Clark, Fitzsimons, Healy, & Harley, 2011).

Chapter 1 of this dissertation combines petrography, phase equilibria, and geochronology of a UHT terrane in southern Madagascar—the Ediacaran–Cambrian Anosyen Domain—with numerical modeling of heat flow to address the fundamental question: *What causes ultrahigh-temperature metamorphism?* A correlation between terrane-scale radiogenic heat-production rate and metamorphic T/P indicates that the distribution of U, Th, and K was a primary control on regional metamorphic grade. Thermal modeling suggests that average crustal heat-production rates must have been $>3 \mu\text{W}/\text{m}^3$ and that the mantle lithosphere must have been relatively thin ($< 80 \text{ km}$) in order to explain the P - T - t path recorded by the gneisses: peak conditions of $\sim 930^\circ\text{C}/0.6 \text{ GPa}$ after 20–40 Myr of prograde metamorphism. Advection of heat by high-temperature magmatism may also have been

important locally. Evidence supporting a component of advective heating includes: 1) the spatial coincidence of osumilite gneisses around the voluminous Anosyen Batholith, a batholith of relatively high-temperature felsic plutons, at least some of which were emplaced during prograde to peak metamorphism in the surrounding gneisses; 2) a short duration of prograde metamorphism (20–40 Myr); and 3) the low pressures (c. 0.6 GPa) inferred for prograde metamorphism.

Chapter 2 addresses the question: *How can peak metamorphic temperatures be calculated?* In this chapter, a new method of thermometry is proposed based on equilibrium fractionation of oxygen isotopes and a mass balance of oxygen among minerals. Accurate and precise temperatures of metamorphism and magmatism can be obtained from oxygen-isotope compositions of minerals using a system of linear equations that defines the fractionation and mass balance of oxygen isotopes among all minerals in a rock. This mathematical approach—linear-equation thermometry, “*LinT*”—does not require that cooling rates or absolute oxygen-diffusion parameters be known. If oxygen diffusivities *are* known, closure temperatures for each phase can be calculated and inverted to determine a temperature-dependent cooling rate that is accurate to a factor of three. The highest and most precise temperatures will be preserved in rocks containing quartz and garnet, because oxygen diffuses slowly in garnet and garnet–quartz oxygen-isotope fractionation is large. The technique is most advantageous in rocks with low-variance mineral assemblages in which precise pseudosection analysis is not possible. Application of *LinT* to gneisses from Madagascar returns metamorphic temperatures of $927 \pm 31^\circ\text{C}$ or $1037 \pm 34^\circ\text{C}$ —depending on the quartz–garnet calibration used—consistent with Zr-in-rutile temperatures, feldspar-solvus temperatures, and pseudosections.

Chapter 3 uses the thermal history determined in Chapters 1 and 2 to calculate elemental diffusivities in titanite, one of the newest and most-promising petrochronometers. This chapter addresses the question: *What is the geological significance of U–Pb titanite dates and Zr-in-titanite thermobarometry in high-grade metamorphic and igneous rocks?* Elemental diffusivities of Zr, Nb, Ce, Al, Fe, and Pb in titanite were calculated as a function of the lengthscales of preserved compositional gradients in titanite grains from calc-silicate gneisses that equilibrated between 800–1000°C from southern Madagascar. The length scales of elemental diffusion were evaluated through (1) LA-ICP-MS and EPMA maps of a 0.5 cm titanite in thin section from a 900–1000°C gneiss, and (2) near-rim isotopic and compositional gradients measured by LA-ICP-MS and EPMA depth profiling of a 0.5 cm euhedral titanite from an ~800°C gneiss. In the 800°C titanite, the length scale of Pb diffusion is 5 µm and the length scales of Al-Fe-Zr-Nb-Ce diffusion are ≤ 1 µm. In the 900–1000°C titanite, the length scales of diffusion are: Al-Zr-Nb ~20, Ce 20–40, Fe 50–100, and Pb 200–300 µm. These length scales, combined with independent constraints on the thermal histories of the rocks, correspond to elemental diffusivities 2–4 orders of magnitude slower than determined from experiments. Considering the growing body of empirical studies suggesting extremely slow elemental diffusion in titanite, titanite dates and compositions should be assumed to reflect the conditions of (re)crystallization in all but the smallest grains in the hottest rocks unless evidence for diffusion can be shown. This chapter concludes by proposing that the differences in experimental and empirical estimates of elemental diffusion rates in titanite might be due to differences in the complexity of most titanite solid solutions relative to the near-pure CaTiSiO₅ used in experiments.

CHAPTER 1: WHAT CAUSES ULTRAHIGH-TEMPERATURE METAMORPHISM? A CASE STUDY FROM THE ANOSYEN DOMAIN OF SOUTHERN MADAGASCAR

1: THE ANOSYEN DOMAIN OF SOUTHERN MADAGASCAR

The Anosyen domain (Figure 1) is the southeasternmost and highest grade tectonic unit of the Malagasy basement. It is bounded by the Androyen domain to the west and the Ikalamavony domain to the north. It is composed of metapelitic, calc-silicate, and felsic paragneisses that were deposited in the Meso- to Neoproterozoic then metamorphosed and intruded by the Anosyen Batholith/Ambalavao suite between 590 and 510 Ma (e.g. GAF-BGR, 2008; Tucker, Roig, Moine, Delor, & Peters, 2014). Detrital zircon ages indicate that the Anosyen metasediments are likely correlative with other metasedimentary rocks exposed throughout central and northern Madagascar, south India, and Sri Lanka, suggesting a shared tectonic history of these regions prior to Ediacaran–Cambrian metamorphism (Boger et al., 2014). Metamorphism has been interpreted as the result of continental collision following closure of the Mozambique Ocean (“East African Orogeny” between India and east Africa) and/or the Mawson Ocean (“Kuunga Orogeny” between India–East-Africa and Antarctica: Boger et al., 2015; Collins & Windley, 2002; Meert & Lieberman, 2008; Tucker et al., 2014). The metamorphic and magmatic history of the Anosyen domain is presented in more detail below.

1.1: Metamorphism of the Anosyen sediments

Metamorphic U-Pb zircon and monazite dates from gneisses in the Anosyen Domain are 590–500 Ma with a mode at 540 Ma (Boger et al., 2014; GAF-BGR, 2008a; Giese, Berger, Schreurs, & Gnos, 2011; Horton et al., 2016; Jöns & Schenk, 2011; Martelat, Lardeaux, Nicollet, & Rakotondrazafy, 2000; Tucker, Roig, Macey, et al., 2011). These metamorphic dates are nearly identical to the dates from the granulites of southernmost India (Blereau et al., 2016; Clark et al., 2015; Johnson, Clark, Taylor, Santosh, & Collins, 2015; R. J. M. Taylor et al., 2014), interpreted to have been contiguous with southern Madagascar at the time. Horton et al. (2016) have also reported dates as old as 610 Ma in and near the Beraketa shear zone along the western margin of the domain, but the significance of these dates is unclear; dates older than 590 Ma within the domain are limited to a single SHRIMP zircon analysis in each of two samples described by Jöns and Schenk (2011) and two LA-ICP-MS zircon analyses from another sample described by Horton et al. (2016). A single Sm-Nd garnet–zircon–monazite–whole-rock isochron date of 588 ± 13 Ma (MSWD = 0.11) was reported for an Al-spinel–quartz leucogneiss collected near Tôlanaro (Paquette, Nédélec, Moine, & Rakotondrazafy, 1994). Martelat et al. (2000) conducted a targeted U/Th–Pb microprobe monazite dating campaign of rocks from within a variety of structural settings across south Madagascar. A regional, flat-lying “D1” granulite-facies fabric was inferred to have developed between 590 and 530 Ma and been locally overprinted by subvertical “D2” transpressional shear zones (still within the granulite facies) until sometime between 530 Ma and 510 Ma. Martelat et al. interpreted D1 and D2 to represent a “whole progressive deformation event,” rather than discrete periods of deformation. The timing of retrograde metamorphism and cooling is constrained by 550–520 Ma leucosomes and pegmatite dikes

interpreted to represent partial-melt crystallization (Collins, Kinny, & Razakamanana, 2012; Jöns & Schenk, 2011; Paquette et al., 1994; Tucker, Roig, Macey, et al., 2011), 537 ± 14 Ma monazite that co-crystallized with high-F apatite and biotite in m-scale veins at $750\text{--}800^\circ\text{C}$ at Manangotry Pass (Montel et al., 2018), a 453 ± 6 Ma Ar/Ar biotite date from Manangotry Pass (Montel et al., 2018), and Ar/Ar (480 ± 2 Ma) and Rb/Sr (492 ± 10 , 491 ± 10 Ma) phlogopite dates from meter-scale carbonatite bodies near Beraketa (Martelat, Randrianasolo, Schulmann, Lardeaux, & Devidal, 2014).

Previous investigations indicate that the Anosyen metasediments were metamorphosed between 0.4 and 1.1 GPa; with most studies suggesting c. 0.6 GPa. Peak temperatures were $>900^\circ\text{C}$ in the southern portion of the domain (Tranomaro–Tôlanaro area, Figure 1) and colder in the north by $50\text{--}100^\circ\text{C}$ (near and north of Ihosy, Figure 1: individual studies are outlined below). Most of the previous thermobarometric constraints are from the northern portion of the domain (near Ihosy) and along its western margin (the Beraketa shear zone), due to ease of access. The most-detailed thermobarometry of the interior of the domain was conducted by Boger, White, and Schulte (2012), who used pseudosections of three common rock types to infer peak temperatures of $880\text{--}920^\circ\text{C}$ near Tranomaro and 840°C near Ihosy. Boger et al. (2012) inferred a prograde path at 0.6–0.65 GPa, with 0.1 GPa of decompression near the peak temperature, based on inclusion relationships and preserved reaction textures among minerals.

Jöns and Schenk (2011) demonstrated the regional extent of high-grade metamorphism by reporting pseudomorphs after osumilite, sapphirine–quartz, spinel–quartz, and orthopyroxene–sillimanite–quartz assemblages. They used these assemblages to infer UHTM; however, fresh osumilite was not observed, and the presence of ferric iron—inferred

from magnetite and hemo-ilmenite assemblages—in the sapphirine–quartz, orthopyroxene–sillimanite–quartz, and many of the spinel–quartz rocks means that the precise thermal significance of these assemblages is unclear (Kelsey, 2008). Using experimentally calibrated thermobarometers, they interpreted peak conditions of 1000°C/1.0 GPa, followed by decompression and cooling to 800°C/0.5 GPa. Jöns and Schenk inferred that temperatures were lower near Ihosy than near Tranomaro based on a systematic south-to-north decrease in biotite and garnet Mg# ($\text{Mg}/[\text{Mg}+\text{Fe}]$) in biotite–garnet–sillimanite gneisses. They also estimated peak temperatures 900–1000°C based on reintegrated perthite compositions and the feldspar solution model of Fuhrman and Lindsley (1988).

Horton et al. (2016) calculated minimum temperatures from Ti in quartz and Zr in rutile. If $P = 1$ GPa (Jöns and Schenk, 2011; GAF-BGR, 2008) $T_{\text{quartz}} = 930^\circ\text{C}$ and $T_{\text{rutile}} = 970^\circ\text{C}$. If $P = 0.6$ GPa—the pressure reported by most studies— $T_{\text{quartz}} = 830^\circ\text{C}$ and $T_{\text{rutile}} = 940^\circ\text{C}$. Ti-in-quartz temperatures are minima, because a_{TiO_2} was assumed to be unity although rutile was not present in most of the samples. The Zr-in-rutile temperatures come from the Beraketa shear zone (Figure 1a), which defines the western margin of the domain; the interior of the domain might be expected to be hotter.

Martelat et al. (2012) determined the P - T conditions of equilibrium of a garnet leucogneiss within the Zazafotsy shear zone near Ihosy to be 800–950°C/0.9–1.1 GPa using two-feldspar thermometry (Benisek, Dachs, & Kroll, 2010; Benisek, Kroll, & Cemič, 2004; Fuhrman & Lindsley, 1988) and garnet–sillimanite–quartz–plagioclase barometry (TWEEQ). Both pressure and temperature may have been overestimated; recalculation of their GASP pressures using the THERMOCALC solution models and end-member mineral data (for direct comparison with Boger et al., 2012) and their feldspar temperatures using the solution

model of Benisek et al. (2010) (correcting for K-Na diffusion using the method of Kroll, Evangelakakis, and Voll (1993) for direct comparison with our results below) returns P - T conditions of 0.6–0.7 GPa and 750–850°C; these values are comparable to those suggested for the area near and north of Ihosy by Boger et al. (2012) and Raith, Rakotondrazafy, and Sengupta (2008).

Raith et al. (2008) calculated metamorphic conditions of 800°C/0.6–0.7 GPa from corundum–spinel–sapphirine–anorthite–phlogopite gneisses (“sakenites”) 75 km northwest of Ihosy, suggesting that the northern part of the Anosyen domain experienced lower peak temperatures, consistent with the interpretations of Boger et al. (2012) and Jöns and Schenk (2011).

Rakotonandrasana, Arima, Miyawaki, and Rambeloson (2010) calculated P - T conditions ranging from 880°C at 0.45 GPa to 1060°C at 0.65 GPa for högbomite–hematite-bearing pelitic rocks within the Anosyen domain just south of Ihosy using pseudosections and WinTWQ. They interpreted that the rocks experienced a component of decompression near peak temperature based on coronal relationships suggesting the reactions spinel + quartz → cordierite and garnet + sillimanite → cordierite + spinel, but did not quantify the magnitude of decompression. They neglected ferric iron in their pseudosections, an important component given the Fe³⁺-rich oxides in their rocks.

Ackermann (1991) calculated peak P - T conditions of 1 GPa and 950–980°C followed by decompression and cooling to 0.6 GPa and 800°C in silica-undersaturated sapphirine–cordierite–orthopyroxene rocks within the Beraketa shear zone, using the equilibria enstatite + sillimanite = sapphirine + cordierite, enstatite + sapphirine = cordierite + spinel, and the Al content of enstatite. They also reported metamorphic conditions of

750–950°C/0.5–0.6 GPa in metapelites near Ihosy and pressures of 0.45–0.55 GPa (no reported temperature) in garnet–cordierite–spinel gneisses near Tôlanaro.

Nicollet (1985) reported temperatures >700°C/0.5–0.55 GPa in metapelites near Ihosy using garnet-biotite and garnet–sillimanite–cordierite–quartz equilibria.

Rakotondrazafy, Moine, and Cuney (1996) recognized near-pure meionite in hibonite-bearing calc-silicate rocks near Tranomaro, implying temperatures >850°C. They also reported isochores of CO₂ fluid inclusions in corundum indicating *P-T* conditions of entrapment at 850°C/0.5 GPa. Inclusions in hibonite and anorthite indicate *P-T* conditions of entrapment at 800°C/0.35 GPa.

1.2: Magmatism within the Anosyen domain

The Anosyen domain contains two groups of plutonic rocks: the voluminous Anosyen Batholith (Figure 1; Paquette et al., 1994; part of the broader Ambalavao Suite in GAF-BGR, 2008) and dikes, pegmatites, leucosomes, and small plutons interpreted to be the result of small-volume, partial melt crystallization during cooling. Dates for dikes, pegmatites, leucosomes, and small plutons have been reported between 550 and 520 Ma and have been attributed to cooling of the terrane and associated partial melt crystallization (Collins et al., 2012; Jöns & Schenk, 2011; Paquette et al., 1994; Tucker, Roig, Delor, et al., 2011).

The Anosyen Batholith (Figure 1) contains “syn-“ to “post-tectonic” plutons of orthopyroxene granite to syenite, garnet (\pm spinel) granite to syenite, quartz monzonite, and one pluton of gabbro (GAF-BGR, 2008). It comprises 30–50 % of the basement exposed in the southeastern part of the Anosyen domain (GAF-BGR, 2008). GAF-BGR (2008) divided the batholith into a single, large “early” pluton and many smaller “late” plutons based on

whether the plutons were discordant to the granulite-facies foliation (“D1:”, loosely constrained between 590–530 Ma; Martelat et al. (2000).

Eight published U–Pb zircon and monazite dates for plutons in the Anosyen batholith range from 570 Ma to 520 Ma. GAF-BGR (2008) dated a concordant pluton at 573 ± 12 Ma and a discordant pluton at 521 ± 12 Ma (weighted mean SHRIMP $^{207}\text{Pb}/^{206}\text{Pb}$ date of youngest analyses; $^{206}\text{Pb}/^{238}\text{U}$ dates for *concordant* analyses range from 560 to 515 Ma) and considered these dates as representative of the “early” and “late” plutons in the batholith.

Paquette et al. (1994) reported ID-TIMS U–Pb intercept dates of 572 ± 14 Ma for the largest concordant body and 570 ± 3 Ma for each of two discordant orthopyroxene granites, suggesting both generations of plutons were emplaced at nearly the same time. These dates are upper intercepts of discordia that project through the origin in Wetherill concordia diagrams, consistent with Pb loss from portions of zircon grains that had experienced radiation damage: a common characteristic of U–Pb zircon data prior to the development of “chemical-abrasion” treatment (Mattinson, 2005). Sm–Nd isochrons from the same rocks provide dates in agreement with the U–Pb intercept dates: 565 ± 7 and 555 ± 24 Ma for the concordant and discordant bodies, respectively. Paquette et al. also collected zircon Pb-evaporation dates, which were generally younger (560–530 Ma), and were considered *minimum* emplacement dates for the orthopyroxene granites (see their discussion section). Martelat et al. (2000) reported U/Th–Pb monazite EPMA dates of 558 ± 12 , 536 ± 7 , and 523 ± 8 Ma from orthopyroxene granites; the two younger dates were obtained from bodies within “D2” shear zones.

2: OSUMILITE & AL-SPINEL–QUARTZ GNEISSES OF SOUTHERN MADAGASCAR

The samples presented in this study come from a 100x100 km area of the Anosyen domain, southeastern Madagascar, containing the Anosyen Batholith and the cities of Tranomaro, Tôlanaro, Amboasary, and Esira (Figure 1). Although the study area is large, pressure estimates from within the same area (0.5–0.65 GPa: Ackermann et al., 1989; Rakotondrazafy et al., 1996; Boger et al., 2012: section 1.1) suggest that all of the gneisses formed at nearly the same depth and record the same tectonic and thermal history. Coordinates of the sample localities used for thermobarometry and geochronology are provided in supplementary data Table S2.

2.1: Osumilite gneisses

I report the first observation of osumilite in Madagascar from sample 23A (Figure 2a). The presence of osumilite had been inferred (Jöns & Schenk, 2011) from the presence of cordierite–K-feldspar–quartz±orthopyroxene±biotite symplectites (Figures 2a–c). In most samples, these symplectites occur as near-equant 0.5–2 mm pseudomorphs within the matrix (Figure 2c) and as coronae that mantle other phases; the latter texture has been interpreted to reflect osumilite breakdown in the presence of partial melt (Korhonen, Brown, Clark, & Bhattacharya, 2013) and is consistent with the absence of orthopyroxene in most of the symplectites (Figure 2c; see Figure 7 in Korhonen et al., 2013). Similar symplectites have been observed in the “Bakika Formation” by Boger et al. (2012), although those authors did not interpret them to be the result of osumilite breakdown, because osumilite was not calculated to be stable in a pseudosection of that rock. The osumilite- and osumilite-

pseudomorph-bearing rocks of Madagascar have only been found adjacent to the Anosyen Batholith (Figure 1; Jöns and Schenk, 2011; this study). Unlike most osumilite-bearing rocks worldwide, the osumilite-bearing rocks of Madagascar do not contain orthopyroxene, except in some of the symplectites after osumilite. Two samples were chosen for pseudosection modeling and are described in more detail in the following paragraphs. Details of how the pseudosections were constructed are presented in section 3.2.

Sample 22H contains quartz, alkali-feldspar, plagioclase, Al-spinel (with magnetite exsolution, but magnetite does not occur as separate grains; 0–0.01 atoms per formula unit each of Zn, Cr, and Mn; see Table S2), ilmenite, cordierite, biotite and garnet. Silicate phases are typically 200–500 μm in diameter except in cordierite–K-feldspar–quartz symplectites after osumilite (Figure 2c) and coronae (Figure 2c–2g); spinel and ilmenite are typically 50–100 μm in diameter. Cordierite most commonly occurs as coronae around spinel, ilmenite, garnet, and less commonly, sillimanite. Equant cordierite also occurs in association with feldspars and quartz in the matrix. Plagioclase occurs as equant grains in the matrix and in worm-like intergrowths with quartz or alkali-feldspar; the latter are interpreted to be the result of melt crystallization. Alkali-feldspar contains exsolution lamellae of plagioclase, but plagioclase does not contain exsolution lamellae of alkali-feldspar. Biotite most commonly occurs rimming other mafic phases or as xenoblastic grains in the matrix. Garnet occurs as up to 1 mm xenoblastic grains with ubiquitous inclusions of Al-spinel (no Zn or Cr), quartz, and sillimanite (Figure 2d), as 100–200 μm coronae around Al-spinel (Figure 2e), and, in one location, as a partial corona around cordierite (Figure 2f). Outside garnet, sillimanite occurs as a matrix phase and as coronae around Al-spinel (Figure 2g).

Sample 23A is the only sample in which fresh osumilite was observed. Fresh osumilite occurs at the center of a 1.5 cm-wide fine-grained symplectite of alkali-feldspar, cordierite, quartz, orthopyroxene, and magnetite (Figures 2a and 2b). Orthopyroxene was only found in the symplectite immediately adjacent to the fresh osumilite; even adjacent to the osumilite, its presence is spatially restricted (Figure 2a). Orthopyroxene is not present near the spinel–quartz–sillimanite–feldspar matrix. The symplectite minerals are elongate perpendicular to the boundary of the fresh osumilite; abrupt changes in the orientations and modal proportions of minerals within the symplectite are inferred to be former osumilite grain boundaries. The fresh osumilite contains a single inclusion of magnetite (Figure 2a). Quartz, alkali-feldspar, magnetite, ilmenite, and monazite occur as inclusions within the fine-grained symplectite near the fresh osumilite; these phases are interpreted to have been former inclusions in osumilite. Biotite and coarser grained cordierite occur as xenoblastic grains and coronae around spinel, magnetite, and ilmenite that extend into the symplectite near its margins. Large zircon (200 μm) and a single monazite are associated with one biotite corona around a composite magnetite–ilmenite grain (Figure 9).

2.2: Al-spinel–quartz gneisses

The gneisses along the southeast coast of Madagascar (south and east of the Anosyen Batholith; Figure 1) consist mainly of leucogneiss dominated by a single ternary feldspar (now mesoperthite), quartz, and garnet with minor Al-spinel, ilmenite, and sillimanite (Figures 3 and 4). Spinel occurs mainly in intergrowths with quartz adjacent to garnet (Figures 3a and 3b), but also as isolated grains in the matrix. Magnetite exsolution is absent or makes up < 1 vol. % of the spinel in all samples of this rock type. Spinel is commonly

separated from quartz by 20–100 μm coronae of garnet, sillimanite, garnet–sillimanite, or plagioclase (Figures 3b–d). Cordierite coronae around garnet and spinel are present some samples, but not sample 18A used for pseudosection modeling. Biotite is a local retrograde phase around spinel and garnet. Plagioclase occurs as films along mesoperthite grain boundaries (Figure 4) and in intergrowths with quartz, suggesting growth from the exsolution of ternary feldspar and from melt crystallization. Garnet contains inclusions of alkali feldspar and quartz.

3: THERMOBAROMETRY

3.1: Feldspar thermometry

Minimum temperatures of metamorphism were calculated from reintegrated mesoperthite compositions and plagioclase films along mesoperthite grain boundaries in two hercynite–quartz gneisses (samples 18A and 18B: Figure 4). The solution model and Na–K exchange correction recommend by Benisek et al. (2010) were used. The pressure used in the calculations was 0.6 GPa. Analytical uncertainties on feldspar compositions were 0.5, 0.9, 0.5, 5.0, 0.5, 7.6, and 0.5% for $X_{\text{ab}}^{\text{pl}}$, $X_{\text{an}}^{\text{pl}}$, $X_{\text{ab}}^{\text{af}}$, $X_{\text{an}}^{\text{af}}$, $X_{\text{san}}^{\text{af}}$, $X_{\text{san}}^{\text{pl}}$, and $X_{\text{san}}^{\text{af}}$, respectively (see supplementary data Tables S2 and S3 for EPMA analyses). Calculations were done 2000 times by Monte Carlo simulation from plagioclase–reintegrated-mesoperthite compositional pairs. The temperatures and uncertainties reported below reflect the mode and 95% confidence interval of the Monte-Carlo simulation. Calculations in which the standard deviation of T_{ab} , T_{an} , and T_{san} never decreased below 10°C during the Na–K exchange correction were excluded (see Benisek et al. [2010] for explanation of T_{ab} , T_{an} , and T_{san}).

The four perthites from sample 18A returned temperatures of $882 \pm 45/-107$, $943 \pm 29/-48$, 899 ± 34 , and 913 ± 13 °C. The four perthites from sample 18B returned temperatures of $919 \pm 17/-30$, $927 \pm 28/-48$, 932 ± 23 , and $922 \pm 25/-31$ °C. All calculated temperatures agree between 910 and 930°C; this is a minimum temperature estimate for these rocks. Jöns and Schenk (2011) also present ternary feldspar thermometry temperatures: 900–1000°C using the solution model of Fuhrmann and Lindsley (1988). Their slightly higher temperatures are the result of lower miscibility in the Fuhrmann and Lindsley (1988) solution model, compared to the Benisek et al. (2010) model. For a discussion of the different feldspar solution models, see Benisek et al. (2010).

3.2: Phase-equilibria modeling

Pseudosections for two osumilite gneisses and one Al-spinel–quartz gneiss were constructed (Figures 5 and 6) using bulk compositions calculated from mineral modes in thin section, mineral molar volumes, and mineral compositions measured by EPMA (see supplementary data Table S4 for bulk compositions). Oxide components used in the calculations were Na₂O, CaO, K₂O, FeO, Fe₂O₃, MgO, MnO, Al₂O₃, SiO₂, TiO₂, and H₂O. Calculations were made using the gridded minimization algorithm of Perple_X 6.7.8 (Connolly, 2009). Diagrams were constructed using the mineral end-member thermodynamic database of Holland and Powell (2011). The ternary feldspar solution model used is from Benisek et al. (2010) to facilitate direct comparison with feldspar temperatures (section 3.1). The osumilite solution model used is that of Holland, Babu, & Waters (1996). Garnet, cordierite, silicate melt, biotite, and orthopyroxene are from White, Powell, Holland, Johnson, and Green (2014) and White, Powell, and Johnson (2014); ilmenite is from White, Powell, Holland, and Worley

(2000) with MgTiO_3 added as described by White, Powell, Holland, et al. (2014) and MnTiO_3 added as described by White, Powell, & Johnson (2014); spinel is from White, Powell, and Clarke (2002).

Elemental components not included in the osumilite, spinel, and biotite solution models:

EPMA measurements of osumilite in sample 23A indicate 0.01 atoms of Ti, 0.04 atoms of Mn, 0.06 atoms of Ca, and 0.01 atoms of Na per formula unit (30 oxygen; Table S2). The osumilite model of Holland et al. (1996) does not include Ti, Na, Ca, Mn, Fe^{3+} , or vacancies. The effects these components have on osumilite stability are not known and must be considered when interpreting the pseudosections of this manuscript. Experiments by Das, Dasgupta, and Miura (2001) in $\text{K}_2\text{O}\text{--FeO}\text{--Fe}_2\text{O}_3\text{--MgO}\text{--Al}_2\text{O}_3\text{--SiO}_2\text{--H}_2\text{O}$ suggest osumilite stability at high $f\text{O}_2$ is restricted to $>850^\circ\text{C}/<8.5$ kbar—similar to its stability at low $f\text{O}_2$ conditions (Carrington & Harley, 1995)—but whether Fe^{3+} is actually incorporated into osumilite in significant amounts remains unclear (see discussion by Das et al., 2001). The osumilite of sample 23A, in this study, has an average cation total of 18.07 for 30 oxygen; 0.4% higher than the expected 18 cations for the simplified osumilite solid solution used in the Holland et al. (1996) solution model. A higher than expected cation total may indicate that molecular weight was underestimated in the processing of EPMA measurements, possibly related to the additional oxygen bonded to ferric relative to ferrous iron. This argument, however, hinges on the assumption that osumilite should have exactly 18 cations per 30 oxygen. For natural osumilite, reported cation totals are typically slightly less than 18 (Armbruster & Oberhaesnsli, 1988; Berg & Wheeler, 1976; Chinner & Dixon, 1973; Olsen & Bunch, 1970); a notable exception are the osumilite reported by Arima and Gower (1991). Even the osumilite from the hematite-magnetite buffered experiments of Das et al. (2001),

have cation totals slightly less than 18; suggesting that cation totals are not a reliable method for estimating ferric iron content. Furthermore, most of the “excess” cations calculated for osumilite in sample 23A can be accounted for by the excess alkalis. The sum of sodium, potassium, and calcium is, on average, 1.04: the maximum occupancy of the 12-fold coordinated A site is unity. The excess alkali metals may be indicative of partial occupancy of an additional site—the B site—that has been suggested for other osumilite group minerals yagiite (Bunch & Fuchs, 1969), roederrite (Fuchs, Frondel, & Klein, 1966; Olsen, 1967), and merrihueite (Dodd, Schmus, & Marvin, 1965; see Berg & Wheeler, 1976). Finally, wt.% totals for osumilite in this study are 100.4 on average, suggesting that total molecular weight has been slightly overestimated, not underestimated. Despite the presence of hematite–ilmenite and spinel–magnetite solid solutions in sample 23A, the extent to which Fe^{3+} is accommodated in osumilite remains unclear.

Elemental components not included in the spinel solution model: The spinel–magnetite model of White et al. (2002) does not include Mn, Cr, or Zn. In sample 22H, Mn and Cr are 0.00–0.01 atoms per formula unit (apfu: four oxygen); in sample 23A, Mn was 0.01–0.02 apfu; and in sample 18A1 Zn was 0.01 apfu (Table S2). The effect of Zn on Al–spinel stability was studied experimentally by Nichols, Berry, and Green (1992). While Zn can greatly expand spinel’s stability to lower temperatures and higher pressures, the small amount of ZnAl_2O_4 in the spinel of this study is negligible considering the geological and numerical uncertainties in thermobarometry and phase equilibria; 0–0.01 mol.% corresponds to $<8^\circ\text{C}$ down-temperature shift in spinel–quartz stability. The effect of Mn and Cr on spinel stability is not known, but likely to be similarly negligible considering their low concentrations. Together, the spinel–quartz stability calculations and feldspar thermometry

provide independent P - T estimates from those constrained by the osumilite stability calculations.

Elemental components not included in the biotite solution model: Fluorine can increase the stability of biotite to higher temperature (Dooley & Patiño Douce, 1996; Finch & Tomkins, 2017; Motoyoshi & Hensen, 2001), but is not included in the solution model of White, Powell, Holland, et al. (2014). In all modeled samples, biotite occurs as coronae around other mafic phases or as xenoblastic grains in the matrix and is interpreted to be exclusively retrograde in these samples; the P - T interpretations of this study do not rely on reactions involving biotite.

Samples chosen for pseudosections: Two samples of osumilite gneiss were modeled. 1) Sample 22H was chosen because of its relatively low ferric iron content compared to the other osumilite-bearing rocks; there is no magnetite other than exsolution lamellae in spinel and there is no hematite exsolution in ilmenite. 2) Sample 23A was chosen because it is the only sample with fresh osumilite. The ferric iron contents of samples 22H and 23A were estimated from the observed modes and compositions of mafic phases. These values were then adjusted iteratively during the construction of the pseudosections until the approximate measured oxide compositions were reproduced at the inferred peak P - T conditions. For 22H, this resulted in $\text{Fe}^{3+}/\text{Fe}^{\text{total}} = 0.1$; for 23A, 0.25. To test the sensitivity of the outputs to different ferric iron contents, pseudosections were calculated at half and twice the values described above; the main effects were changes in the lower-temperature stability limit of Al-spinel and reactions involving ilmenite outside the P - T conditions relevant to the rock. The key relationships of osumilite \pm garnet were affected by less than 0.1 GPa and 25°C (see Figure 5b). As discussed above, and again below, the results of osumilite-bearing

pseudosections are limited by the lack of Fe^{3+} , Mn, Ca, Na, and Ti in the osumilite solution model.

Of the hercynite–quartz gneisses, sample 18A was chosen for pseudosection modeling because it lacks retrograde cordierite and therefore provides a low-pressure constraint on the retrograde P - T path. Furthermore, the spinel contains no magnetite exsolution, <0.01 mol. % ZnAl_2O_4 , and no measurable Cr, indicating that its stability should be well described by the spinel solution of White et al. (2000). Ilmenite is end-member FeTiO_3 , corroborating the lack of ferric iron in the rock.

The H_2O content in all calculations, was set such that the silicate melt was c. 10 vol. % at the inferred peak P - T conditions; this was approximately 0.5 mol. % H_2O for all rocks. Due to these low H_2O contents, the lower-temperature mineral assemblages in the initial pseudosection calculations were melt absent. To better illustrate the potential prograde phase equilibria (prior to melt extraction), the portions of the diagrams at lower temperature were recalculated both by reintegrating melt (as described by Korhonen et al., [2013]) and by simply increasing the bulk-rock water content until the entire diagrams became melt saturated. The results of both methods were nearly identical, because the two most abundant components of the reintegrated silicate melt were, by far, H_2O and SiO_2 ; the additional SiO_2 has no effect on the phase equilibria, because the modeled assemblages are already saturated in SiO_2 . This is consistent with the findings of Bartoli (2017) who tested different methods of melt reintegration and found that the stability limits of phases were similar in all calculations. The phase equilibria at temperatures lower than the low- H_2O solidi in Figures 5 and 6 (bold dash-dot lines; referred to as residual solidi elsewhere) were obtained by increasing the bulk-rock water content, as this was both a simpler and more objective calculation. The amount of

water required to saturate the full diagrams with melt was 2–3 mol. %. Although these calculations illustrate potential prograde phase relationships, no detailed inferences about the low-temperature P - T path of the rocks is made in this study due to a lack of definitively prograde mineral relationships.

3.2.1: Pressure-temperature path

Pressure–temperature path inferred from pseudosections: The peak temperature reached by sample 18A (Al-spinel–quartz gneiss) is constrained by the stability of one ternary feldspar + spinel: $>910^{\circ}\text{C}$ (Figures 5c). The peak P - T conditions reached by sample 22H (osumilite–garnet gneiss) are constrained by the stability of osumilite–garnet–spinel: 925 – $1050^{\circ}\text{C}/0.4$ – 0.7 GPa (Figures 5a). The peak P - T conditions reached by sample 23A (fresh osumilite gneiss) are constrained by the stability of osumilite without garnet: $>940^{\circ}\text{C}/<0.6$ GPa (Figures 5c). The inferred peak-temperature mineral assemblages in pseudosections of all samples overlap in the range of 940 – $1050^{\circ}\text{C}/0.4$ – 0.6 GPa (Figure 6a).

The dominant coronal relationships preserved in the osumilite and Al-spinel–quartz gneisses consist of garnet and sillimanite mantling Al-spinel and are interpreted to be indicative of the FMAS reactions $\text{spinel} + \text{quartz} \rightarrow \text{garnet} + \text{sillimanite}$ during cooling (and related reactions in more chemically complex systems; Figures 2 and 3). The ubiquity of Al-spinel and quartz, inclusions in garnet from sample 22H (Figure 2) are also interpreted to reflect retrograde garnet growth by this reaction. Similar microtextures were identified in granulites from the Musgrave Block of central Australia by White et al. (2002) and interpreted to be the result of the same reaction (alternatively, Boger et al., 2012, interpreted similar garnet [no sillimanite] coronae around magnetite to reflect garnet growth during

prograde biotite breakdown). The moderate Clapeyron slope of the reaction spinel + quartz → garnet + sillimanite (see Figure 2 of White, Powell, & Holland, 2007) prohibits robust interpretation of the nature of the P - T path (clockwise, counterclockwise, or isobaric). However, the presence of retrograde cordierite in sample 22H, but not 18A, requires near-isobaric cooling through the granulite facies at ~0.45–0.6 GPa (Figure 6b). Magnetite inclusions in osumilite from sample 23A are compatible with either a clockwise (Figure 6a) or counterclockwise P - T path, but a clockwise P - T path is more consistent with the observations of Boger et al. (2012) and Jöns and Schenk (2011); uncertainty in the prograde path is discussed in more detail below.

Comparison with other P - T estimates: The stability limits of osumilite must be interpreted with caution due to the absence of minor components in the solution model. Independent estimates for the P - T conditions of metamorphism are provided by the stability limit of spinel–quartz in sample 18A (garnet + sillimanite = spinel + quartz in the system FeO–MgO–Al₂O₃–SiO₂ adjusted for minor Zn after Nichols et al. [1992]), feldspar thermometry (section 3.1), the experimental stability limits of osumilite–garnet in low f O₂ rocks (Carrington & Harley, 1995), and the experimental stability limits of osumilite in high f O₂ (Das et al., 2001). Together, these independent P - T estimates suggest metamorphism at 910–950°C/<0.65 GPa, although the upper temperature limit is poorly constrained by extrapolation of the experiments of Das et al. (2001) to lower pressure (Figure 6b). These P - T estimates are not significantly different than those inferred from pseudosections of osumilite-bearing rocks above. Viewed holistically, the temperature estimates of this study agree with those of Jöns and Schenk (2011: 900–1000°C) and the upper limit of the estimates of Boger et al. (2012: 880–920°C).

The pressures obtained in this study and Boger et al. (0.4–0.6 GPa) are lower than those obtained by Jöns and Schenk (2011; 1.0 GPa). This may be the result of different thermobarometric approaches or differences in the rocks targeted in each study. Jöns and Schenk (2011) determined peak pressures and temperatures from the intersections of experimentally calibrated thermobarometers from different rocks (e.g. intersection of Al in orthopyroxene in one rock with GASP in another rock). When using internally-consistent thermobarometers from single rocks along the western margin of the domain (using the AvPT mode of THERMOCALC), the calculated P - T conditions were $936 \pm 190^\circ\text{C}/0.83 \pm 0.2$ GPa (2σ), which are compatible with the P - T conditions reported by Boger et al. (2012) and this study. An additional limitation in comparing the P - T estimates from Jöns and Schenk (2011) and this study is that many (but not all) of the P - T estimates of Jöns and Schenk came from rocks along the western margin of the Anosyen domain and in the Androyen domain, whereas the thermobarometry in this paper comes from the central and eastern portion of the domain (Figure 1). The higher pressures estimated by Jöns and Schenk could, in part, reflect higher metamorphic pressures to the west.

Prograde metamorphism between 5.5 and 7 kbar was determined by Boger et al. (2012) based on the inferred co-stability of garnet, sillimanite, and cordierite during prograde metamorphism within the “Bakika” and “Amparihy” formations. Alternatively, a higher-pressure prograde path (≥ 1 GPa) was suggested by Jöns and Schenk (2011) based on the intersections of garnet–plagioclase–orthopyroxene–quartz, garnet–sillimanite–quartz–plagioclase, and garnet–orthopyroxene (Al in orthopyroxene) equilibria from different rocks. Both studies inferred a clockwise P - T path based on retrograde growth of cordierite. In sample 23A of this study, fresh osumilite contains inclusions of magnetite (Figure 2a). This

inclusion relationship is consistent with heating at ~0.65 GPa (as proposed by Boger et al., 2012) or during isothermal decompression at ~950°C (as proposed by Jöns & Schenk, 2011). Although the prograde path remains poorly constrained, all interpretations are compatible with a clockwise *P-T* path passing through ~900°C/0.5 GPa. In section 4, I demonstrate that such a *P-T* path is also compatible with observed trends in monazite composition from sample 22H.

Orthopyroxene in the symplectites after osumilite in sample 23A: Orthopyroxene is present in the symplectites after osumilite in sample 23A (Figure 2a), but does not occur as a stable phase in the pseudosection of that sample (Figure 5b). Phase stability within fine-grained symplectites has been demonstrated to reflect local chemical potential gradients that develop as a result of limited and differential elemental mobility at the time of symplectite formation (Schorn & Diener, 2017; Štípská, Powell, White, & Baldwin, 2010; White, Powell, & Baldwin, 2008). This has been shown most starkly by Baldwin, Powell, White, and Štípská (2015) who documented sapphirine, corundum, and spinel as spatially restricted components of symplectites after kyanite in quartz-bearing high-pressure granulites. Pseudosections constructed from whole-rock compositions showed that none of these phases were part of an equilibrium mineral assemblage at the hand-sample or thin-section scale (corundum may never be stable with quartz: see Harlov & Milke, 2002); rather, the limited elemental mobility created chemical potential gradients between the kyanite and surrounding matrix resulting in heterogeneous distribution of minerals within the symplectites.

In sample 23A, orthopyroxene was only found in K-feldspar–cordierite–quartz symplectites immediately adjacent to fresh osumilite; even adjacent to the osumilite, its presence is spatially restricted (Figure 2a). Such restricted and discontinuous occurrence of

orthopyroxene within the symplectites of this sample is similar to the restricted and discontinuous occurrence of spinel/sapphirine/corundum in the examples described above. I interpret orthopyroxene adjacent to osumilite to be the result of local chemical potential gradients during symplectite formation, rather than part of an equilibrium mineral assemblage at the thin-section scale. The absence of orthopyroxene from the pseudosection of this sample (Figure 5b) is consistent with this interpretation. For an additional example of chemical-potential-gradient controlled mineral stability, the reader is referred to Štípská, Powell, and Ráček, (2014) and Štípská, Powell, Ráček, and Lexa (2014). For a more general discussion on the scale of equilibrium during high-grade metamorphism the reader is referred to Guevara and Caddick (2016).

4: U–PB LASER-ABLATION-SPLIT-STREAM ICP-MS (LASS) MONAZITE & ZIRCON GEOCHRONOLOGY

Monazite and zircon were dated by LASS. Details of these analyses are presented in Appendix S3 (see supplementary data Tables S5 and S6 for all LASS analyses). For further explanation of the method, see Kylander-Clark, Hacker, and Cottle (2013) and Kylander-Clark (2017). The reported dates in this paper are weighted means of multiple analyses. The reported uncertainties reflect the standard error of the weighted means and should only be used to compare dates from the same mineral (monazite with monazite or zircon with zircon) within this study. For comparing zircon and monazite dates or dates from either mineral with dates from other studies, a 2% uncertainty should be used, reflecting the long-term reproducibility of homogeneous reference materials in the laser-ablation ICP-MS lab at the University of California, Santa Barbara.

4.1: U/Th–Pb LASS monazite

4.1.1: Monazite U/Th–Pb dates and their relationship to the *P-T* path

Concordia diagrams of all samples are presented in Figure 7. Discordant analyses from samples 21A, 23C, 18B, MD69 define a discordia with an upper intercept near 1900 Ma and are colored red; these dates correspond to the dominant peak in detrital zircon from the Anosyen domain and related metasediments in Madagascar and south India (Boger et al., 2014; Collins et al., 2012). Analyses that are colored red, but appear concordant in U–Pb concordia diagrams (Figures 7a–f), have discordant U–Pb–Th–Pb isotopic ratios. Dates mentioned below are U–Pb dates.

The oldest concordant analyses from all samples that are statistically indistinguishable by the MSWD criterion (Wendt & Carl, 1991) are 579 ± 5 Ma. These analyses correspond to a minor peak in the PDF of all concordant dates (Figure 7i) and are interpreted to reflect monazite neocrystallization during prograde metamorphism (c. 450–600°C; Spear, 2010).

Large monazite grains within symplectite after osumilite in sample 23A are interpreted to have been former inclusions in osumilite (see section 2.1 and Figure 2a). All analyses from these inclusions are 561 ± 6 Ma (Figure 7h). Based on the inferred inclusion relationship, this is a maximum date for osumilite growth and for the peak temperature of metamorphism. This date coincides with emplacement ages of the older generation of plutons in the Anosyen Batholith (Figure 11b).

Monazite with oscillatory zoning (Figure S2) located within a segregation of equant feldspars, quartz, and cordierite in sample 23A is interpreted to have crystallized as the rock cooled through its solidus. Based on the residual solidus calculated for this sample (Figure 5b), the temperature at the time that this monazite grew was 930–940°C. All analyses from

this monazite yield a mean date of 550 ± 6 Ma (Figure 7g). This is the oldest reported date for partial melt crystallization in the Anosyen domain (Figure 11b), and thus a minimum date for the peak temperature of metamorphism.

A majority of the monazite analyses are younger than 550 Ma (Figure 7i) and define two peaks: 535 Ma and 522 Ma. These broad peaks correspond to dates reported for leucosome, pegmatite, small-pluton, and hydrothermal crystallization during cooling of the domain (Figure 11b: Collins et al., 2012; Jöns & Schenk, 2011; Paquette et al., 1994; Tucker et al., 2011). This is consistent with models of monazite solubility in silicate melts: monazite is predicted to dissolve during high-grade metamorphism and precipitate during cooling and melt crystallization (Stepanov, Hermann, Rubatto, & Rapp, 2012).

4.1.2: Monazite composition

Monazite dates from sample 22H span the entirety of the metamorphic event and display trends in composition; the petrological significance of these trends is discussed here. The compositional variables discussed are Gd/Yb and Eu/Eu* ($\text{Eu}^* = [\text{Sm} \times \text{Gd}]^{0.5}$); values used in the ratios are normalized to concentrations of the elements in C.I. chondrite (McDonough & Sun, 1995). Monazite dates from each of the other samples only span a portion of the metamorphic event and many of the analyses in each of these samples are the same age within uncertainty, meaning that trends in monazite composition cannot be reliably identified; compositions of monazite in these samples are not discussed.

Gd/Yb in sample 22H decreases between 580 and 550 Ma, after which it increases (Figure 8A). This pattern can be seen in individual monazite grains (Figure 8C): low-Y (high

Gd/Yb) cores were mantled/replaced by high-Y (low Gd/Yb) mantles, and then followed by low-Y rims (high Gd/Yb). Eu/Eu* exhibits the same trend (Figure 8D).

4.1.2.1: Monazite Gd/Yb and garnet growth/resorption

I interpret decreases in monazite Gd/Yb to reflect garnet breakdown, whereas increases are interpreted to reflect garnet growth (e.g. Mottram et al., 2014; Rubatto, Hermann, & Buick, 2006; Stearns et al., 2013). For sample 22H, this implies that the mode of garnet decreased at the time ~550 Ma and subsequently increased (Figures 8a, 8b). This is consistent with the petrographic interpretation of retrograde garnet growth by the reaction $\text{spinel} + \text{quartz} \rightarrow \text{garnet} + \text{sillimanite}$ (Figure 2; section 3.2.1) and with 6 of 7 analyses from monazite inclusions in garnet having dates younger than 550 Ma (Figure 8a). These trends are compatible with metamorphism along a clockwise P - T path, in which the mode of garnet decreases toward high temperature and low pressure and subsequently increases during cooling (Figure 8b).

4.1.2.2: Monazite Eu/Eu* as a record of changes in oxidation state

Changes in Eu/Eu* in monazite have been interpreted to reflect changes in the mode of feldspar (e.g. Holder, Hacker, Kylander-Clark, & Cottle, 2015; Mottram et al., 2014; Rubatto et al., 2006): increases reflect feldspar breakdown and decreases reflect feldspar growth. According to this hypothesis, Eu/Eu* in monazite should increase during partial melting within the granulite facies as feldspar breaks down and decrease during melt crystallization as feldspar grows. This trend is opposite to that observed in sample 22H: Eu/Eu* decreases

during partial melting (feldspar breakdown) and increases during melt crystallization (feldspar growth) (Figures 8d, 8f).

Implicit, but never discussed in the model described above, is that bulk-rock $\text{Eu}^{3+}/\text{Eu}^{\text{total}}$ is less than unity, $\text{Eu}^{3+}/\text{Eu}^{\text{total}}$ is constant, and $K_d^{\text{Eu}^{2+}}_{\text{feldspar/monazite}}$ is $\gg 1$. I propose that changes in $\text{Eu}/\text{Eu}^*_{\text{monazite}}$ could also be the result of changes in $\text{Eu}^{2+}/\text{Eu}^{3+}$, because of the difference in size and charge between Eu^{2+} and Eu^{3+} (Shannon, 1976). The experiments of Burnham et al. (2015) demonstrated that constant $\text{Eu}^{3+}/\text{Eu}^{\text{total}}$ in silicate melts has a temperature dependence parallel to the quartz–fayalite–magnetite (FMQ) buffer. Although the exact value of $\text{Eu}^{3+}/\text{Eu}^{\text{total}}$ depended on melt composition in their experiments, the results suggest that relative changes in $\text{Eu}^{3+}/\text{Eu}^{\text{total}}$ can be inferred from changes in $f\text{O}_2$ relative to FMQ (for convenience, all mentions of $f\text{O}_2$ in the following paragraphs are relative to FMQ).

Whether changes in bulk-rock $f\text{O}_2$ are recorded by monazite Eu/Eu^* can be tested by comparing monazite Eu/Eu^* with Sr or Sr/Ca (normalizing to Ca removes the effect of the brabantite substitution— $[\text{Ca},\text{Sr}]\text{Th} \leftrightarrow 2\text{REE}$ —on monazite Sr concentration). If $\text{Eu}^{3+}/\text{Eu}^{\text{total}}$ remained constant during metamorphism ($f\text{O}_2$ remained constant), changes in $\text{Eu}/\text{Eu}^*_{\text{monazite}}$ should be positively correlated with changes in $\text{Sr}/\text{Ca}_{\text{monazite}}$ because Sr^{2+} and Eu^{2+} have nearly identical ionic radii (Shannon, 1976) and will therefore be equally compatible in each phase. If $\text{Eu}/\text{Eu}^*_{\text{monazite}}$ and $\text{Sr}/\text{Ca}_{\text{monazite}}$ are not correlated, the data may indicate changes in $f\text{O}_2$ and $\text{Eu}^{3+}/\text{Eu}^{\text{total}}$ during metamorphism.

In sample 22H, $\text{Sr}/\text{Ca}_{\text{monazite}}$ is positively correlated with $\text{Eu}/\text{Eu}^*_{\text{monazite}}$ at $\text{Eu}/\text{Eu}^*_{\text{monazite}} > 0.1$, but shows no correlation at $\text{Eu}/\text{Eu}^*_{\text{monazite}} < 0.1$. The positive correlation at $\text{Eu}/\text{Eu}^*_{\text{monazite}} > 0.1$ is not robust, being strongly influenced by a single outlier datum (Figure 8d). Based on the above criterion, the lack of a correlation between $\text{Sr}/\text{Ca}_{\text{monazite}}$ and

$\text{Eu}/\text{Eu}^*_{\text{monazite}}$ is compatible with $\text{Eu}/\text{Eu}^*_{\text{monazite}}$ have been influenced, in part, by changes in $f\text{O}_2$.

Changes in $f\text{O}_2$ can result from fluid-rock interaction (open system) or from changes in mineral assemblage in unbuffered rocks (closed system). The magnitude of open-system modification of $f\text{O}_2$ in the osumilite gneisses cannot be constrained. To test how much bulk-rock $f\text{O}_2$ and monazite Eu/Eu^* might have changed from closed-system metamorphism (from changes in pressure and temperature only) the pseudosection of sample 22H was contoured for μO_2 , an intensive variable defined by the compositions and proportions of the Fe^{2+} – Fe^{3+} -bearing solid solutions (garnet, biotite, ilmenite, and spinel in our pseudosection). $f\text{O}_2$ was calculated from μO_2 along the proposed P - T path using the relationship $f\text{O}_{2(T,P)} = \exp([\mu\text{O}_{2(T,P)} - \mu\text{O}_{2(T,1\text{bar,pure O}_2)}]/RT)$ (Figure 8e). Along this path, $f\text{O}_2$ decreased during heating and decompression and increased during cooling; the total magnitude of the change is $\sim 1 \log_{10}$ unit. The largest decrease in $f\text{O}_2$ is correlated with the growth and breakdown of spinel (Figure 8e). The exact relationship between $f\text{O}_2$, T , and $\text{Eu}^{3+}/\text{Eu}^{\text{total}}$ is not known for this type of rock; however, the experiments of Burnham et al. (2015) on silicate melts suggest that 1 \log_{10} unit change in $f\text{O}_2$ is sufficient to change $\text{Eu}^{3+}/\text{Eu}^{\text{total}}$ by 0.05–0.15 (higher $f\text{O}_2 =$ higher $\text{Eu}^{3+}/\text{Eu}^{\text{total}}$); this is similar to the total variation in monazite Eu/Eu^* observed in sample 22H (0.12).

In summary, $\text{Eu}/\text{Eu}^*_{\text{monazite}}$ has been interpreted as a record of feldspar growth and breakdown, but $f\text{O}_2$ likely plays a role too in some systems. $\text{Eu}/\text{Eu}^*_{\text{monazite}}$ from sample 22H does not correlate with $\text{Sr}_{\text{monazite}}$ (or Sr/Ca) as expected for partitioning in a system with constant $\text{Eu}^{3+}/\text{Eu}^{\text{total}}$. Modeled changes in $f\text{O}_2$ along the proposed P - T path may correspond to sufficient changes in $\text{Eu}^{3+}/\text{Eu}^{\text{total}}_{\text{rock}}$ to explain the observed variation in $\text{Eu}/\text{Eu}^*_{\text{monazite}}$. The

modeled changes in fO_2 were a function of pressure, temperature, and mineral assemblage only; the largest changes in fO_2 corresponded to the growth and breakdown of spinel. Open-system fluid-rock interaction might also influence bulk-rock fO_2 and therefore Eu/Eu*, but changes in fO_2 as a result of fluid-rock interaction are likely to be small in most metamorphic environments due to the large buffering capacity of rocks (Dyar, Lowe, Guidotti, & Delaney, 2002; Rumble, 1978).

4.2: U–Pb LASS zircon

Zircon grains in the majority of samples are less than 30 μm across and only a few grains were found in most samples. One exception to this is osumilite gneiss 23A, in which several 100 μm zircon grains occur in association with a retrograde biotite corona around magnetite and ilmenite (Figure 9). The grains contain oscillatory zoned cores, CL-dark mantles, and CL-bright rims. U–Pb analyses from grain cores define a discordia between 1900–1800 and 600–500 Ma. Concordant mantle and rim analyses are 580–520 Ma, similar to monazite dates (above), but the ubiquity of an inherited component, and the lack of any trends in zircon composition make the pressure-temperature significance of the dates unclear. Ti-in-zircon temperatures (Ferry & Watson, 2007) have a weighted average of $790 \pm 8^\circ\text{C}$ and there is no correlation between Ti concentrations and U–Pb dates. Either the zircon grains were not in equilibrium with the other phases in the rock (possibly due to their position in the now-former osumilite) or they did not grow/recrystallize at UHT. A similar lack of compositional equilibrium during resetting of zircon U–Pb dates has been documented in the granulites of Blanský Les in the Bohemian Massif (Štípská, Powell, Hacker, Holder, & Kylander-Clark, 2016). All monazite from this sample is isotopically homogeneous: 561 ± 6 Ma (Figure 7h).

5: DISCUSSION

5.1: Duration of heating and cooling

I infer prograde metamorphism in the Anosyen Domain of southern Madagascar to have lasted $<29 \pm 8$ Myr based on the differences between the oldest monazite dates from all samples (579 ± 5 Ma) and the oldest monazite interpreted to have formed from melt crystallization (550 ± 6 Ma; Figure 11b; see section 4.1.1 for discussion and evaluation of the data). The difference in melt crystallization age and the age of monazite inclusions in osumilite at the same outcrop (sample 23A) constrains the residence time of the rocks near the peak metamorphic temperature ($\sim 930^\circ\text{C}$) to have been $<11 \pm 8$ Ma.

U/Th–He monazite dates (530–510 Ma) from the gigantic monazite at Manangotry Pass indicate that the rocks took ~ 30 Myr to cool to 400°C (Montel et al., 2018): an average cooling rate of 17 ± 7 K/Myr. The Sm–Nd garnet–zircon–monazite–whole-rock isochron date of 588 ± 13 Ma, reported by Paquette et al. (1994) from an Al-spinel–quartz gneiss, corresponds with the time of prograde metamorphism inferred in this study and the emplacement of the early plutons of the Anosyen Batholith (Figure 11), which also preserve Sm–Nd consistent with prograde to peak metamorphism (~ 570 – 560 Ma). Smit, Scherer, and Mezger (2013) have suggested that preservation of Sm–Nd dates through a UHT event requires short residence time at UHT and cooling rates of 20 to >100 K/Myr through the granulite facies: an interpretation that is consistent with the short duration of peak metamorphism estimated in this study and the cooling rates constrained by the monazite U/Th–He dates described above.

The short duration of prograde metamorphism, short residence time at peak temperature, and potentially rapid cooling rates all suggest that advection of heat may have been important

for the formation of the osumilite gneisses. However, the interpretation that metamorphism was the result of continental collision and the overall long duration of the metamorphic event—recorded by monazite and zircon within the gneisses—are compatible with radiogenic heating within a long-lived thick crust. Below, I discuss the relative importance of advected and radiogenic heat.

5.2: Can metamorphism be explained by high radiogenic-heat production within thickened crust and no advection?

Horton et al. (2016) and Clark et al. (2015) proposed that UHTM in southern Madagascar and southern India might have been caused by the accumulation of radiogenic heat in the middle to lower crust if a 60–70 km thick crust was maintained for c. 60 Myr and if the crust contained an anomalously high concentration of the heat-producing elements U, Th, and K. Measured high heat production rates from gneisses in these terranes and long durations of metamorphism were cited as support for this hypothesis. The models of Horton et al. (2016) were particularly thorough, demonstrating the sensitivity of crustal temperatures to the distribution of heat-producing elements, thermal conductivity, mantle heat flow, and erosion rates.

The mean and standard error heat production rates from regional whole-rock data (taken from GAF-BGR [2008] and U, Th, and K concentrations corrected to 600 Ma) for all the tectonometamorphic domains of southern Madagascar are plotted against the ratio of peak metamorphic temperature at peak metamorphic pressure (Figure 10). For terranes in which isothermal decompression has been inferred, the P - T conditions prior to decompression were used. Uncertainties in temperature and pressure were taken to be 50°C and 0.1 GPa. The

highest average heat production rate, $\sim 3.5 \mu\text{W}/\text{m}^3$, is associated with the highest T/P metamorphic rocks (Anosyen and Antananarivo domains). T/P of metamorphism is correlated with heat-production rates at the terrane scale. To test the magnitude of heating that might have resulted from radioactive decay within a thickened crust, I constructed one-dimensional lithospheric heat flow models, which are described briefly below and more thoroughly in Appendix S1.

I calculated relaxation of the thermal gradient of the crust following thickening from 30 to 60 km using one-dimensional finite-difference heat flow models for three high-heat-production profiles: a homogeneous crust with a heat-production rate of $2 \mu\text{W}/\text{m}^3$, a homogeneous crust with a heat-production rate of $3 \mu\text{W}/\text{m}^3$, and the heat-production profile used by Horton et al. (2016) for the southern Anosyen domain. General details of the modeling approach were described by Peacock (1989). Specific model parameters are outlined in Appendix S1; heat-production profiles for each model are shown in the supplementary data Table S7.

Figure 12a shows the crustal thermal gradient 40 Myr after thickening (the approximate maximum duration of prograde metamorphism from this study: $<29 \pm 8$ Myr) for each model—using a “typical” mantle lithosphere thickness of 140 km—compared to the peak P - T estimates and P - T paths from this study, Jöns and Schenk (2011), & Boger et al. (2012). Only the models with average crustal heat-production $\geq 3 \mu\text{W}/\text{m}^3$ reached the peak P - T conditions proposed by these studies.

Figure 12b shows the time required to heat the crust to 930°C at a depth of 25km (c. 0.65 GPa; corresponding to the P estimates of this study and Boger et al.) as a function of mantle lithosphere thickness (proximity of the lower crust to the convecting mantle) for each of the

models. Temperatures of 930°C at 25 km depth are only reached in the models if heat-production rates are $>3 \mu\text{W}/\text{m}^3$ or the mantle lithosphere is <80 km. Such a thin mantle lithosphere may not be unreasonable for a collisional orogen. UHT lower-crustal xenoliths have been documented in Qiangtang, Tibet (Hacker et al., 2000), directly overlying mantle with anomalously slow seismic wave speeds (e.g. Liang et al., 2012; McNamara, Walter, Owens, & Ammon, 1997). The low wave speeds have been interpreted to reflect a thin lithospheric mantle (40–80 km thick; e.g. Jiménez-Munt, Fernández, Vergés, & Platt, 2008; Tunini et al., 2016) and possibly asthenospheric upwelling following lithospheric foundering (e.g. Jiménez-Munt & Platt, 2006; Liang et al., 2012; Molnar, England, & Martinod, 1993).

5.3: How important were advective heat sources?

The short timescales of heating ($<29 \pm 8$ Ma), preservation of Sm–Nd dates from prograde to peak metamorphism, the location of osumilite gneisses around the Anosyen Batholith (Figure 1), emplacement dates for many of the high-temperature plutons within the Anosyen Batholith during prograde to peak metamorphism (Figure 10; see section 1.2), the low pressure of regional metamorphism (c. 0.6 GPa: Boger et al., 2012; this study), and the extreme heat-production rates required to reproduce metamorphic P - T estimates in models (Figure 12a–12b and section 5.2) all suggest that advective heat sources might have been important in the thermal evolution of the southeastern Anosyen domain.

5.3.1: High-temperature melt transfer within the crust

The Anosyen Batholith consists of $>80\%$ anhydrous granitoids and is the largest pre- to syn-tectonic body of the Ambalavao suite (GAF-BGR, 2008). In this section, I more generally

refer to all of the plutons in southeast Madagascar as the Anosyen Batholith. The majority of dates from the Batholith are 570–560 Ma with a lesser number c. 530 Ma (see section 1.2 and Figure 10); the mode of dates from the Batholith correlates with the timing of prograde to peak metamorphism. Isotopic data on the Batholith are limited to three whole-rock Nd isotope measurements of granites compatible with formation from crustal melting (Paquette et al., 1994); however gabbro and quartz monzonite with trace-element composition distinct from the granites (no isotopic data is available) suggest some of the magmas had a different source (GAF-BGR, 2008), possibly the mantle. Hercynitic spinel in some of the granitoids indicates emplacement temperatures in the granulite facies. Orthopyroxene granitoids (“charnockites”) were likely emplaced at temperatures of 950–1050°C (Frost & Frost, 2008; Kilpatrick & Ellis, 2011); this generalization is corroborated by modeling the crystallization of these orthopyroxene granitoids in rhyoliteMELTS (Appendix S2), which suggests magmatic temperatures of 1000–1100°C. The high magmatic temperatures estimated for the plutons, and large extent of the Batholith (Figure 2), suggest that magmatic advection may have been an important heat source for metamorphism in the surrounding gneisses.

To investigate the potential magnitude of heating caused by the Anosyen Batholith, I calculated the minimum volume of magma required to heat a metamorphic terrane to 930°C using the following energy balance:

$$(930-T_c) C_{pc} V_c \rho_c = V_m \rho_m ((T_m-930) C_{pm} + L)$$

T_c is the temperature of the crust into which the magma is emplaced, C_{pc} the heat capacity of the crust, ρ_c the density of the crust, V_c the volume of crust into which the magma is emplaced, V_m the volume of the magma, ρ_m the magma density, T_m is the emplacement temperature of the magma, C_{pm} the heat capacity of the magma, and L the latent heat of

crystallization of the magma. For simplicity, the density of the magma and the crust were assumed to be the same; $C_{p_c} = 1.25 \text{ J/gK}$; $C_{p_m} = 1.5 \text{ J/gK}$; and $L = 300 \text{ J/g}$.

The volume of magma calculated this way is a minimum, because 1) if the magma is emplaced over a period of time rather than instantaneously, conduction causes cooling; 2) the latent heat of crystallization for the crustal rocks is neglected, because the fertility of the rocks at the time of magma emplacement is unknown; and 3) not all of the batholith was emplaced during prograde metamorphism (Figure 10; see section 1.2 for summary of geochronology of the batholith). Emplacement of magma over a millions of years, rather than instantaneously, results in smaller-magnitude, but longer-lived heating (Chapman and Furlong, 1992).

The results of these calculations are shown in Figure 12c. I used the peak temperatures for the Anosyen domain >100 km away from the Batholith (800–850°C: Boger et al., 2012; Raith et al., 2008) as the possible temperature of the crust into which the magmas were intruded. I used half the area proportion of the Batholith currently exposed as the volume proportion of intruded magma; only half the aerial extent of the Batholith was used in the calculations to provide a conservative estimate for the magnitude of heating, in recognition of younger dates reported for some of the plutons (see section 1.2).

If the calculated emplacement temperatures of the orthopyroxene granites are representative of the batholith, the Anosyen Batholith is large enough to explain the differences in peak metamorphic temperature across the domain—930°C near the batholith (this study) and 800–850°C near Ihosy (Raith et al., 2008; Boger et al., 2012)—*but the Batholith is not large or extensive enough to have been the only heat source for metamorphism*. This is supported by recognition of very high temperatures (~900°C)

recorded by Zr in rutile (Horton et al., 2016) and Fe³⁺-rich sapphirine-bearing rocks (Jöns and Schenk, 2011; Wheller et al., 2015) near the western margin of the domain, approximately 60 km from the batholith. Additionally, mantle-derived heat sources that may have contributed to crustal melting and metamorphism are discussed below.

5.3.2: Mantle-derived heat sources: mafic magmatism and asthenospheric upwelling

Although minor, gabbro within the Anosyen Batholith suggests that mafic magmatism (and associated asthenospheric upwelling) may have contributed to heating the Anosyen domain. The similarities in major- and trace-element ratios in the gabbro and the much more abundant quartz monzonites of the Batholith (GAF-BGR, 2008) and the low densities of the exposed gneisses (2.7–2.8 g/cm³ calculated from the pseudosections of this study) suggest that mafic plutons may be more abundant at depth (see Glazner, 1994, for discussion of density stratification of the crust). The thermal significance of mafic magmatism may be underestimated by the current exposure. Mantle-sourced heating is also suggested by oxygen and carbon isotopes of marbles, calc-silicates, and metamafic rocks from the largest regional shear zones (such as the Beraketa shear zone, Figure 1; Pili, Sheppard, Lardeaux, Martelat, & Nicollet, 1997) which suggest mantle-derived fluids entered the crust during orogenesis, possibly associated with mafic magmatism or lithospheric thinning (Pili, Ricard, Lardeaux, & Sheppard, 1997). Despite the scarcity of exposed mafic plutons, it cannot be ruled out that mafic magmatism and/or asthenospheric upwelling contributed significant heat to the terrane.

6: CONCLUSIONS

The Anosyen domain of southeast Madagascar was metamorphosed at $\sim 930^{\circ}\text{C}/0.6\text{ GPa}$ along a clockwise P - T path. At the 100's-of-km scale, metamorphic grade correlates with average heat-production rate, indicating that radioactive decay of U, Th, and K was one of the main heat sources for high-grade metamorphism. Models of heat flow and radiogenic heat production within thickened crust (without advection) require an average crustal heat-production rate of $>3\ \mu\text{W}/\text{m}^3$ and a mantle lithosphere thickness of $<80\text{ km}$ to reproduce the P - T conditions experienced by the gneisses within the time permitted by monazite petrochronology ($<29 \pm 8\text{ Ma}$).

Advective heating may also have been important. The volume and distribution of high-temperature plutons of the Anosyen Batholith are sufficient to explain differences in peak temperature across the domain ($\sim 930^{\circ}\text{C}$ near the Anosyen Batholith and $800\text{--}850^{\circ}\text{C}$ near Ihosy), but the processes that led to the generation of the plutons in the Batholith remain unclear. Isotopic data on the Batholith are limited to three whole-rock Nd isotope measurements compatible with formation from crustal melting (Paquette et al., 1994), highlighting the potential importance of intracrustal mass and heat transfer in the formation of low-pressure granulite-UHT terranes. Minor mafic plutons and geochemically associated quartz monzonite (GAF-BGR, 2008) along with mantle-sourced carbon and oxygen isotopes from rocks within major shear zones (Pili, Ricard, et al., 1997; Pili, Sheppard, et al., 1997), suggests that mantle-sourced heat (mafic magmatism or asthenospheric upwelling) may have also been important despite the scarcity of mafic plutons exposed.

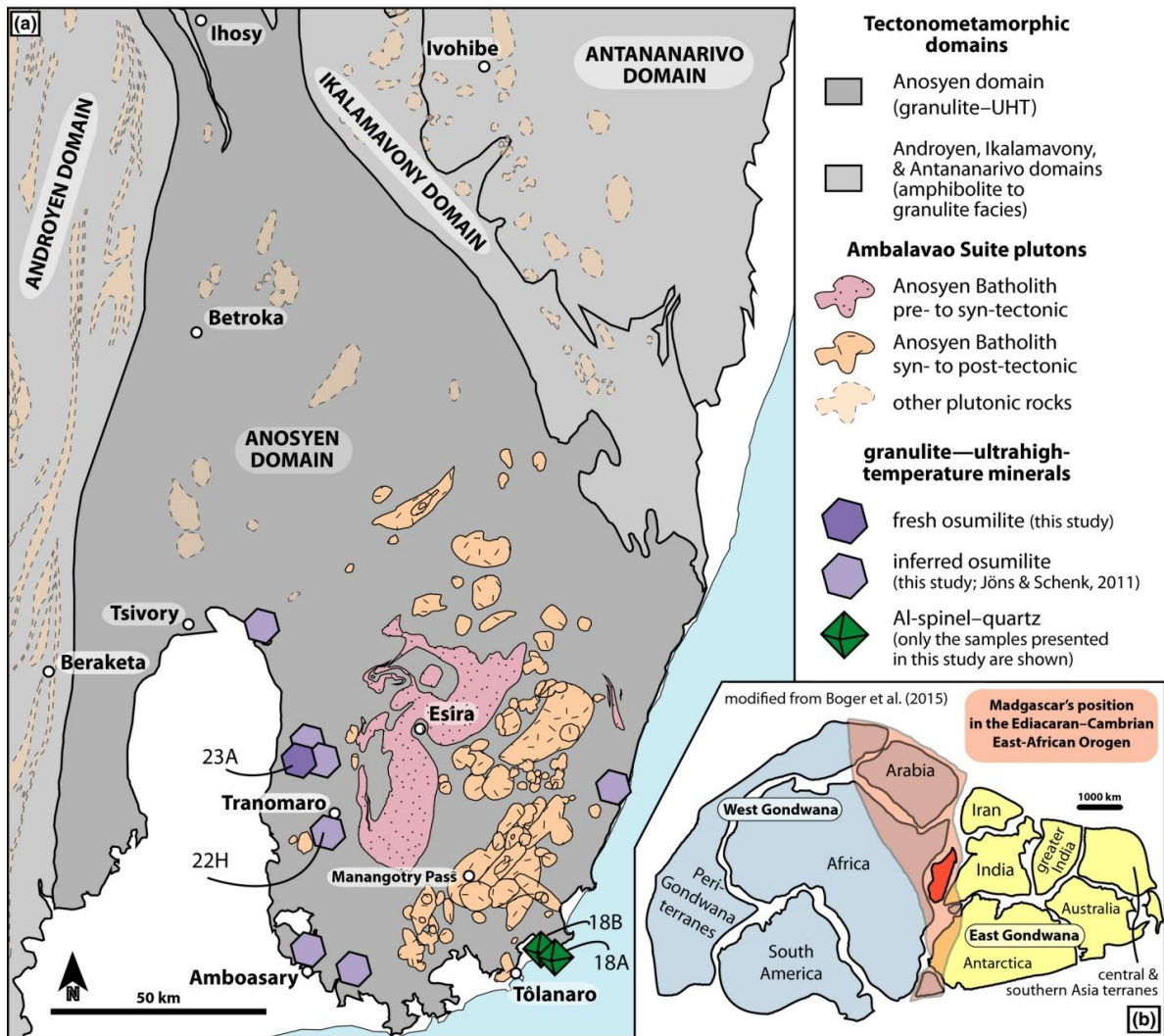


Figure 1. (a) Simplified geological map of the Anosyen domain in southeast Madagascar (modified from GAF - BGR, 2008). (b) The position of Madagascar during Gondwana assembly (modified from Boger et al., 2015).

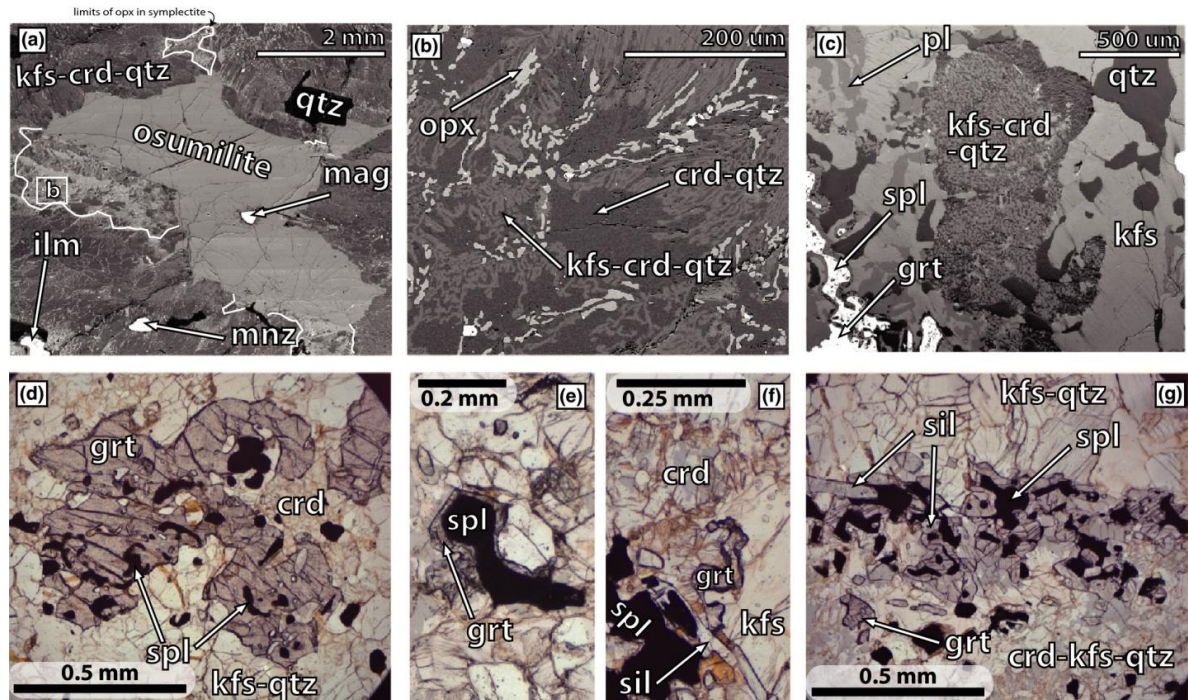


Figure 2. Microtextures of osumilite gneisses 23A and 22H. Mineral abbreviations after Kretz (1983). (a) Back - scattered electron (BSE) image of fresh osumilite with a magnetite inclusion, surrounded by a symplectite of K - feldspar-cordierite-quartz-orthopyroxene from sample 23A. Orthopyroxene only occurs in four restricted areas immediately adjacent to the osumilite grain. (b) Higher magnification BSE image of the symplectite in (a). (c) BSE image of K - feldspar-cordierite-quartz symplectite interpreted to be a pseudomorph after osumilite in sample 22H. (d) Optical photomicrograph of xenoblastic garnet interpreted to have grown at the expense of spinel in sample 22H. (e) Corona of garnet around spinel in sample 22H. (f) Partial corona of garnet around cordierite in sample 22H. (g) Coronae of sillimanite around spinel in sample 22H, interpreted to reflect sillimanite growth at the expense of spinel during cooling.

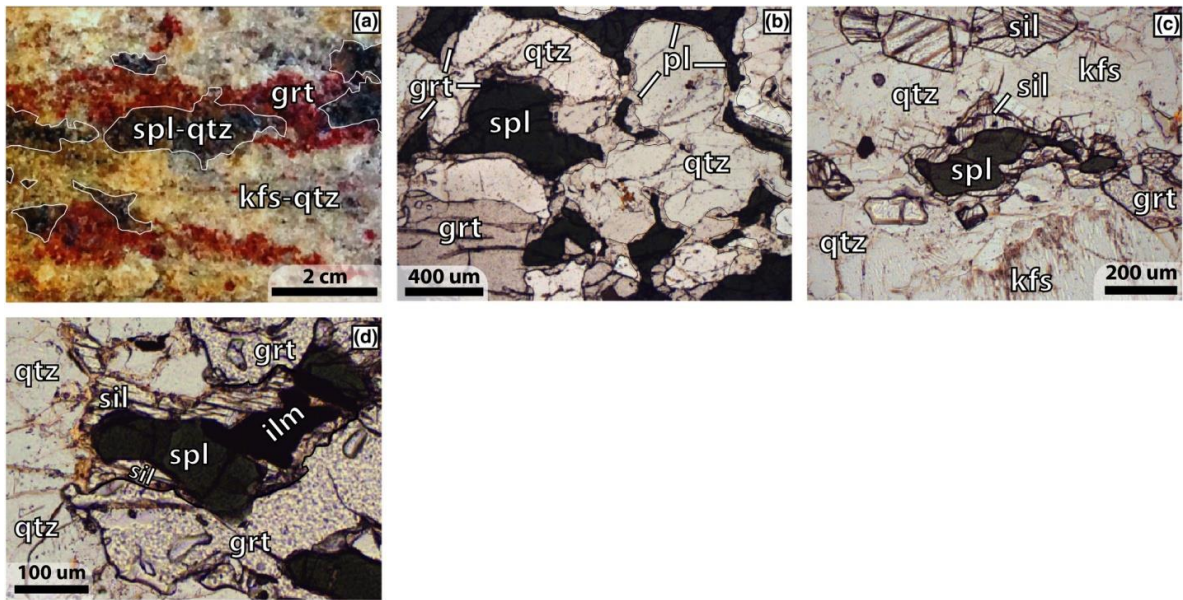


Figure 3. Microtextures of Al - spinel–quartz gneiss 18A. (a) Hand - sample photograph showing the common association of spinel with quartz. (b) Garnet and plagioclase coronae separate spinel and quartz that are interpreted to have once been stable together. (c) Corona of sillimanite separating spinel and quartz. (d) Corona of sillimanite and garnet separating spinel and quartz.

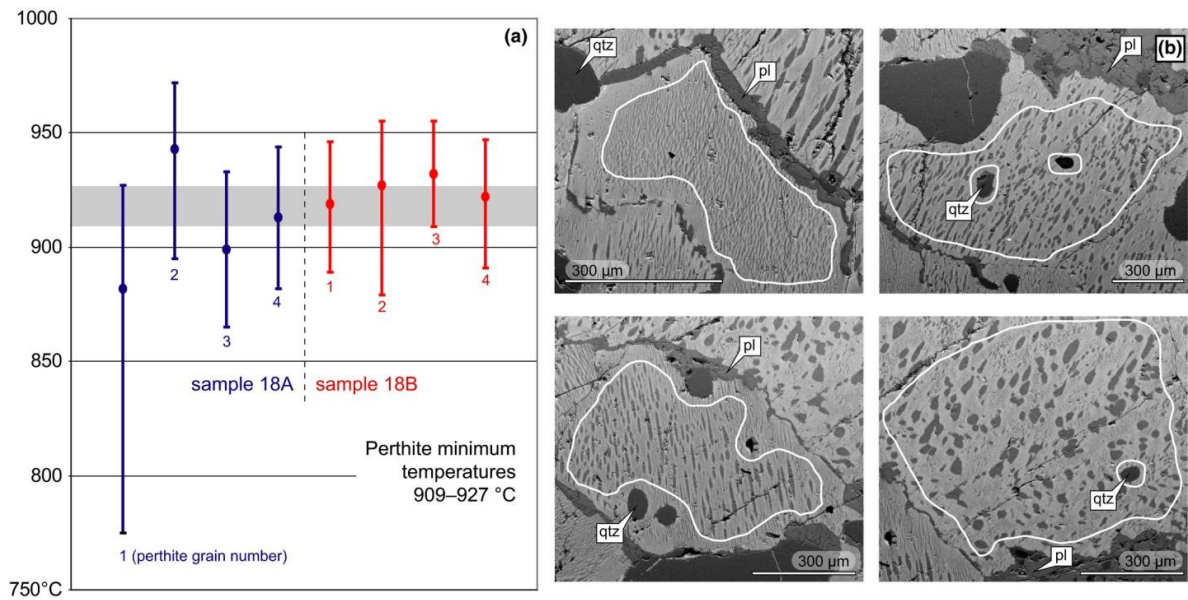


Figure 4. (a) Mesoperthite and adjacent, grain - boundary plagioclase—interpreted to have formed during exsolution—record a minimum metamorphic temperature of 910–930°C. (b) Mesoperthite grains used for thermometry in sample 18A. Shapes show the areas of perthite reintegrated for thermometry. Mineral abbreviations after Kretz (1983).

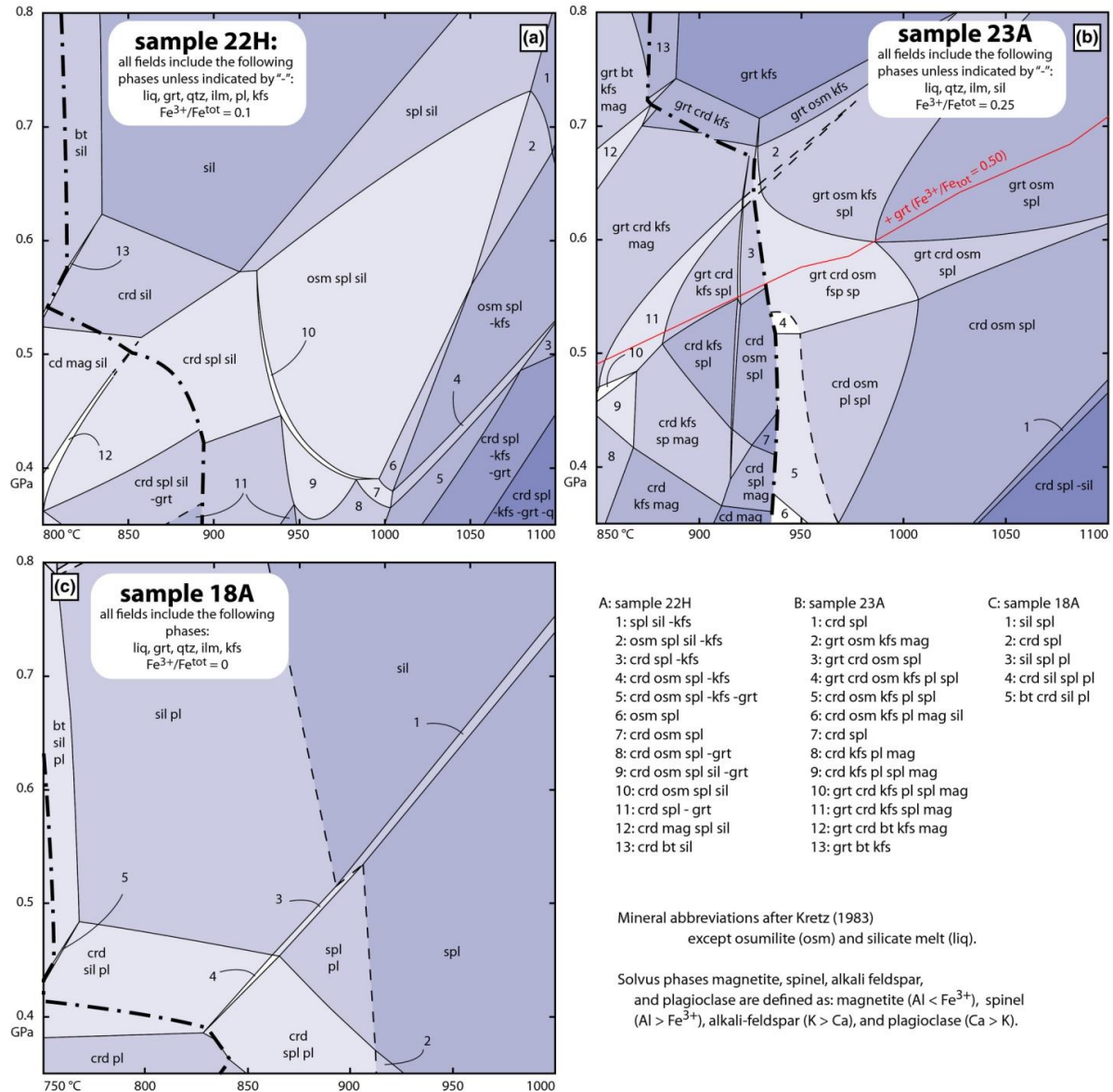


Figure 5. Pseudosections of (a) osumilite - garnet gneiss 22H, (b) osumilite gneiss 23A, and (c) Al - spinel-quartz gneiss 18A. Bold, dash - dot lines are the residual solidi: the water content at temperatures higher than these lines was set such that the interpreted peak assemblages did not contain more than 10 vol.% melt. At temperatures below this line, additional H₂O was added to the calculations to stabilize melt, thereby providing a better model of melt - saturated phase relationships during prograde metamorphism (see text for more details and discussion of melt - reintegration methods). The positions of dashed phase boundaries were poorly constrained by the calculation (typically the spinel and feldspar solvi). Darker shading indicates higher variance mineral assemblages.

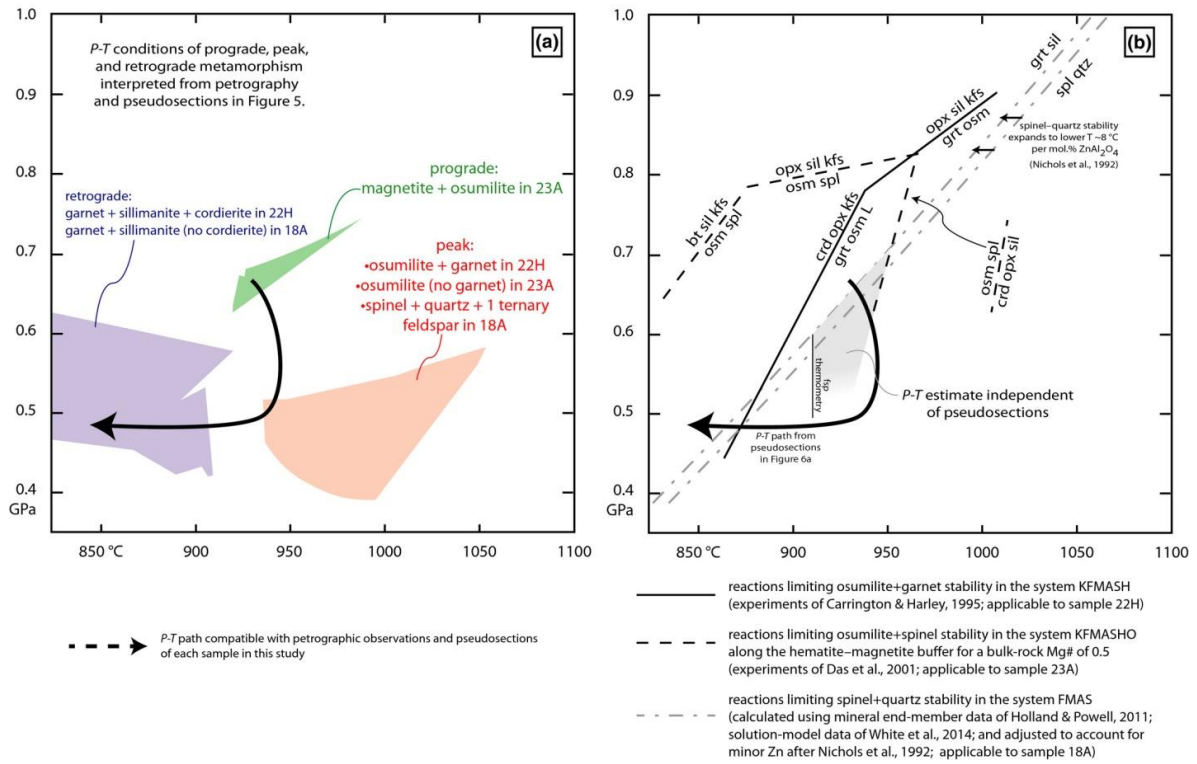


Figure 6. Interpreted pressures and temperatures of metamorphism for the samples in this study. (a) The stability fields of prograde, peak and retrograde mineral assemblages from pseudosections in Figure 5. (b) Independent estimates for the $P-T$ conditions of the samples in this study. Osumilite in sample 23A contains Na, Ca, Ti, Mn and possibly Fe^{3+} , none of which are accounted for in the osumilite solution model used in Figures 5 and 6a. Independent estimates for osumilite stability are provided by the experiments of Das et al. (2001; high $f\text{O}_2$) and Carrington and Harley (1995; low $f\text{O}_2$). Spinel in sample 18A contains ≤ 1 mol.% ZnAl_2O_4 , which is not accounted for in the spinel solution model used in Figures 5 and 6a. The effect of Zn on spinel stability was evaluated by Nichols et al. (1992); for 1 mol.% ZnAl_2O_4 , the stability of spinel with quartz expands $\sim 8^\circ\text{C}$ down temperature. Feldspar thermometry provides an additional, independent $P-T$ constraint. Estimates of peak temperature from these methods are only slightly lower than estimates from pseudosections.

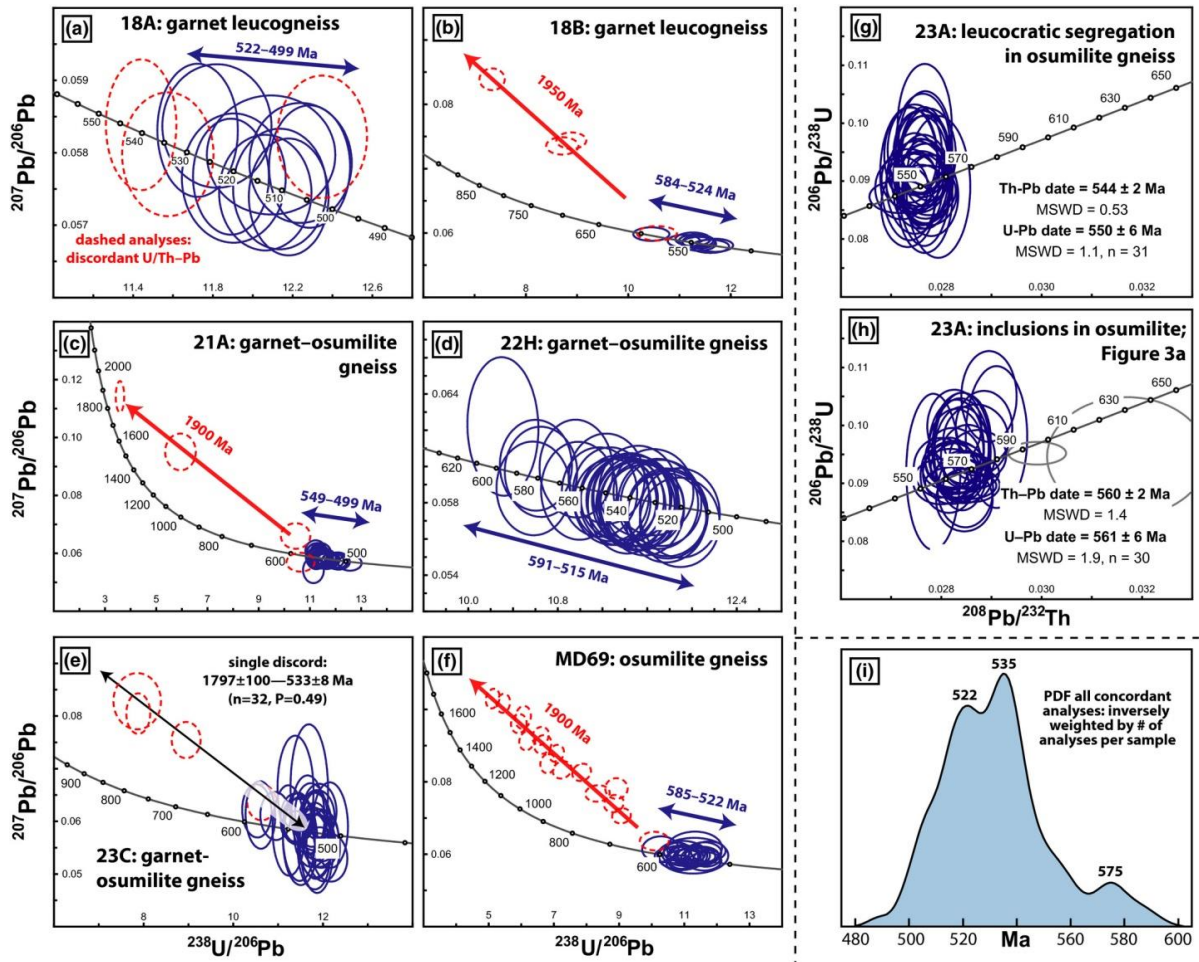


Figure 7. (a–f) Concordant monazite dates record 80 Myr of tectonic and thermal activity in the Anosyen domain from 580 to 500 Ma. (g–h) Monazite inclusions in osumilite and from a leucocratic segregation—interpreted to have formed during melt crystallization—at the same outcrop constrain the timing of peak metamorphism between 561 ± 6 and 550 ± 6 Ma. (i) PDF of all concordant monazite dates inversely weighted by number of analyses per sample. The oldest dates define a peak at 575 Ma—interpreted as prograde monazite neocrystallization—whereas the majority of analyses are <500 Ma and interpreted to reflect growth or recrystallization during cooling.

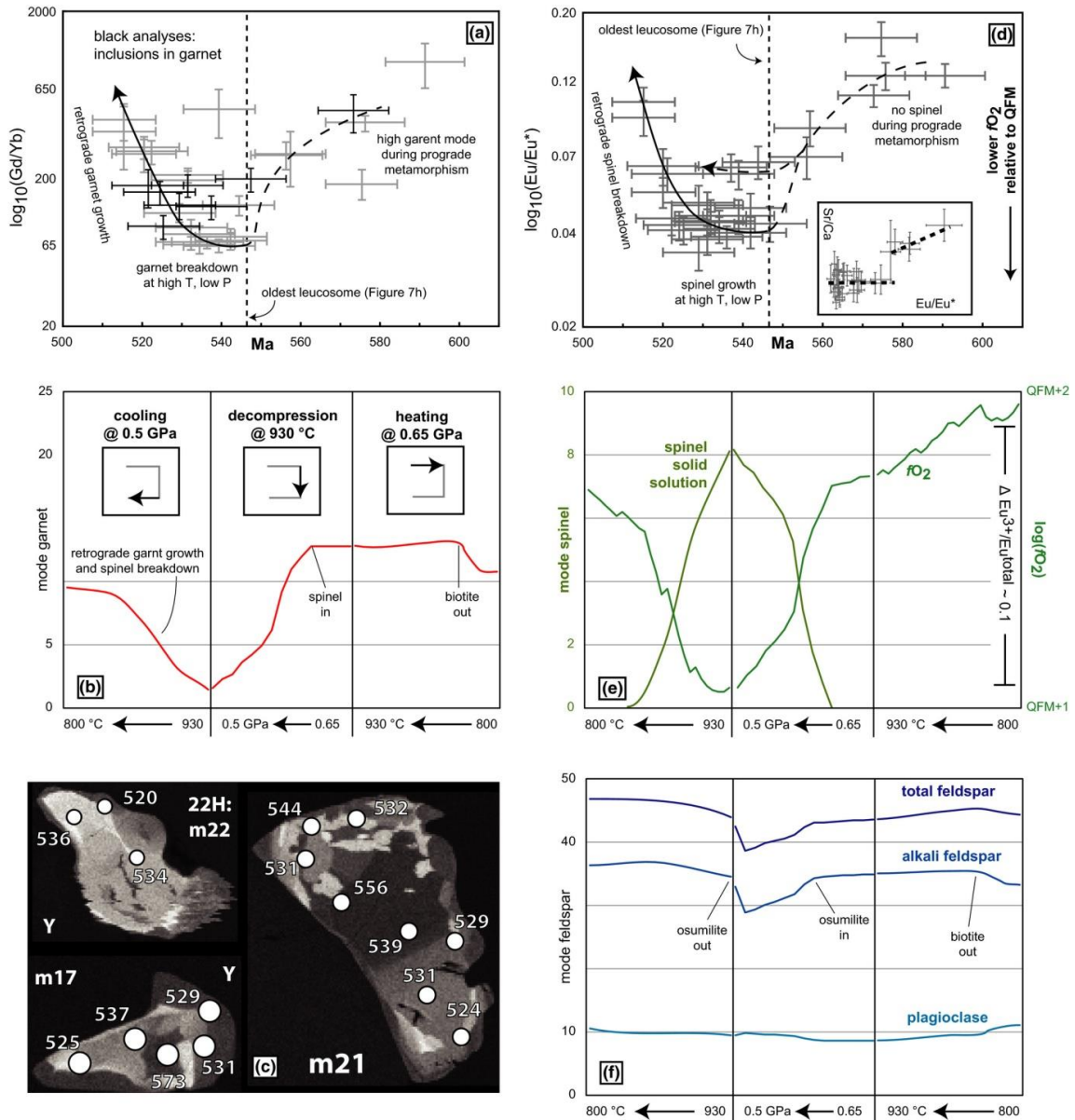


Figure 8. Monazite compositions reflect changes in the mode of garnet and bulk - rock $f\text{O}_2$ during metamorphism. Data are from sample 22H. (a) Gd/Yb in monazite record garnet breakdown during heating and garnet growth during cooling, consistent with petrographic observation in Figure 3 and garnet modes (b) calculated from a plausible clockwise P - T path extracted from pseudosections in Figure 5. (c) Y zoning in individual monazite grains shows low - Y cores, high - Y mantles and low - Y rims, consistent with Gd/Yb trends in a: high Gd/Yb corresponds to low Y. (d) Eu/Eu^* decreases prior to 550 Ma, then increases, but is not correlated with Sr/Ca as expected for partitioning if bulk - rock $\text{Eu}^{2+}/\text{Eu}^{3+}$ was constant. (e) $f\text{O}_2$ decreases, then increases along the P - T path proposed in Figure 7a due to changes in mode and composition of spinel. Changes in $f\text{O}_2$ relative to FMQ result in corresponding changes in $\text{Eu}^{3+}/\text{Eu}^{\text{total}}_{\text{rock}}$ (Burnham et al., 2015) and might explain the observed trends in $\text{Eu}/\text{Eu}^*_{\text{monazite}}$, but lack of a correlation between Eu/Eu^* and Sr/Ca. See text for more details. (f) Total feldspar decreases towards higher temperatures and lower pressures as a result of partial melting. It has been hypothesized that feldspar breakdown during partial melting should be recorded as an increase in monazite Eu/Eu^* (e.g. Rubatto et al., 2006); the opposite is observed for the gneisses of south Madagascar, further supporting the novel hypothesis that monazite Eu/Eu^* can reflect changes in $f\text{O}_2$.

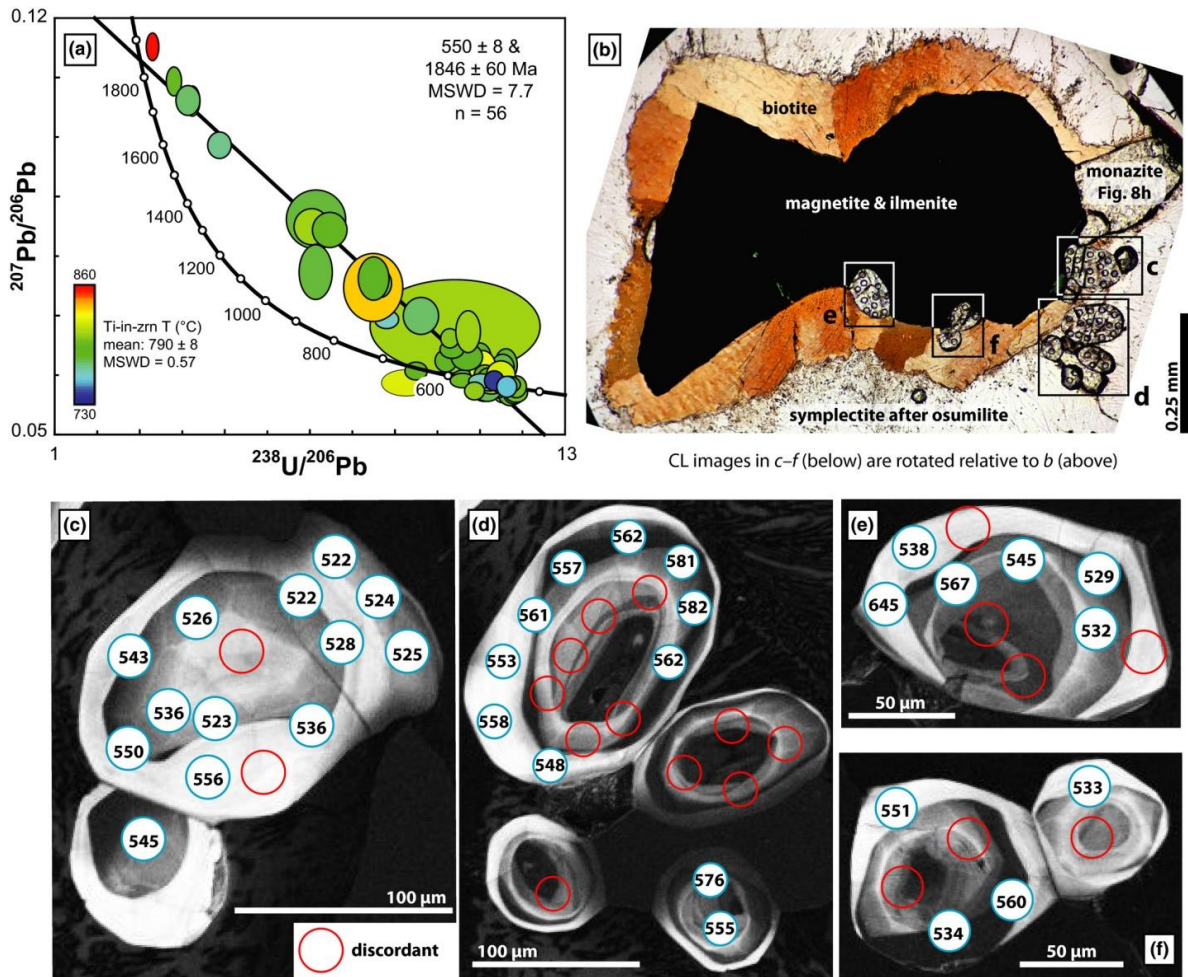


Figure 9. (a) U-Pb zircon dates in osumilite gneiss 23A define a discordia between 1,850 and 550 Ma. Ti-in-zircon temperatures have an average value of 790°C and are not correlated with date (see online version for analyses colored by Ti concentration). (b) Optical photomicrograph showing association of zircon with retrograde biotite corona on magnetite and ilmenite. Monazite grains from the sample are isotopically homogeneous: 561 ± 6 Ma (Figure 8h). (c-f) CL images of zircon in b with LA - ICP - MS spot locations and $^{238}\text{U}-^{206}\text{Pb}$ dates (CL images have been rotated relative to b to better fit on page). Dates from zircon cores are discordant. CL - dark mantles and CL - bright rims are 590–520 Ma.

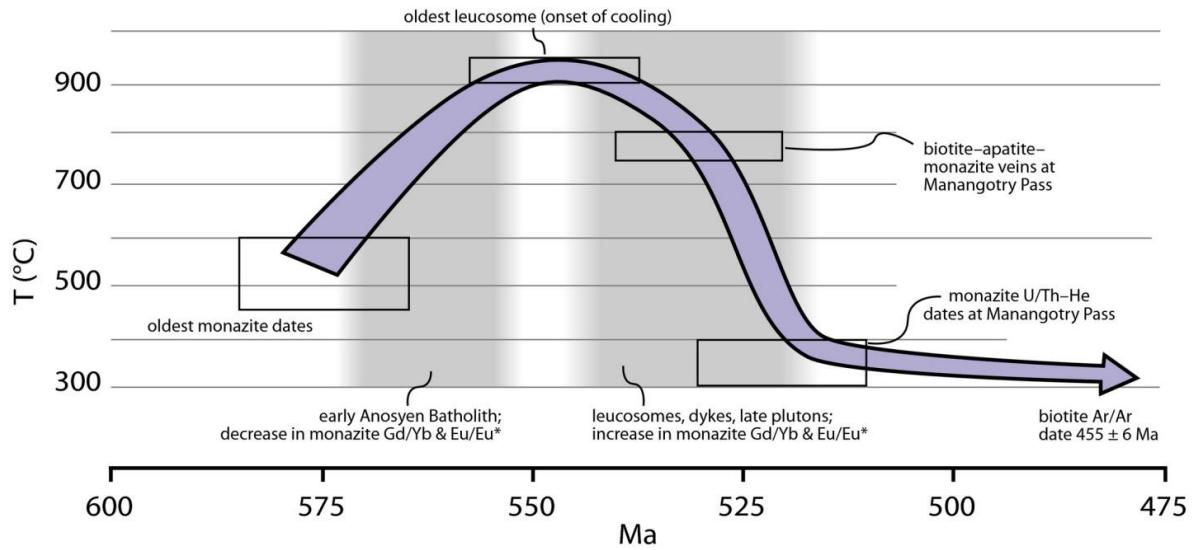


Figure 10. Temperature - time path of the Anosyen domain near Tranomaro and Tôlanaro from U/Th–Pb monazite dates of osumilite gneisses (this study), U/Th–Pb and U/Th–He monazite dates from Manangotry Pass (Montel et al., 2018), magmatic dates (see text for references), and Ar/Ar biotite dates from Manangotry Pass (Montel et al., 2018); the average cooling rate is 17 ± 7 K/Myr for 550–520 Ma.

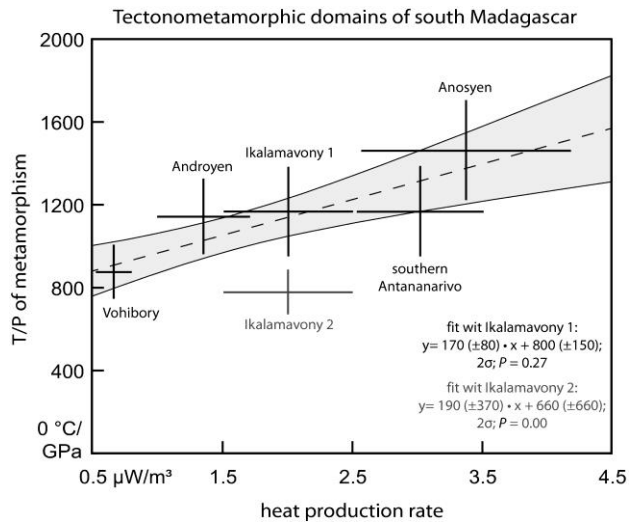


Figure 11. Average heat - production rate of southern Malagasy terranes correlates with the apparent thermal gradient of metamorphism (metamorphic temperature divided by metamorphic pressure). Decay of U, Th and K was an important heat source for high - grade metamorphism at the terrane scale (P–T data from GAF - BGR 2008; Grégoire et al. 2009; Jöns & Schenk 2008; Martelat et al. 1997; and this study).

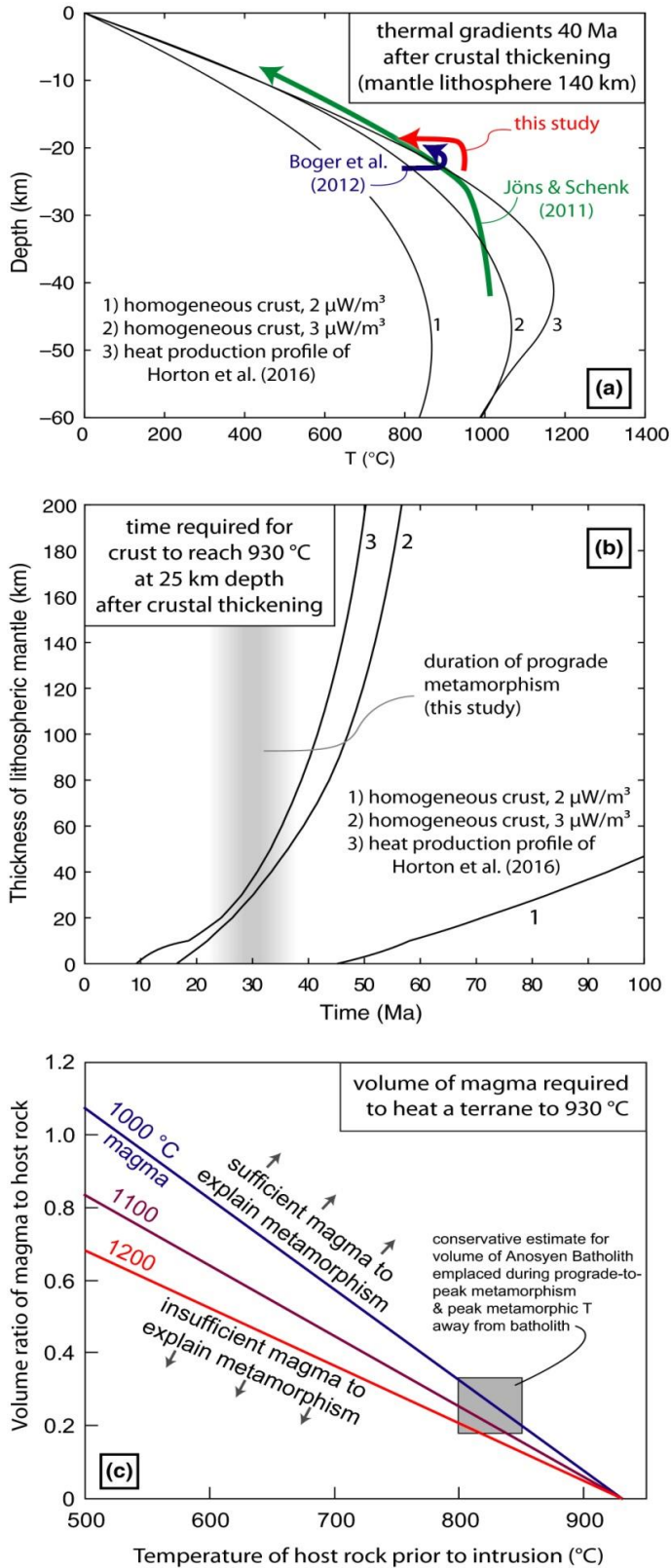


Figure 12. Models of plausible heat sources for UHTM in the Anosyen domain. (a) Model thermal gradients for crust with high radiogenic heat-production rates—and no advective heat transfer—40 Myr after crustal thickening from 30 to 60 km (duration of heating constrained by monazite dates; this study). Average crustal heat-production rates $\geq 3 \mu\text{W}/\text{m}^3$ are necessary for models to reproduce the P–T–t estimates of this study, Boger et al. (2012), and Jöns and Schenk (2011; see Section 5.1 and Appendix S1 for model details). (b) Same models as A, showing the influence of mantle lithosphere thickness on the temperature-time evolution of the crust at 25 km depth. The short duration of prograde metamorphism estimated in this study is best fit with a mantle lithosphere thickness less than 80 km and a highly radiogenic crust. Similarly, thin mantle lithosphere is inferred beneath modern central Tibet (e.g. Jiménez-Munt et al., 2008; Tunini et al., 2016). (c) Energy balance calculations showing the volume of magma required to heat a terrane to 930°C as a function of magma temperature and host - rock temperature prior to intrusion. The volume of the Anosyen Batholith may have been sufficient to explain the difference in peak metamorphic temperature between gneiss with osumilite near the batholith (~930°C) and gneisses without osumilite far away from the batholith (800–850°C). While advection of heat by magmatism is unlikely to have been the dominant source of heat for regional metamorphism, it may have been a locally important addition to the high rates of radiogenic heat production.

CHAPTER 2: *LinT*, A SIMPLIFIED APPROACH TO OXYGEN-ISOTOPE THERMOMETRY AND SPEEDOMETRY OF HIGH-GRADE ROCKS

1: OXYGEN ISOTOPE THERMOMETRY

Urey (1947) predicted the temperature-dependent fraction of oxygen isotopes and foresaw its application as a geothermometer, specifically to determine paleoseawater temperatures from fossils (Urey, Lowenstam, Epstein, & McKinney, 1951). The temperature dependence of oxygen-isotope fractionation among rock-forming minerals was first experimentally calibrated in the 1950's–70's (e.g., Clayton and Epstein, 1958; Taylor et al., 1963; O'Neil and Taylor, 1967; Clayton et al., 1972; Bottinga and Javoy, 1973) and allowed calculation of crystallization temperatures for igneous and metamorphic rocks.

Retrograde diffusion can partially reset the isotopic compositions of minerals, leading to temperature estimates less than those of peak metamorphism, however the oxygen-isotope disequilibrium can be exploited to calculate cooling rates if diffusivities are known (e.g., Javoy, 1977). Using the Dodson equations for instantaneous closure temperature (T_c : Dodson, 1973), Giletti (1986) presented a mathematical formulation for quantifying the oxygen-isotope disequilibrium as a function of cooling rate, grain size, and mineral modes; this was used to calculate cooling rates for granites based on the magnitude of oxygen-isotope disequilibrium among quartz, feldspar, and Ca-amphibole. Eiler, Baumgartner, and Valley (1992) and Kohn and Valley (1998) forward-modeled oxygen-isotope redistribution during cooling of crystalline rocks using the full temperature dependence of oxygen diffusion rate, rather than the instantaneous T_c used by Giletti (1986). The full-diffusion models provide the advantage of being able to predict oxygen-isotope zoning within phases, although

bulk-mineral oxygen-isotope compositions are nearly identical to those predicted by the instantaneous closure-temperature method.

The method of Giletti was expanded by Farquhar et al. (1993, 1996), who presented the method of isotope-exchange trajectories (IET) for extracting the crystallization or near-peak cooling temperatures of slowly cooled rocks. An IET is an equation that describes oxygen-isotope fractionation between a mineral and the bulk rock as a function of temperature. The temperature at which the IET agrees with the measured mineral oxygen isotope compositions is taken to be the T_c of that mineral; each mineral has a different IET. As long as one phase in the rock has a T_c equal to or greater than the peak metamorphic temperature, IET's can be used to calculate crystallization temperatures of plutons and peak-temperatures of ultrahigh-temperature metamorphic rocks.

Hoernes et al. (1994, 1995) and Hagen et al. (2008) recognized that the low diffusivities of oxygen in garnet and kyanite/sillimanite allow peak or near-peak temperatures of crystalline rocks to be extracted from garnet–(kyanite/sillimanite)–whole-rock fractionations alone, without the need to correct for retrograde oxygen diffusion in other phases. These minerals—or any others that remained closed to oxygen diffusion during cooling—will lie on a straight line with the whole-rock value in $A_{\text{min-quartz}}-\delta^{18}\text{O}$ space (A is the oxygen-isotope fractionation factor between each mineral and quartz). The slope of this line is proportional to the temperature at which the minerals equilibrated.

The method used in this paper builds on the theory of Giletti (1986) and can be considered analogous to the IET method of Farquhar et al. (1993, 1996), though the mathematical formulation differs. I reiterate the findings of Farquhar et al. (1993, 1996), Hoernes et al. (1994, 1995), and Hagen et al. (2008): oxygen isotopes can be used to extract

accurate and precise temperatures of the highest-grade rocks independent from—and complementary to—other thermometric techniques. Mineral diffusivities do not need to be known to calculate temperature, but if they are known, non-linear cooling rates can also be calculated.

2: A LINEAR-EQUATIONS APPROACH TO OXYGEN-ISOTOPE RE-EQUILIBRATION THERMOMETRY (*LinT*)

Assuming that minerals have an essentially instantaneous closure temperature to oxygen diffusion (a reasonable approximation for most rocks: Dodson, 1973; Gilotti, 1986) and that the rock remains closed to oxygen-isotope exchange during cooling, the last temperature at which all minerals in the rock were in oxygen-isotope equilibrium—and the oxygen-isotope composition of the minerals at that temperature—can be uniquely determined from measured mineral $\delta^{18}\text{O}$, mineral modes, and the oxygen-isotope fractionation factors among the minerals. This solution comes from solving a set of linear equations that describe the oxygen-isotope fractionations and oxygen mass balance among the minerals. For a rock with three minerals, of which mineral “3” has the highest T_c , the set of equations can be:

$$\delta^{18}\text{O}^{\text{at } T_{\text{min1}}} - (A_{\text{min3}} - A_{\text{min1}})/T^2 = \delta^{18}\text{O}^{\text{measured}}_{\text{min3}} \quad (1)$$

$$\delta^{18}\text{O}^{\text{at } T_{\text{min2}}} - (A_{\text{min3}} - A_{\text{min2}})/T^2 = \delta^{18}\text{O}^{\text{measured}}_{\text{min3}} \quad (2)$$

$$x_{\text{min1}} * \delta^{18}\text{O}^{\text{at } T_{\text{min1}}} + x_{\text{min2}} * \delta^{18}\text{O}^{\text{at } T_{\text{min2}}} = x_{\text{min1}} * \delta^{18}\text{O}^{\text{measured}}_{\text{min1}} + x_{\text{min2}} * \delta^{18}\text{O}^{\text{measured}}_{\text{min2}} \quad (3)$$

(T = temperature in K; x = mineral “oxygen density,” mineral mode * oxygen atoms per formula unit / molar volume; $A_{\text{minX/quartz}}$ = oxygen-isotope fractionation factor between mineral X and quartz). Equations 1 and 2 derive from the fundamental relationship of oxygen-isotope fraction as a function of temperature: $\Delta^{18}\text{O} = A/T^2$. For n minerals in a rock,

there will be $n!/(k!(n-k)!)$ possible equations of this form of which only $n-1$ are necessary to define the oxygen-isotope fractionations among all phases. Equation 3 is a mass balance of oxygen isotopes among the minerals that remained open to oxygen diffusion during cooling. For each additional mineral in the rock beyond three, additional terms of the form $x_{\min}^* \delta^{18}\text{O}_{\min}$ must be added to both sides of equation 3 (examples for possible sets of equations for four- and five-mineral rocks are given in Appendix S4).

T calculated from these equations will be the peak temperature of metamorphism (or the crystallization temperature of a pluton) or $T_{c_{\min 3}}$, whichever is lower. Uncertainties in the calculated temperatures are a function of analytical uncertainty in $\delta^{18}\text{O}$, experimental uncertainty in fractionation factors, and mineral modes; full temperature uncertainties are easily calculated by Monte Carlo simulation. A graphical illustration of the *LinT* method applied to an ultrahigh-temperature garnet–quartz–feldspar gneiss from Madagascar is shown in Figure 1.

If the effective grain size of each mineral and diffusion parameters are known, the instantaneous cooling rates (dT/dt) at each of the mineral T_c 's can be calculated using the equations of Dodson (1973). If dT/dt is calculated at multiple mineral T_c 's within a rock, dT/dt can be defined as a function of T and integrated with respect to time to yield a temperature-time path for the rock—a fundamental goal in petrology.

3: COMPARISON OF *LinT* WITH MODELS AND REAL ROCKS

To evaluate the accuracy of the *LinT* approach, I i) apply *LinT* to synthetic data output from cooling models using fully temperature-dependent expressions for oxygen diffusion (Kohn and Valley, 1998) and ii) apply *LinT* to three ultrahigh-temperature gneisses from

Madagascar and compare the resulting temperatures to independent temperature estimates from the same terrane.

3.1: Comparison with the model schist of Kohn and Valley (1998)

Kohn and Valley (1998) forward-modeled oxygen-isotope re-equilibration during cooling of a hypothetical quartz–plagioclase–muscovite–biotite schist using a fully temperature-dependent description of oxygen diffusion rate in each mineral and allowing zoning to develop within each mineral. *LinT* was applied to the final oxygen-isotope compositions and modes of each mineral in the Kohn–Valley model (i.e., the values that would have been measured, had it been a real rock). From *LinT*, the last temperature at which all minerals were in equilibrium was 456°C (interpreted to be $T_{C_{\text{quartz}}}$) and the last temperature at which muscovite, biotite, and plagioclase were in equilibrium was 353°C (interpreted to be $T_{C_{\text{muscovite}}}$). These T_c 's are nearly identical to the Dodson T_c 's calculated from the dT/dt and grain sizes prescribed in the forward model: 470°C (quartz) and 335°C (muscovite). Plotting each of the linear equations in $\delta^{18}\text{O}$ – T space (effectively the same as generating IET's by the method of Farquhar et al., 1993), shows that the calculated $\delta^{18}\text{O}$ of all minerals at all temperatures differs by less than 0.1 ‰ from the full diffusion model of Kohn and Valley (Figure 2). Assuming a hypothetical analytical uncertainty of 0.1 ‰ (2σ) for $\delta^{18}\text{O}$ in each mineral, the precision of the T_c 's calculated by *LinT* are $\pm 12^\circ\text{C}$ ($T_{C_{\text{quartz}}}$) and $\pm 48^\circ\text{C}$ ($T_{C_{\text{muscovite}}}$).

Instantaneous dT/dt 's calculated at the *LinT* T_c 's of quartz and muscovite are 2.2 and 13 K/Myr, respectively. The prescribed dT/dt in the Kohn–Valley forward model was a constant 5 K/Myr, suggesting that dT/dt calculated by inversion of *LinT* temperatures should only be

considered accurate within a factor of 3. This is due to the exponential relationship between closure temperature and dT/dt in the Dodson (1973) equation; small uncertainties in closure temperature correspond to large uncertainties in dT/dt .

3.2: Comparison with ultrahigh-temperature granulites of Madagascar

Ultrahigh-temperature granulites in the Anosyen domain of southern Madagascar are metapelitic, calc-silicate, and felsic paragneisses metamorphosed between 590 and 510 Ma (see Tucker et al., 2014, and references therein). Because the peak temperatures have been consistently estimated at 900–1000°C (Jöns and Schenk, 2011; Boger et al., 2012; Horton et al., 2016; Chapter 1), these rocks provided an ideal case study to compare results of *LinT* with other modern thermometric techniques. I chose three samples from near Tôlanaro, because of their simple, unretrogressed mineral assemblages; all three are garnet–quartz–ternary-feldspar gneisses with <5 total volume percent other phases (mainly sillimanite, ilmenite, and Al-spinel).

Twenty five cm³ of each sample was crushed and separated into 350–850 µm diameter fragments. Unweathered, inclusion-free grains of quartz, perthite, and garnet were then picked by hand. Aliquots of 1–2 mg of each mineral were measured at the Center for Stable Isotopes at the University of New Mexico, Albuquerque, using the laser-fluorination method of Sharp (1990). The analytical precision of the measurements was ~0.1‰ [2σ] based on repeated analyses of a reference quartz measured periodically throughout the analytical session. Quartz and feldspar mineral modes were determined from pixel counting of back-scattered electron images of whole thin sections. For comparison, two oxygen-isotope fractionation factors were used for quartz–garnet: that of Sharp (1995) and that of Valley et

al. (2003), the former yielding higher temperatures. The quartz–feldspar fractionation factor used is from Clayton et al. (1989) for $X_{\text{anorthite}} = 0.15 \pm 0.05$. Results are shown in Table S1 and Figure 3.

Using the Valley et al. (2003) value for quartz–garnet fractionation, the calculated temperatures at which the quartz, feldspar, and garnet were in oxygen isotope equilibrium ranges from 899 to 960°C with a weighted mean of $927 \pm 31^\circ\text{C}$ (2σ). Using the quartz–garnet oxygen isotope fractionation factor of Sharp (1995), temperatures range from 1009 to 1069°C with a weighted mean of $1037 \pm 34^\circ\text{C}$ (2σ). These values agree with peak metamorphic temperatures calculated from feldspar-solvus thermometry ($>910\text{--}930^\circ\text{C}$; Chapter 1) and Zr-in-rutile thermometry ($930 \pm 45^\circ\text{C}$; Horton et al., 2016) and pseudosections ($880\text{--}920^\circ\text{C}$, Boger et al., 2012; or $>930^\circ\text{C}$, Chapter 1). The agreement of $\text{Lin}T$ temperatures with independent estimates of peak metamorphic temperature suggests that $T_{\text{c}_{\text{garnet}}}$ is equal to or greater than the peak temperature of metamorphism, consistent with interpretations of previous studies (Hoffbauer, Hoernes, & Fiorentini, 1994; Z. D. Sharp, 1995). The temperatures calculated from $\Delta^{18}\text{O}_{\text{quartz-feldspar}}$ are 498 to 638°C and are interpreted to be the T_{c} 's of quartz. The temperatures calculated from $\Delta^{18}\text{O}_{\text{quartz-garnet}}$ are 740 to 819°C (calibration of Valley et al., 2003; shown in Figure 3) or 810–896°C (calibration of Sharp, 1995); these are minimum temperatures of metamorphism, because $\Delta^{18}\text{O}_{\text{quartz-garnet}}$ can only increase during cooling (Figure 1).

Instantaneous dT/dt can be calculated from $T_{\text{c}_{\text{quartz}}}$ using the equations of Dodson (1973). The grain sizes for the minerals in each sample are similar, but each mineral has a distribution of grain sizes, such that the “effective grain radius” to be used in the Dodson equation is unclear. To account for this variability, I propagate a large uncertainty in grain

radius through each cooling-rate calculation: 0.6 ± 0.3 mm; this is the largest contribution to the uncertainty in dT/dt presented below. Quartz was modeled as a plane sheet, because oxygen diffusion in quartz along the c-axis is much faster than perpendicular to the c-axis (e.g., Sharp et al. 1991). The lack of hydrous, retrograde minerals in these rocks suggests that these rocks did not have a free fluid phase during cooling. Using the “dry” diffusion parameters of alpha quartz (parallel to the c-axis) from Sharp et al. (1991) yields dT/dt of 1–55 K/Myr at the times of quartz closure. This range of dT/dt , 1–55 K/Myr, calculated for the three samples, reflects the range in permissible values for the combined uncertainties in grain size, T_c 's, and $\delta^{18}O_{\text{minerals}}$.

For garnet, the agreement of $LinT$ with independent estimates for peak metamorphic temperatures indicate that $T_{c_{\text{garnet}}}$ is equal to or greater than the peak temperature of metamorphism. No “dry” diffusion data are available for almandine-rich garnet, but if they were, they could be used to calculate minimum dT/dt .

The 75 Myr difference in age between the onset of cooling at 555 ± 11 Ma (oldest monazite leucosome date; $T \sim 940^\circ\text{C}$, Chapter 1) and 530–510 Ma monazite He dates (Montel et al., 2017; $300 \pm 50^\circ\text{C}$) implies an average dT/dt of 17 ± 7 K/Myr, consistent with the range of permissible dT/dt calculated from $T_{c_{\text{quartz}}}$ (although these are imprecise). In more mineralogically complex samples, $LinT$ could be used to calculate different instantaneous dT/dt for each $T_{c_{\text{mineral}}}$, defining dT/dt as a function of T . Alternatively, in rocks with effectively binary mineral assemblages in which one mineral is much more abundant than the other (such minor magnetite in a marble), dT/dt could be evaluated as a function of T by measuring $\delta^{18}O$ of the minor phases as a function of grain size as explained by Sharp (1991).

4: CONCLUSIONS

I presented a new mathematical approach (*LinT*) to the application of oxygen-isotope thermometry that requires only mineral $\delta^{18}\text{O}$, modes, and fractionation factors. Grain size, cooling rate, and diffusion parameters are not needed for the extraction of meaningful temperature information, but if they are known, mineral T_c 's can be used to calculate temperature-dependent cooling rates to within a factor of 2–3. Temperatures were calculated for ultrahigh-temperature gneisses from south Madagascar— $921 \pm 30^\circ\text{C}$ or $1037 \pm 34^\circ\text{C}$, depending on the calibration used—consistent with two-feldspar thermometry, Zr-in-rutile thermometry, and pseudosections. Cooling rates calculated from $T_{c\text{quartz}}$ are consistent with the cooling rate calculated from thermochronology.

The most-precise oxygen-isotope temperatures will be obtained from rocks that contain minerals with a large range in fractionation factors, such as quartz with garnet, pyroxene, or kyanite/sillimanite (Figure S3: Sharp, 1995; Valley et al., 2003; Valley, 2003). The highest temperatures will be obtained if the diffusion rate of oxygen in at least one mineral is slow enough that its T_c is equal to or greater than the peak temperatures of high-grade metamorphic rocks or the emplacement temperatures of plutons. The best candidates for this are garnet and kyanite/sillimanite (Hoffbauer et al., 1994; Sharp, 1995; this study). Oxygen-isotope thermometry is particularly well suited to high-temperature quartz–garnet-bearing rocks with low-variance mineral assemblages (rocks that are problematic for precise phase-equilibria modeling).

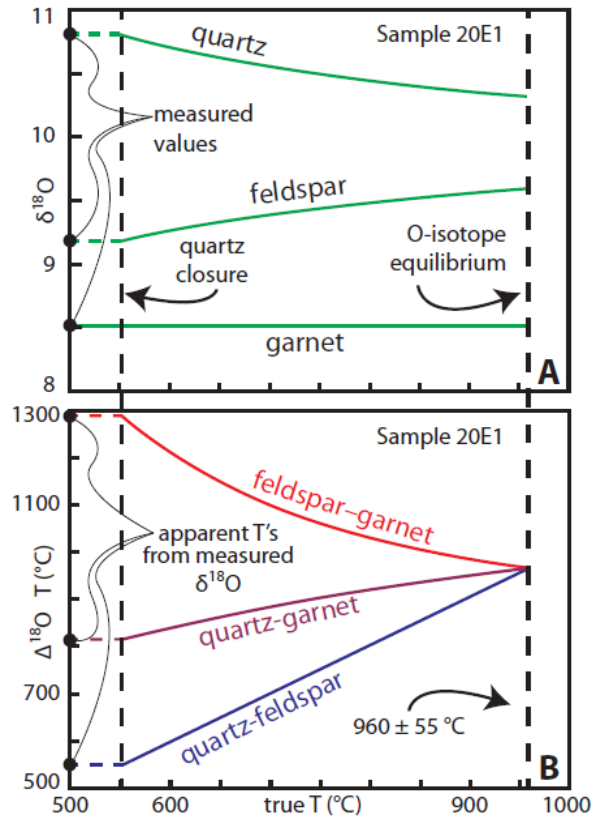


Figure 1. Graphical illustration of the system-of-linear-equations approach to high-temperature oxygen-isotope thermometry (*LinT*) as applied to an ultrahigh-temperature gneiss from Madagascar. A) Constrained by mass balance and equilibrium fractionation, $\delta^{18}\text{O}_{\text{quartz}}$ and $\delta^{18}\text{O}_{\text{feldspar}}$ are adjusted (while $\delta^{18}\text{O}_{\text{garnet}}$ is held constant, because it has the slowest relative oxygen diffusivity) until the quartz–garnet and feldspar–garnet temperatures are identical. This is the last temperature at which all three minerals were in equilibrium: either the closure temperature of garnet or the peak temperature of metamorphism, whichever is lower. B) The same data shown in A recast as oxygen-isotope apparent temperatures against “true temperature” to illustrate how the *LinT* method works: by solving for the temperature at which all oxygen-isotope apparent temperatures agree.

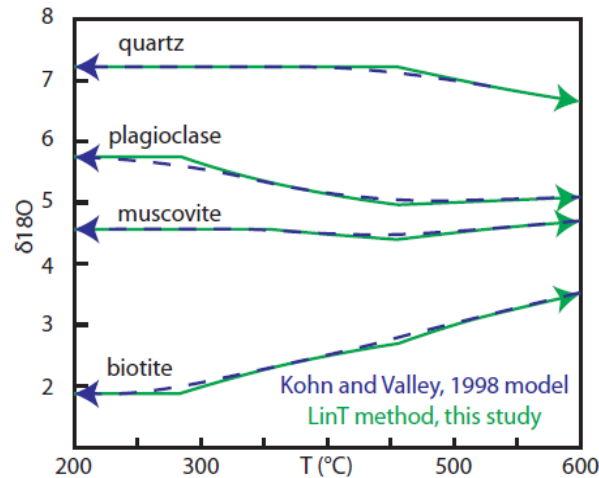


Figure 2. Comparison of a forward model of oxygen-isotope reequilibration during cooling (Kohn and Valley, 1998; blue arrows)—using a whole-rock composition, temperature-dependent parameterizations of oxygen diffusion rates in each mineral, oxygen-isotope fractionation factors among all minerals, mineral modes, and a cooling rate to predict how oxygen-isotope compositions change *down-temperature*—with the *LinT* method, which uses measured mineral $\delta^{18}\text{O}$, oxygen-isotope fractionation factors, and modes to calculate $\delta^{18}\text{O}$ of each mineral *up-temperature*. The differences in the models are ≤ 0.1 ‰ for each mineral at any temperature.

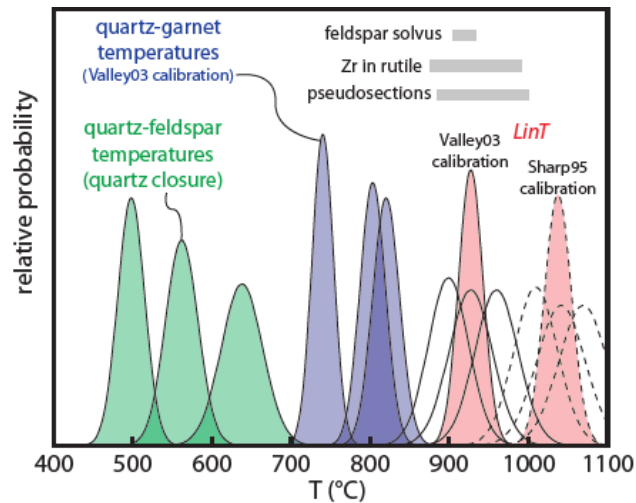


Figure 3. Despite different amounts of retrograde oxygen-isotope exchange between quartz and feldspar in each sample—evident from the differences between quartz–feldspar and quartz–garnet apparent temperatures among samples—oxygen-isotope temperatures calculated by *LinT* agree with each other (weighted mean: $927 \pm 31^\circ\text{C}$ or $1037 \pm 34^\circ\text{C}$ [2σ] depending on the garnet–quartz calibration used) and with independent temperature estimates from feldspar-solvus thermometry (Chapter 1), Zr-in-rutile thermometry (Horton et al., 2016), and pseudosections (Boger et al., 2012; Chapter 1) of rocks in the same terrane.

CHAPTER 3: INTERPRETING TITANITE U–Pb DATES AND Zr THERMOMETRY; EMPIRICAL CONSTRAINTS ON ELEMENTAL DIFFUSIVITIES OF Pb, Al, Fe, Zr, Nb, AND Ce

1: THE PETROCHRONOMETER TITANITE

U–Pb titanite ($\text{Ca}[\text{Ti,Al,Fe}^{3+}]\text{SiO}_4[\text{O,OH,F,Cl}]$) dates can record neocrystallization and growth (Corfu, 1996; Kohn & Corrie, 2011; Scott & St-Onge, 1995; Spencer et al., 2013; Stearns, Cottle, Hacker, & Kylander-Clark, 2016; Stearns, Hacker, Ratschbacher, Rutte, & Kylander-Clark, 2015; Verts, Chamberlain, & Frost, 1996), recrystallization during deformation (Bonamici, Fanning, Kozdon, Fournelle, & Valley, 2015; Spencer et al., 2013), alteration/reaction with a fluid (Corfu, 1996; Garber, Hacker, Kylander-Clark, Stearns, & Seward, 2017; Marsh & Smye, 2017), and possibly cooling (Cherniak, 1993). Criteria for interpreting the significance of titanite U–Pb dates based on elemental and isotopic zoning are discussed by Stearns et al. (2015). The Zr content of titanite has been calibrated as a thermobarometer (Hayden, Watson, & Wark, 2008) and titanite commonly contains many other trace elements that can be used to relate dates to physical conditions (pressure, temperature, mineral assemblage) of neocrystallization, growth, dynamic recrystallization, or alteration (Garber et al., 2017). Unlike zircon, titanite reacts with many rock-forming minerals, making it useful for conventional thermobarometry (Table 2 of Frost et al., 2001), further allowing U–Pb titanite dates to be tied directly to physical conditions of magmatism and metamorphism (e.g., Scott and St-Onge, 1995).

Although titanite is a versatile petrochronometer, interpretations of U–Pb titanite dates are limited by uncertainties in the diffusivities of petrochronologically important elements such as Pb, Zr, Al, Fe, Nb, Ta, and REE. Experiments suggest that typical metamorphic titanite grains (~100- μm diameter cooled at 10 K/Myr) should have a whole-grain closure

temperature to Pb diffusion of $\sim 575^{\circ}\text{C}$ (Cherniak, 1993), to Zr diffusion of $\sim 675^{\circ}\text{C}$ (Cherniak, 2006), to Nb and Ta diffusion $\sim 725^{\circ}\text{C}$ (Cherniak, 2015), and to Sr and Nd diffusion of $\sim 800^{\circ}\text{C}$ (Cherniak, 1995). As discussed below (sections 2.2 and 2.3), however, empirical constraints on elemental mobility in titanite suggest that Fickian diffusion is negligible at temperatures $\leq 800^{\circ}\text{C}$. Empirical studies have also shown that processes other than Fickian diffusion—such as fluid-mediated dissolution–precipitation reactions, neocrystallization, and possibly deformation—are more important than Fickian diffusion for resetting U–Pb dates, Zr temperatures, and other elemental concentrations in most titanite.

2: ESTIMATES FOR THE U–Pb CLOSURE TEMPERATURE AND ELEMENTAL DIFFUSIVITIES IN TITANITE

As summarized in this section, empirical studies suggest that (1) titanite can retain U–Pb dates and trace-element zoning to temperatures $\geq 800^{\circ}\text{C}$, and (2) several processes—chiefly fluid-mediated dissolution-precipitation reactions (“interface-coupled dissolution–precipitation”; Putnis, 2009) and new titanite growth—are more important than Fickian diffusion for resetting U–Pb dates and compositions in most rocks.

2.1: Empirical TIMS studies of the U–Pb closure temperature in titanite

Mattinson (1978) dated titanite and zircon from several granitic plutons in the Salinian block of California, USA. He found titanite dates that are younger than zircon U–Pb dates by several Myr, but agree with K–Ar hornblende dates. Based on the agreement of titanite and hornblende dates, Mattinson concluded that titanite has a closure temperature of $\sim 500^{\circ}\text{C}$ for the U–Pb system.

Tucker et al. (1987, 1990, 2004) dated titanite in gneiss from the Western Gneiss region, Norway. All of the dates define a discordia between inherited and metamorphic components. The degree to which the titanite grains were reset correlates with metamorphic grade. Tucker et al. interpreted this correlation to reflect variable degrees of diffusive Pb loss over a 550–750°C temperature range during a short-lived metamorphic event. Kylander-Clark et al. (2008) also dated titanite from the Western Gneiss region, and noted that while the general correlation between degree-of-resetting and metamorphic grade holds over a broad region, data from several samples preclude a simple interpretation of diffusive Pb loss as the main mechanism controlling U–Pb titanite dates. Two of their samples reached temperatures $\geq 700^\circ\text{C}$, but preserved strongly inherited U/Pb isotope ratios despite having smaller titanite grains than nearby rocks that were completely reset. Another sample yielded a date 5–8 Myr older than dates from samples nearby despite metamorphic temperatures of 700–750°C. Kylander-Clark et al. proposed that the U–Pb titanite dates from the Western Gneiss region are better explained as (re)crystallization, rather than cooling, ages. This hypothesis was later supported by the extensive in-situ dating and titanite imaging of Spencer et al. (2013) and Garber et al. (2017; see section 2.3).

Mezger et al. (1991, 1993) dated titanite, monazite, garnet, and rutile from the Grenville Orogen in New York and Ontario. They found that titanite U–Pb dates are the same or younger than monazite U–Pb dates, but older than hornblende K–Ar and $^{40}\text{Ar}/^{39}\text{Ar}$ dates. By interpolating between an assumed monazite U–Pb closure $T \approx 700^\circ\text{C}$ and a hornblende K–Ar closure $T \approx 500^\circ\text{C}$, the closure temperature of titanite U–Pb was determined to be $T \approx 500\text{--}670^\circ\text{C}$, depending on grain size. Subsequent experimental (Cherniak, Watson, Grove, & Harrison, 2004) and empirical (McFarlane & Harrison, 2006) estimates of Pb diffusivity in

monazite and studies documenting incomplete resetting of monazite during ultrahigh-temperature metamorphism (e.g., Chapter 1) suggested that the interpretation of monazite U–Pb dates as cooling ages is inappropriate. The results of Mezger et al. therefore indicate that titanite U–Pb dates must have a higher closure temperature than hornblende K–Ar dates ($>500^{\circ}\text{C}$), but do not provide an upper temperature constraint.

Scott and St-Onge (1995) dated metamorphic titanite from mafic tonalite gneisses that reached $660\text{--}700^{\circ}\text{C}$ in the Ungava/Trans-Hudson Orogen, Canada. In one sample, all of the titanite yielded identical dates despite a large range in grain size: $75\text{--}1000\text{ }\mu\text{m}$. Scott and St-Onge's interpretation that the dates reflect metamorphic titanite growth requires that the closure temperature for Pb is greater than 700°C . This interpretation is consistent with local K–Ar hornblende dates that are $150\text{--}200\text{ Myr}$ younger than the titanite U–Pb dates: such slow cooling should have enabled diffusive Pb loss and grain size-dependent dispersion of U–Pb dates if the temperature for Pb closure is $<700^{\circ}\text{C}$.

Pidgeon et al. (1996) dated titanite, zircon, and apatite from a metamorphosed syenite in the Yilgarn Craton. They dated whole titanite grains and fragments of different colors corresponding to different concentrations of U and Th. The titanite and zircon dates define a discordia between the inferred timing of $\sim 650^{\circ}\text{C}$ metamorphism and an inherited magmatic/xenocrystic age. The preservation of inherited dates suggests that the closure temperature for Pb in titanite is $>650^{\circ}\text{C}$. A titanite date from a nearby amphibolite is 60 Myr older than titanite in the syenite, despite having experienced the same metamorphic event. Pidgeon et al. suggested that this might be related to differences in titanite stability dictated by bulk compositions (syenite vs. amphibolite), implying that processes other than volume diffusion controlled the degree to which titanite was reset during metamorphism.

Verts et al. (1996) dated titanite along a transect through a contact aureole in the Laramie Anorthosite Complex, USA. In samples that reached $T > 700^{\circ}\text{C}$, U–Pb dates were found to be completely reset. In samples that equilibrated at lower temperatures, titanite dates are scattered between an inherited age and the age of contact metamorphism. In the samples that reached $T < 700^{\circ}\text{C}$, paler titanite is generally younger than darker titanite, supporting an interpretation of growth at different conditions. Verts et al. constructed models for the amount of diffusive Pb loss predicted by the experimental Pb diffusion parameters of Cherniak (1993) as a function of distance from the pluton. They interpreted the results to indicate $\sim 650^{\circ}\text{C}$ as a reasonable closure temperature for Pb in titanite, in general agreement with Cherniak (1993), but also acknowledged that new titanite growth occurred throughout the contact aureole.

Corfu (1996) dated gneisses, plutons, and dikes of the Winnipeg River Subprovince, Canada. Differences in titanite dates from samples within 20 m of each other led Corfu to conclude that local processes, such as “focused fluid activity” were a more probable explanation for titanite resetting than diffusive Pb loss. This was corroborated by the recognition that their younger titanite grains have a distinct color (paler) and composition than older titanite within individual samples; the paler titanite was observed mantling darker titanite in thin section, commonly adjacent to biotite and, to a lesser extent, white mica and epidote (hydrous minerals). Corfu also interpreted the presence of xenocrystic titanite in a diorite to indicate that Pb diffusion was not fast enough to reset titanite at intermediate magmatic temperatures. He concluded that the closure temperature for Pb diffusion in titanite must be $> 650^{\circ}\text{C}$ and that “It would be inappropriate to interpret the titanite ages in terms of slow cooling.” Growth of titanite (or possibly dissolution–reprecipitation of preexisting

titanite) from fluid flow at low to moderate temperatures ($T < 700^{\circ}\text{C}$) was also documented by Corfu et al. (1994) and Corfu and Muir (1989), providing further evidence for resetting U–Pb titanite dates by processes other than Fickian diffusion.

Schärer et al. (1994) and Zhang and Schärer (1996) dated titanite from a syenite in the Red River Shear Zone, China. They found two generations of concordant, Cenozoic titanite that they interpreted to be magmatic, and discordant analyses dispersed toward an inherited, Precambrian age. Based on the preservation of the inherited component and an inferred magmatic temperatures of 700°C , they suggested that the closure temperature for Pb in titanite is $>700^{\circ}\text{C}$.

In summary, TIMS U–Pb titanite dates have yielded imprecise constraints on the closure temperature of Pb. Some studies have argued for a closure temperature similar to that predicted by experiments, but also acknowledged the importance of neo- or re-crystallization in resetting bulk titanite dates. Other studies have clearly demonstrated that a closure temperature $\geq 700^{\circ}\text{C}$ is required to explain magmatic inheritance and the heterogeneity of metamorphic dates (independent of grain size) from individual localities.

2.2: Empirical LA-ICP-MS studies of the U–Pb closure temperature and elemental mobility in titanite

In-situ dating of titanite by LA-ICP-MS has provided the most rigorous evaluation of elemental mobility in titanite, particularly when coupled to grain-scale mapping of titanite composition. By documenting the absence of elemental diffusion profiles in individual titanite grains, these studies have shown that processes other than Fickian diffusion reset dates and composition in natural titanite that reached temperatures up to $800\text{--}850^{\circ}\text{C}$. These

in-situ empirical studies suggest that Zr and Pb diffusivities (and presumably many other elements) in titanite may be more than four orders of magnitude slower in nature than in experiments.

Kohn and Corrie (2011) and Walters and Kohn (2016) conducted LA-ICP-MS analyses of titanite in calc-silicate gneisses from the Greater Himalayan Sequence, Nepal. U–Pb dates and Zr temperatures were preserved through 20 Myr of high-temperature metamorphism at a peak of 775–800°C (Kohn and Corrie, 2011) and sector zoning was preserved in grains heated to 800–850°C for 10 Myr (Walters and Kohn, 2016). Individual depth profiles (Kohn and Corrie, 2011) show heterogeneity preserved at the μm scale. These two studies indicate that U, Pb, and Zr were diffusively immobile at the μm scale to temperatures $\geq 800^\circ\text{C}$.

Gao et al. (2012) dated titanite from the Central Dabie Orogen, China, by LA-ICP-MS spot analyses. They found inherited, magmatic titanite cores preserved within younger, metamorphic titanite in gneisses subducted to $>1.5\text{--}2$ GPa and 800–850°C. The two generations of titanite have distinct major- and trace-element compositions. Dates of the cores and rims do not define a discordia suggestive of diffusive Pb loss during heating; rather, the rims were interpreted to reflect new titanite growth.

Spencer et al. (2013) dated titanite from >150 samples from the Western Gneiss region, Norway, by LA-ICP-MS spot analyses—the same region where Kylander-Clark et al. and Tucker et al. conducted TIMS studies. Inherited magmatic titanite dates are preserved in rocks that reached metamorphic temperatures of 700–800°C for as long as 15 Myr. Other titanite dates were found to be the same as $^{40}\text{Ar}/^{39}\text{Ar}$ white mica dates (closure temperature $\approx 400^\circ\text{C}$) from the same outcrops. The dichotomy of inherited dates and dates that correspond to temperatures as low as 400°C—coupled with BSE imaging of titanite grains that show

subgrains, sharp compositional steps, and discontinuous lobate zoning sometimes referred to as “patchy”—suggested to Spencer et al. that processes such as “fluid flow, deformation, and reaction” were more important than Fickian Pb diffusion in resetting titanite dates. Spencer et al. noted that, “When all of the titanite dates are considered together... there is an overall pattern similar to that recognized farther north by Tucker et al. (1990),” but that this pattern cannot be explained solely by Pb diffusion in light of additional petrographic and petrologic data.

Garber et al. (2017) also dated titanite from the Western Gneiss region, Norway, by LA-ICP-MS spot analyses. Through EPMA mapping, BSE imaging, EPMA measurements of halogen contents, and LA-ICP-MS trace-element compositions, Garber et al. recognized three distinct titanite populations: 1) inherited igneous titanite, 2) metamorphic titanite that recrystallized from the igneous titanite by fluid-mediated dissolution–reprecipitation reactions, and 3) neocrystallized titanite. In titanite from the hottest part of the orogen (~800°C), they found that titanite U–Pb dates, but not REE-Th-U concentrations, were partially reset; they interpreted this to be evidence for Pb, but not REE-Th-U, diffusion, although no demonstrable diffusion profiles in single grains were found. In colder portions of the orogen (~700°C), variability in U–Pb dates and REE-Th-U concentrations was interpreted to reflect analytical mixing between different generations of titanite (re)crystallization, but not volume diffusion of Pb-REE-Th-U. In aggregate, their results suggest that Pb may be diffusively mobile at temperature slightly higher than 800°C, but that most other trace elements (U, Th, REE, Zr) are not.

Bonamici et al. (2015) measured O isotopes and U–Pb profiles in titanite from the Adirondacks, New York. The $\delta^{18}\text{O}$ exhibited continuous core-rim zoning interpreted to

reflect partial diffusive reequilibration during cooling. U–Pb dates were found to be generally younger near grain rims, but did not exhibit the same smooth core-rim decrease seen in $\delta^{18}\text{O}$. Bonamici et al. interpreted the general core-rim decrease in U–Pb dates to be the result of diffusive Pb loss, but that the profiles were complicated by local resorption, growth, and possibly dynamic recrystallization at temperatures below T_c^{Pb} , but above T_c^{O} . Because the results of Bonamici et al. are based, in part, on the experimentally derived diffusion parameters of O and Pb, they cannot be used to provide independent estimates of elemental mobilities; however, their U–Pb profiles provide additional support for the hypothesis that titanite U–Pb dates can be reset by processes other than diffusion.

Stearns et al. (2015) dated titanite from 60 igneous and metamorphic rocks in lower-crustal domes in the Pamir Plateau by LA-ICP-MS. They found that individual samples recorded U–Pb dates and Zr temperatures corresponding to ≥ 10 –20 Myr of metamorphism at 650–700°C, suggesting that Pb diffusion was not significant at this temperature. In other samples they noted that all titanite grains yielded the same U–Pb date, despite order-of-magnitude differences in grain size. In aggregate, Stearns et al. suggested that temperatures $> 700^\circ\text{C}$ are necessary for significant Pb and Zr diffusion in titanite and that processes resulting in new titanite growth or recrystallization of preexisting titanite were more important than volume diffusion in their samples. They also outlined criteria—based on elemental and isotopic zoning—for differentiating between diffusional Pb loss and (re)crystallization processes when interpreting U–Pb titanite dates.

Stearns et al. (2016) measured near-rim zoning in titanite U, Th, Pb, and Zr from gneiss domes in the Pamir Plateau, by single-shot LA-ICP-MS depth profiles. Although U, Th, Pb, and Zr all exhibited near-rim zoning that could be fit reasonably well by analytical

expressions for diffusion profiles, the apparent length scales of diffusion in all of the elements are identical and do not scale with elemental diffusivity. The down-hole variation in Zr temperature and U–Pb dates revealed temperature–time histories consistent with independent estimates for the thermal history of the gneiss domes. Stearns et al. concluded that there was no evidence for elemental diffusion in titanite depth profiles from rocks that resided at $T = 750\text{--}800^\circ\text{C}$ for tens of Myr.

Marsh and Smye (2017) dated titanite from mafic granulites of the Grenville Orogen, Canada, by LA-ICP-MS spot analyses. They found no core-to-rim variability in U–Pb dates, despite peak metamorphic temperatures of 800°C , confirming the general findings of the previously discussed studies. Near-rim steps and gradual gradients in trace-element concentrations were both interpreted to be the result of fluid-mediated reactions. These interpretations are discussed in more detail in section 6.

3: STUDIED SAMPLES

Two titanite-bearing samples were chosen from the gneisses of southern Madagascar metamorphosed during the Ediacaran–Cambrian continental collision between East and West Gondwana (Figure 1: Collins et al., 2012; Tucker et al., 2014; Boger et al., 2015; Fitzsimons, 2016).

Titanite 12D is a 1 cm euhedral titanite grain from a roadcut of calc-silicate gneiss in the Ikalamavony domain, between Zazafotsy and Ankaramena, where metamorphism reached temperatures of $\sim 750^\circ\text{C}$ (GAF-BGR, 2008b). Near-rim zoning in the titanite was measured by a combination of LA-ICP-MS and EPMA (Figure 2). First, the titanite was mounted in epoxy with its crystal face exposed for depth profiling of U, Th, Pb, and Zr by LA-ICP-MS

(Figures 3, 4; Table S1). Four depth profiles were measured as a check for reproducibility. Following depth profiling, the sample was cut perpendicular to the profiled grain face and polished until two of the laser pits were visible and then mapped by EPMA to evaluate the near-rim zoning of Al, Fe, Ce, Zr, and Nb complementary to the LA-ICP-MS depth profiles (Figure 5; Table S2). The length scales of near-rim compositional gradients (or their absence) were used to estimate elemental diffusivities (Table S3).

Titanite 21B is a 0.5 cm crystal in thin section collected in Tranomaro, along the river directly across from the gendarmerie. It comes from the Anosyen domain, which contains the highest-grade, osumilite-bearing metamorphic rocks in south Madagascar (900–1000°C: Jöns and Schenk, 2011; Boger et al., 2012; Horton et al., 2016; Chapter 1). EPMA maps of Al, Fe, Zr, Nb, and Ce as well as an LA-ICP-MS map of U–Pb dates were made to evaluate the length scales of compositional and isotopic zoning (Figure 6). Steep compositional gradients observed in EPMA maps (Figure 6; Table S4) were modeled as diffusively relaxed compositional steps to estimate elemental diffusivities (Figures 7, 8; Table S5). The length scale of differences in U–Pb dates within the titanite (Figure 9; Table S6) were used to constrain intracrystalline Pb diffusivity and the differences in U–Pb dates around the rim of the grain were used to assess whether grain-boundary conditions affected the preservation of U–Pb dates.

4: METHODS

4.1: Laser-ablation split-stream inductively coupled plasma mass spectrometry (LA-ICP-MS)

One thousand twenty-six LA-ICP-MS spot analyses were conducted on a single titanite grain in a thin section from sample 21B to assess grain-scale heterogeneity in U–Pb dates. U/Th–Pb dates and trace-element compositions were measured using the split-stream procedure described by Kylander-Clark et al. (2013) and Kylander-Clark (2017). This section focuses on the details of the less well established technique of LA-ICP-MS depth profiling: the measurement of 100-nm scale variability in composition and isotopic ratios within a laser pit by measuring the analyte released by individual pulses of the laser (“single-shot” LA-ICP-MS: (Cottle, Kylander-Clark, & Vrijmoed, 2012; Stearns et al., 2016; Viète, Kylander-Clark, & Hacker, 2015) or from extracting individual data collected during continuous firing of the laser at a low repetition rate (Kohn & Corrie, 2011).

Four depth profiles were measured perpendicular to a titanite crystal face in sample 12D using the continuous firing method (Figures 3, 4; Table S1). Ca, Ti, and Zr were measured on an Agilent 7700x ICP-MS. U, Th, and Pb were measured on a Nu Plasma HR ICP-MS. The spot diameter was 40 μm and the laser fluence was 2.4 J/cm^2 . Each depth profile was measured by firing the laser at 2 Hz for 150 seconds. The titanite was cut perpendicular to the measured crystal face after laser ablation to measure the pit depths (19 μm) and to map near-rim Zr, Nb, Ce, Al, and Fe concentrations in two dimensions by EPMA (Figure 5; section 4.2) as a complement to the one-dimensional LA-ICP-MS data. The time resolution of the LA-ICP-MS data is 2 s based on the washout time of “cleaning shots” fired before the beginning of each analysis. The corresponding spatial resolution of the data is ~ 250 nm.

Isotope ratio data were corrected for down-hole fractionation, mass bias, and machine drift using Iolite (Paton, Hellstrom, Paul, Woodhead, & Hergt, 2011) version 2.5. Three reference materials were measured to assess accuracy and precision: Bear Lake Ridge titanite (“BLR”: Aleinikoff et al., 2007), MKED1 titanite (Spandler et al., 2016), and Y1710C5 (Spencer et al., 2013). Using BLR as the primary reference material, the average dates for all of the data in 16 MKED1 depth profiles are 1534 ± 2 Ma [2 standard error] ($^{206}\text{Pb}/^{238}\text{U}$), 1560 ± 2 Ma ($^{207}\text{Pb}/^{206}\text{Pb}$), and 1530 ± 2 Ma (“ ^{207}Pb -corrected” $^{206}\text{Pb}/^{238}\text{U}$ date assuming a common Pb composition of Stacey and Kramers, 1975); the expected age of MKED1 is 1519 Ma (Spandler et al., 2016), 1.0% and 0.7% younger than the $^{206}\text{Pb}/^{238}\text{U}$ and the “ ^{207}Pb -corrected” depth profile ages, respectively. A regression of all data from all four depth profiles of Y1710C5 returns a intercept date of 402 ± 1 Ma [2 standard error] (MSWD = 0.85), 3.3% older than the TIMS age reported by Spencer et al. (2013), but in agreement with the LA-ICP-MS depth profiles of Stearns et al. (2016) and within 1.5% of the LA-ICP-MS spot age reported by Garber et al. (2017). Based on the reproducibility between BLR and MKED1 and the similarity in LA-ICP-MS dates for Y1710C5 in this study, Stearns et al. (2016), and Garber et al. (2017), the suggestion of Spencer et al. (2013) that LA-ICP-MS U–Pb titanite dates have an accuracy of 2% seems appropriate for the depth profiles in this study. The precision of each isotope-ratio datum in each profile—estimated as the amount of uncertainty per datum required such that all data from the MKED1 and BLR profiles fit a single population by the MSWD criterion (Wendt & Carl, 1991)—is 5.1% (2σ) for $^{207}\text{Pb}/^{235}\text{U}$, 4.3% for $^{206}\text{Pb}/^{238}\text{U}$, 2.0% for $^{207}\text{Pb}/^{206}\text{Pb}$, and 7.5% for $^{208}\text{Pb}/^{232}\text{Th}$. Y1710C5 was not used in this assessment of precision, because it is not isotopically homogeneous (Spencer et al., 2013).

Zr-concentration depth profiles were calculated using the trace-element data reduction scheme of Iolite assuming an internal standard of Ca that was adjusted iteratively (near the stoichiometric value for CaTiSiO_5) until the average Zr concentration of MKED1 agreed with the value reported by Spandler et al. (236 ppm: 2016). MKED1 was chosen as the primary reference material for Zr concentrations, because BLR is compositionally heterogeneous (Stearns et al., 2016). The precision of each LA-ICP-MS Zr datum—estimated as the amount of uncertainty per datum required such that all of the MKED1 and BLR profile data fit a single population by the MSWD criterion (Wendt and Carl, 1991)—is 7.7%.

U, Th, and Pb were measured on the Nu Plasma MC-ICP-MS and therefore do not have the benefit of co-measured Ca to use as an internal standard. U and Th counts per second (cps) were background corrected using Iolite and then exported to Excel® for down-hole and standard corrections, which were made analogously to the Iolite “U/Th–Pb Geochronology” procedure. The down-hole correction was made by fitting reference-material (BLR and MKED1) cps vs. time with a cubic polynomial; the best-fit polynomial was used to correct the data of all profiles (reference materials and unknowns) such that there was no time-dependent signal intensity for the reference materials. The down-hole-corrected cps were then multiplied by a factor to match the expected ppm of the reference material MKED1; the same factor was applied to each unknown and each profile of the reference material BLR. U and Th concentrations were standard-corrected to MKED1, because it is more homogeneous than BLR. The precision of each LA-ICP-MS U and Th datum—estimated as the amount of uncertainty per datum required such that the data from each MKED1 profile define a single population by the MSWD criterion (Wendt and Carl, 1991)—is 6% (2σ).

The concentrations of individual Pb isotopes were processed two ways. *Method 1*) The first method is analogous to the processing of U and Th described above, except that the concentrations of the individual Pb isotopes in the reference materials need to be calculated before the final standard correction can be applied (e.g. ^{206}Pb cps to ^{206}Pb ppm rather than just using a Pb_{total} value). The Pb isotope concentrations for BLR and MKED1 were calculated by solving a system of linear equations constructed from the $^{208}\text{Pb}/^{206}\text{Pb}$, $^{207}\text{Pb}/^{206}\text{Pb}$, $^{206}\text{Pb}/^{204}\text{Pb}$, and total Pb ppm reported for these materials (Aleinikoff 2007; Spandler et al., 2013). The precision of the $^{206,207,208}\text{Pb}$ isotope concentrations determined by this method is 6% (2σ). ^{204}Pb concentration profiles are not reported; although the average \pm standard-error ^{204}Pb signal of each depth profile is above the detection limit, the precision of individual data points in the profiles are not, and therefore a statistically meaningful concentration-vs-depth gradient could not be extracted. *Method 2*) Pb isotope concentrations internally consistent with the isotope ratios and the U-Th concentrations were calculated by multiplying the Pb/U-Th isotope ratios by the U-Th concentrations ($^{207}\text{Pb}/^{235}\text{U} \times ^{235}\text{U}$ mol.; $^{206}\text{Pb}/^{238}\text{U} \times \text{U}$ mol.; $^{208}\text{Pb}/^{232}\text{Th} \times ^{232}\text{Th}$ mol.). Method 1 is an independent measure of Pb isotope concentrations, whereas Method 2 depends on the accuracy of the U and Th concentrations and the U/Th–Pb isotope ratios. The shape of the Pb-isotope concentration profiles calculated from *Method 1* and *Method 2* are identical, although Pb isotope concentrations are 20–40% higher using *Method 2*. Although the inhomogeneity of the BLR reference material limits the assessment of elemental-concentration accuracies by LA-ICP-MS (Stearns et al., 2016), the diffusivity estimates of Pb from LA-ICP-MS data in this study are based on U–Pb ratios and dates, which, as discussed above, have a precision of 2–5% and an accuracy of 2%.

4.3: Quantified EPMA trace-element maps

The elemental concentrations of Al, Fe, Zr, Nb, and Ce were mapped parallel to the LA-ICP-MS depth profiles in titanite 12D (after cutting the grain perpendicular to the profiled crystal face; Figure 5) and in a single large titanite grain in thin section (titanite 21B; Figure 6) by EPMA. The maps of titanite 21B were collected at a resolution of 10 μm and the maps collected parallel to the depth profiles in titanite 12D at a resolution of 1 μm . The beam current was 200 nA, and the accelerating voltage was 15 kV. LPET crystals were used to measure Zr and Nb L_{α} X-rays, LLIF crystals for Fe K_{α} and Ce L_{α} , and a TAP crystal was used for Al K_{α} . The maps were processed using Calc Image of the Probe for EPMA software. The weight percents of each element were calculated from the counts-per-second per nA of each pixel in the maps using a mean-atomic-number background calibration (Donovan, Singer, & Armstrong, 2016) and ZAF correction assuming that the matrix composition was CaTiSiO_5 . Some components not considered (chiefly F, which can comprise several wt.% of titanite) might have a small influence on the accuracy of the data reported herein, but the large uncertainties associated with the low-concentration, short-dwell-time data (e.g. ~6–20% 2SE for the swath profiles shown in Figure 7) are much larger than the uncertainties related to small changes in assumed matrix composition.

4.4: Estimating elemental diffusivities based on the characteristic length-scale of

diffusion: $u = 2(Dt)^{1/2}$

LASS depth profiles of sample 12D (Figure 3) show increases *and* decreases in U, Th, and individual Pb isotopes over the depth of the measurements. The ^{206}Pb and ^{207}Pb profiles

mimic the shape of the U profile, as expected for a system that has remained largely closed since 500 Ma. The ^{208}Pb profile also mimics the shape of the Th profile. The complexity of the concentration profiles prohibits fitting the profiles with simple analytical expressions for diffusion, such as the various error-function expressions used in the experiments of Cherniak (1993, 1995, 2006, 2015) and in the depth profiles of Stearns et al. (2016). Due to this limitation, D is simply estimated from the expression for the characteristic length scale of one-dimensional diffusion ($u = 2[Dt]^{1/2}$: u the diffusion length scale, D diffusivity, and t time at peak temperature). The same approach is applied to the length-scale of intra-titanite U–Pb date variability in the LA-ICP-MS map of titanite 21B, and in the EPMA depth profiles measured parallel to the LA-ICP-MS depth profiles of titanite 12D. In both of these cases, chemical potential is assumed to be proportional to concentration for the reasons described in section 4.3. Diffusivities calculated by this method are shown in Table S3.

4.5: Estimates of elemental diffusivity from relaxation of compositional steps

In titanite 21B, three steep compositional gradients were chosen to calculate elemental diffusivities (locations marked with stars in Figure 6). Compositional gradients were extracted from the EPMA maps as swath profiles (rather than individual line profiles) using the “swath profile” plugin for QGIS. A swath profile is the average parallel line profile within a specified area. The swath profiles are shown in Figure 7 and Table S4. Assuming that these compositional gradients began as step functions and that the rocks cooled linearly from the time the step functions formed, diffusion parameters for Al, Fe, Zr, Nb, and Ce were calculated using the following equation from Watson and Cherniak (2015):

$$\log S_0 = 2.504 - \frac{1}{2} \log D_0 - \log T_i + \frac{1}{2} \log E_a + \frac{1}{2} \log \dot{T} + \left(26.11 \frac{E_a}{T_i} \right)$$

where S_0 is the slope at the center of the best-fit error function (normalized such that the maximum value of the error function is 100 and the minimum is value 0); T_i the temperature (K) at which the compositional step formed and cooling began; \dot{T} the cooling rate (K/s); and D_0 (m²/s) and E_a (kJ/mol) are the elemental diffusivity at infinite temperature and the activation energy of diffusion, respectively. D_0 and E_a describe the temperature dependence of elemental diffusivity D by the Arrhenius relationship, $D = D_0 e^{-E_a/RT}$ (R , the gas constant). The cooling rate used for the calculations was 17 ± 7 K/Myr (Chapter 1). The starting temperatures used for the calculations are described in the following section. Because there are two unknowns, D_0 and E_a , the value of each can only be described as a function of the other. It was found that permissible values of D_0 and E_a are related by $\log_{10}(D_0) = m * E_a + b$. Uncertainties in S_0 (as a function of analytical uncertainties in the swath profiles), T_i (see following section), and \dot{T} (17 ± 7 K/Myr; Chapter 1) were propagated into uncertainties in m and b by Monte Carlo analysis. Implicit in these calculations is that the chemical potential of each element is proportional to its concentration; this is a reasonable assumption based on the low concentrations of each element (~2 wt.% Al; ~1.4 wt.% Fe; <1 wt.% each of Ce, Nb, and Zr) and their limited compositional ranges (± 1000 ppm Al and Fe, ± 500 ppm Ce, ± 200 – 400 ppm Nb, ± 3000 – 5000 ppm Zr). Results of the calculations are shown in Table S5.

4.5.1: Uncertainties in model starting temperatures

For each element in each profile, two calculations were made using the Zr-in-titanite temperatures from either side of the compositional steps as the starting temperature (T_i).

Uncertainties used for T_i are the propagated uncertainties of the coefficients of the experimental calibration of the Zr-in-titanite thermobarometer (Hayden et al., 2008), uncertainty in the pressure of metamorphism (0.6 ± 0.2 GPa; Chapter 1), and a conservatively large uncertainty in a_{TiO_2} (0.75 ± 0.25) reflecting the absence of rutile in the samples, but recognizing that a_{TiO_2} is likely greater than 0.5 in titanite-bearing rocks (Chambers & Kohn, 2012; Ghent & Stout, 1984). The highest starting temperature was $956 \pm 64^\circ\text{C}$, the lowest $873 \pm 57^\circ\text{C}$. The large uncertainties in T_i contribute to large uncertainties in the estimates of elemental diffusivities (± 1 to 2 orders of magnitude), but ensure that the results are not strongly biased toward a single interpretation of the terrane's thermal history. Uncertainties in the Zr-in-titanite temperature as a function of titanite REE and Al concentration are negligible by comparison (Hayden et al., 2008). As mentioned in the previous section, all uncertainties were propagated through the calculations by Monte Carlo analysis. The model starting temperatures are shown with the results of the calculations in Table S5.

5: RESULTS

A graphical summary of all elemental diffusivity estimates from this study is shown in Figure 10 alongside experimental data and relevant empirical constraints. This section discusses the length scales of compositional variation observed in titanite and the elemental diffusivities calculated from those length scales.

5.1: 800°C titanite 12D

Four U/Th–Pb+Zr LA-ICP-MS depth profiles were measured by drilling into the crystal face of titanite 12D (Figures 3, 4; Table S1); afterward, the titanite was cut perpendicular to that crystal face, polished until two of the LA-ICP-MS pits were partially exposed, and mapped by EPMA for Al, Fe, Zr, Nb, and Ce (Figure 5). Compositional gradients were extracted as swath profiles from the area between the two exposed laser pits in the EPMA maps (Table S2).

5.1.1: Estimates of Pb diffusivity from the LA-ICP-MS depth profiles of titanite 12D

LA-ICP-MS depth profiles (Figures 3, 4) of titanite 12D show downhole increases *and* decreases in U, Th, and individual Pb isotopes within the same pit. The ^{206}Pb and ^{207}Pb profiles mimic the shape of the U profile and the ^{208}Pb profile mimics the shape of the Th profile, as expected for a system that has remained largely closed since 500 Ma. However, the $^{206}\text{Pb}/^{238}\text{U}$, $^{207}\text{Pb}/^{235}\text{U}$, $^{208}\text{Pb}/^{232}\text{Th}$, and ^{207}Pb -corrected $^{206}\text{Pb}/^{238}\text{U}$ date (corrected using the $^{207}\text{Pb}/^{206}\text{Pb}$ composition of clinopyroxene from the same rock) profiles decrease toward the grain rim, corresponding to younger dates. The dates decrease gradually from 550 to 535 ± 11 Ma between the bottom of the pit and $\sim 6 \mu\text{m}$ depth, then decrease more rapidly to 495 ± 11 Ma at the crystal face. The decrease in U–Pb date toward the crystal face, particularly within the outermost 5–6 μm could reflect (1) protracted growth, as suggested by Stearns et al. (2016) for near-rim zoning in titanite from gneiss domes in the Pamir Mountains or (2) loss of Pb by Fickian diffusion.

Do the U–Pb profiles reflect protracted growth? To test the hypothesis of protracted growth, an apparent temperature–time history was calculated from a linear regression of the

Zr-in-titanite temperatures and the ^{207}Pb -corrected $^{206}\text{Pb}/^{238}\text{U}$ dates in the profile (Stearns et al., 2016). The resulting rate, 0.12 ± 0.04 K/Myr, is unreasonably slow, because it requires the Ikalamavony domain (where the sample was collected) to have remained at $\sim 800^\circ\text{C}$ until 500 Ma while the adjacent Antananarivo and Anosy domains cooled to $< 500^\circ\text{C}$ (Grégoire et al., 2009; Montel et al., 2018). The younging of the U–Pb dates near the titanite rim are therefore not interpreted to reflect simple, protracted growth.

Does the decrease in U–Pb date within the outermost 5–6 μm reflect loss of Pb by Fickian diffusion? The rim date (495 ± 11 Ma) agrees with a $^{40}\text{Ar}/^{39}\text{Ar}$ amphibole plateau date of 511 ± 10 Ma obtained from a sample collected ~ 30 km east of this titanite (Grégoire et al., 2009). The difference between the titanite dates from > 6 μm depth in the profiles and the amphibole date correspond to a reasonable terrane-scale cooling rate of 5–10 K/Myr from $\sim 800^\circ\text{C}$ (Zr-in-titanite temperature) to $\sim 500^\circ\text{C}$ ($^{40}\text{Ar}/^{39}\text{Ar}$ amphibole date). If the near-rim gradient is interpreted to be the result of Fickian Pb diffusion (assuming U diffuses significantly more slowly than Pb), the 5 μm characteristic length scale and the 30–40 Myr timescale of near-peak metamorphism (accounting for the range of dates in the proposed Pb diffusion profile) corresponds to a Pb diffusivity of $\sim 10^{-26.2}$ m^2/s near the peak temperature of 750 – 800°C (Zr-in-titanite thermometry of this study and pseudosections of GAF-BGR, 2008; Table S3). This estimate for Pb diffusivity is ~ 1 order of magnitude slower than extrapolated estimates of Sr diffusivity in experiments (Cherniak, 1995; suggested to be a reasonable proxy for Pb diffusivity by Kohn, 2017; Figure 10). If the proposed Pb loss were instead the result of a short (~ 1 Myr) thermal pulse at ~ 500 Ma, the estimate for Pb diffusivity is comparable to Sr diffusivity in experiments, but still significantly slower than Pb diffusion experiments (Cherniak, 1993).

5.1.2: Estimates of Al, Fe, Zr, Nb, and Ce diffusivities from EPMA depth profiles of titanite 12D

The EPMA maps and extracted swath profiles of Al, Fe, Zr, Nb, and Ce are shown in Figure 5. Zr, Al, and Fe all decrease monotonically toward the crystal face of titanite 12D; no clear diffusion profiles are present. Based on a conservative range of durations of near-peak metamorphism (1–40 Myr; accounting for the range of U–Pb dates in the LA-ICP-MS depth profiles) and the μm scale resolution of the EPMA data, the diffusivities for these elements at 750–800°C are $\leq 10^{-26.1}–10^{-27.7} \text{ m}^2/\text{s}$ (Figure 10; Table S3). The Nb concentrations increase toward the crystal face within the outermost 6 μm of the profile. If this is the result of diffusive influx, rather than growth, this corresponds to a diffusivity of $10^{-24.5}–10^{-26.2} \text{ m}^2/\text{s}$ (Figure 10; Table S3). Ce increases gradually toward the crystal face within the outermost 20 μm of the profile. If this is the result of diffusive influx, rather than growth, this corresponds to a diffusivity of $10^{-23.5}–10^{-25.1} \text{ m}^2/\text{s}$ (Figure 10; Table S3). However, the absence of Zr, Al, or Fe diffusion profiles suggests that the Ce and Nb profiles might simply reflect growth zoning and the estimated diffusivities should be considered maxima.

5.2: 900–1000°C titanite 21B

EPMA maps of Al, Fe, Zr, Nb, and Ce in titanite 21B are shown in Figure 6. The compositional steps used for diffusion modeling are indicated with stars in Figure 6a and shown in more detail in Figure 6b. The best-fit profiles for each element in each compositional gradient are shown in Figure 7. The normalized compositional gradients of each element in each compositional profile are shown in Figure 8 along with predicted compositional gradients using experimental diffusion parameters. The LA-ICP-MS map of

titanite 21B is shown in Figure 6a and in more detail in Figure 9. The estimates for elemental diffusion from titanite 21B are compared to those from titanite 12D and previous studies in Figure 10.

5.2.1: Estimates of Al, Fe, Zr, Nb, and Ce diffusivities from relaxed compositional steps

Swath profiles with best-fit error functions are shown in Figures 7 and 8. Calculated diffusion parameters are shown in Table S5. Diffusivities, calculated for $E_a = 300$ and 500 kJ (the range of cation E_a reported experimentally), are shown in Figure 10. The apparent length scales of the compositional gradients in Zr, Al, and Nb are ~ 40 μm . The apparent length scales of the compositional gradients in Ce range from 40 – 80 μm . The apparent length scales of compositional gradients in Fe are 100 – 200 μm . The estimates of elemental diffusivity extracted from these profiles are maxima, because the modeled compositional boundaries are likely not perpendicular to the thin section, resulting in apparent length scales of diffusion greater than the true length scales. Diffusivities presented in the following paragraphs and shown in Figure 10 were calculated using a cooling rate of 17 ± 7 K/Myr (Chapter 1). If the cooling rate were an order of magnitude faster, calculated diffusion rates would likewise be an order of magnitude faster. Rates >1000 K/Myr are required by the models to reproduce the experimental diffusivities of Nb and Zr; these are not reasonable terrane-scale cooling rates.

The estimates for maximum Zr diffusivity in this study are 4 ± 1 orders of magnitude slower than the experimental results of Cherniak (2006), in agreement with the assessment of Walters and Kohn (2017). The estimates for maximum Nb diffusivity are 3 ± 2 orders of magnitude slower than experiments (Cherniak, 2015). The estimates for maximum Al

diffusivity are 1 to 2 ± 1 orders of magnitude slower than experimental Nd diffusivity measured at FMQ (Cherniak, 1995) and 3 to 4 ± 1 orders of magnitude slower than experimental Nb–Ta diffusivity (Cherniak, 2015); in those experiments, Al was diffusively coupled to those elements. The large differences in Nb and Al molar concentrations (Figure 7) indicate that the elements did not diffuse solely as a charge-coupled pair ($\text{Nb}^{5+} + \text{Al}^{3+} = 2\text{Ti}^{4+}$), as was also noted by Cherniak (2015). Surprisingly, the diffusivities of Nb and Al—which rely on coupled substitutions—are the same as those of Zr, within uncertainty, which is thought to enter titanite by the simple substitution mechanism $\text{Zr}^{4+} = \text{Ti}^{4+}$ (Hayden et al., 2008).

The estimates for maximum Ce diffusivity are the same as, or within 1 order of magnitude of, experimental Nd diffusivity measured at the FMQ buffer (Cherniak, 1995). This agreement is consistent with the predicted similarities in geochemical behavior of the REE, but significant in that Ce has two common valence states (Ce^{4+} and Ce^{3+}) that likely diffuse by different mechanisms and at different rates. Due to differences in Ce valence, Ce diffusivity is likely to be influenced by $f\text{O}_2$.

Fe exhibits the largest and most variable length scales of compositional variation. Fe is commonly assumed to substitute into titanite by the same mechanism as Al— $(\text{Al}, \text{Fe}^{3+}) + (\text{F}^-, \text{OH}^-) = \text{Ti}^{4+} + \text{O}^{2-}$ —and therefore might be expected to have an elemental diffusivity similar to Al. However, in all profiles, the Fe gradients are $>3x$ longer than the Al gradients, indicating that Fe diffusivity was at least $9x$ greater than Al diffusivity ($u = 2[\text{Dt}]^{1/2}$). This may be explained, in part, by the presence of at least some Fe^{2+} in titanite, rather than just Fe^{3+} as is commonly assumed: Fe^{2+} would likely diffuse faster than Fe^{3+} due to its lower charge. If titanite accommodates Fe^{2+} and Fe^{3+} , the diffusivity of elemental Fe is likely to be

influenced by fO_2 . The estimates of maximum Fe diffusivity agree with experimental diffusivities of other cations (Sr, Nd, Nb, Ta).

5.2.2: Estimates of Pb diffusivity from the LA-ICP-MS map of titanite 21B

The LA-ICP-MS map of titanite 21B (Figure 9) shows U–Pb dates from 550 Ma to 490 ± 11 Ma (spot analyses corrected for common Pb using the $^{207}\text{Pb}/^{206}\text{Pb}$ composition of clinopyroxene). The oldest dates agree with the age of peak metamorphism in the Anosyen Domain (550 ± 11 Ma) that lasted <20 Myr (Chapter 1). These isotopically older domains within the titanite have radii of 200–300 μm . For a length scale of 200–300 μm , a peak temperature of 900–1000°C (Jöns and Schenk, 2011; Boger et al., 2012; Horton et al., 2016; Chapter 1), and a timespan of 1–20 Myr for peak metamorphism, the estimated Pb diffusivity is $10^{-20.5}$ – $10^{-21.9}$ m^2/s . This value is equivalent to estimates of Sr diffusivity from the experiments of Cherniak (1995), and consistent with the hypothesis of Kohn (2017) that experiments for Sr diffusivity are a good fit to empirical estimates of Pb diffusivity.

Although the length scale of Pb diffusion *within* Madagascar titanite is consistent with experimental estimates for Sr diffusivity, the distribution of U–Pb dates within the grain suggest that diffusion of Pb out of titanite might not have occurred at the same rate everywhere. The titanite dates do not decrease from core to rim (Fig 5), but rather, two broad regions of older titanite dates are preserved. The oldest dates (550–540 Ma) are immediately adjacent to the grain rim. (All of these data have been screened using trace-element concentrations to remove the effects of small impurities: e.g., zircon or monazite.) The irregular distribution of U–Pb dates might indicate that diffusion of Pb out of titanite depends on grain-boundary conditions, such as the availability of a fluid phase, or which phase was

adjacent to titanite. The possible importance of grain-boundary conditions limiting (or facilitating) Pb loss from titanite 21B is supported by the observation that the youngest titanite dates are correlated with grain boundaries shared with calcite (Figure 9), which is interpreted to be a retrograde phase formed by the reaction wollastonite + CO₂ → calcite + quartz. However, this correlation is not absolute. Some grain boundaries shared with calcite preserve distinctly older titanite dates, whereas other grain boundaries shared with wollastonite preserve some of the youngest dates. Some of this complexity may be related to local growth or resorption of the titanite during cooling; the most irregular titanite grain boundaries are those shared with calcite and these grain boundaries are enriched in Fe, which is otherwise relatively homogeneous throughout the grain (Figure 6).

The importance of grain-boundary conditions on elemental diffusion out of minerals was previously suggested by Kohn et al. (2016), who measured LA-ICP-MS depth profiles in rutile from amphibolites on Catalina Island, USA. Kohn et al. found profiles of Nb, Zr, and U in rutile that differ in magnitude and direction (increasing vs decreasing toward grain rim) among grains within individual samples and are therefore unlikely to reflect diffusional equilibration with the rest of the rock during cooling. Kohn et al. suggested that slow grain-boundary diffusion of Zr (or Si, which is required for retrograde zircon growth, the primary sink for Zr leaving rutile) limited the ability of Zr in rutile to equilibrate with other minerals in the rock. In granulite-facies rocks, like those of this study, grain-boundary mobility is likely limited by the low a_{H₂O} of the grain-boundary fluid.

6: DISCUSSION

6.1: Differences among empirical and experimental diffusivity estimates in titanite: the possible role of coupled substitutions and solid-solution complexity

The purpose of this study is to provide empirical constraints on elemental diffusion in titanite. As with previous studies, the elemental diffusion rates of Pb and Zr were found to be slower than in experiments. Nb diffusion was also found to be slower than experiments. This section discusses chemical and physical differences between the titanite used in experiments and most natural titanite that might explain these differences in elemental diffusivities.

A notable difference between the empirical and experimental studies of elemental mobility in titanite is that the experimental studies have used close to end-member CaTiSiO_5 —as evident from its pale green color, minimal Al–Fe content, and near 100 wt.% totals for EPMA measurements of major elements—whereas most titanite used for geochronology is brown–orange–red and has a wider range in composition. For example, titanite reported in Garber et al. (2017), which might be considered typical for granitic rocks, has 2–3x higher Al–Fe than titanite used in experiments, 0.5–2 wt.% F, and EPMA totals of ~95 wt.%, indicating that the sum of minor and trace elements not measured by EPMA are a significant component of the titanite solid solution. This is corroborated by Garber’s et al. LA-ICP-MS trace-element oxide totals (calculated from their Table S1), which range from 0.2 to 7.1 wt.% with a median of 1.3 wt.%. The sum of elemental Al, Fe, Zr, Nb, and Ce alone in titanite 21B in this study (from the quantified EPMA maps) is ~5 wt.%. These points emphasize that natural titanite grains may have more complex solid solutions than the titanite used in experimental diffusion studies. Most of these minor and trace elements are

accommodated in titanite by multiple coupled substitutions unlikely to have operated in experiments with purer titanite.

The possible importance of coupled vs uncoupled diffusion in titanite, as well as the complexity of individual diffusion mechanisms is illustrated in part by the experiments of Cherniak (1995) on Sr and Nd diffusion. Cherniak found that Nd diffusion in air was ~1 order of magnitude faster than Nd diffusion buffered at FMQ. The activation energies of diffusion were lower in air than at FMQ, indicating that the diffusion mechanism was different. Neodymium diffusion was coupled to Al diffusion (one-to-one) in experiments conducted at FMQ, but showed no coupling to Al (and Al showed no diffusion profile) in experiments conducted in air. The coupling to Al at FMQ can be explained by the reaction $\text{Nd}^{3+} + \text{Al}^{3+} \leftrightarrow \text{Ca}^{2+} + \text{Ti}^{4+}$, but the mechanism for the apparently uncoupled diffusion in air is unclear. Cherniak suggested that it might be related to the presence of defects (a faster diffusion pathway) created by the oxidation of Fe (the samples changed from green to red when annealed in air prior to experiments), or by coupled substitution with anions on the volatile site (O, OH, F, Cl), although she did not find appreciable differences in O or F contents among untreated, annealed-in-air, or annealed-at-FMQ samples. The apparently uncoupled Nd diffusion in air (faster than at FMQ) was found to have the same rate as Sr diffusion, which was also interpreted to be uncoupled ($\text{Sr}^{2+} \leftrightarrow \text{Ca}^{2+}$) and did not have different diffusion rates at different $f\text{O}_2$. These experiments show that order-of-magnitude differences in elemental diffusivities (of Nd and Al) can result from differences in how elements are coupled in the crystal lattice and, possibly, differences in ambient conditions (in this case, $f\text{O}_2$).

In experiments on Nb and Ta diffusivity (Cherniak, 2015), the length-scales of Nb and Ta diffusion were found to be identical to the length scales of Al diffusion, although the molar proportions of Al were not sufficient to charge balance the amount of Nb-Ta present, suggesting that other elements (Fe^{3+} , Na^+ , F^-) must have been involved. Even in the relatively simple titanite used in experiments, diffusion of a single element may require exchange of other elements in the crystal lattice. The correlations between Al and Nd-Nb-Ta diffusion suggest that trace-element diffusivities and Al (and Fe^{3+}) diffusivity are fundamentally linked, such that movement of any of these elements will be partially limited by the mobility of other elements. This interpretation is supported by the similarities among calculated diffusivities for Al, Nb, and Ce (a REE, like Nd) in this study.

The complexity of cation substitution in titanite is also highlighted by Prowatke and Klemme's (2005) experimental study of trace-element partitioning between titanite and silicate melt. Prowatke and Klemme found that total REE-Nb-Ta partitioning into titanite was correlated with titanite Al content, but that Al content was independent of REE-Nb-Ta content. The correlation between Al and total REE-Nb-Ta concentrations was nonlinear. They concluded that titanite–melt trace-element partitioning was affected more by trace-element coordination in the melt than by changes in crystal structure caused by changes in titanite composition. More importantly for this discussion, Prowatke and Klemme concluded that the substitution of REE-Ta-Nb into titanite may have involved vacancies ($4\text{Nb}^{5+} + \square \leftrightarrow 5\text{Ti}^{4+}$, $2\text{REE}^{3+} + \square \leftrightarrow 3\text{Ca}^{2+}$), and not Al, although the aforementioned coupled substitutions involving Al may have been operating too.

Although Prowatke and Klemme concluded that total REE partitioning was not a function of Al content, they did recognize changes in the physical properties of the titanite crystal lattice as a function of Al content. With increasing titanite Al content, their REE profiles exhibited more-pronounced MREE enrichment (higher Gd relative to La and Lu). Lattice strain modeling of REE substitution into the Ca site suggested an increase in the apparent Young's modulus of the Ca site by a factor of 2.3 for an increase in Al₂O₃ of 0.13 to 0.69 wt.%. Garber et al. (2017) noted the same correlation between REE concavity and Al content in the Western Gneiss region, Norway. Garber et al. interpreted this to reflect decreases in the Ca–O and [Ti,Al]–O bond lengths and unit-cell volume as a function of Al ↔ Ti substitution (Oberti, Smith, Rossi, & Caucia, 1991).

To summarize, most natural titanite is a more complex solid solution than titanite used in diffusion experiments. Non-CaTiSiO₅ substituents in titanite commonly comprise ≥5–10 wt.%. The substitution of Al in particular has been shown to correspond to changes in properties of the titanite lattice. Although speculative, changes in composition and crystal structure might correspond to at least small changes in elemental diffusivities, as has been shown for interdiffusion in metal alloys (Porter & Easterling, 1990) and predicted for O diffusion in silicates (Zheng & Fu, 1998). Most substituents enter the titanite lattice through multiple coupled substitution mechanisms, such that none of the substituents likely diffuse independently of the others. The rates of even relatively simple diffusion mechanisms, like Zr⁴⁺ ↔ Ti⁴⁺, might be limited by the extent to which each of these elements is coupled to other elements in the titanite lattice. The relatively slow empirical diffusion estimates might reflect fundamentally different diffusion mechanisms than those operating in experiments with simpler solid solutions.

6.2: The role of fluids in resetting titanite U–Pb dates and composition

It has long been recognized that the activities of fluid components (especially $f_{\text{H}_2\text{O}}$) and fluid speciation (such as H_2O , H^+ , OH^- , H_2 , CO_2 , and O_2) influence O diffusion rates (e.g., Elphick and Graham, 1988; Sharp et al., 1991; Kohn, 1999). Some studies have suggested that fluids may influence specific cation diffusivities in minerals (water has been shown to increase Al–Si order/disorder reaction rates [Yund and Tullis, 1980], but not Na–K diffusion rates [Lin and Yund, 1972] in feldspars), but well-documented relationships between fluid fugacities or speciation and cation diffusivities are lacking.

Although fluid presence/absence and fluid composition are not likely to play a significant role in Fickian diffusivity in titanite, they may be important for the formation of “fast-diffusion pathways” and in facilitating dissolution–precipitation reactions. For example, Garber et al. (2017) noted that titanite from the Western Gneiss region, Norway, commonly has multiple, discontinuous, lobate, chemical domains with sharp compositional boundaries suggestive of interface-coupled dissolution–precipitation reactions (IDR; Putnis, 2009). In addition to the textural observations, this interpretation was corroborated by (1) a higher F content of replacement titanite relative to the titanite cores, indicating changes in fluid composition between the time of original titanite growth and the formation of each of the lobate chemical domains, and (2) REE depletion in these domains and the growth of allanite along titanite grain boundaries, interpreted to be the sink for REE evacuated from titanite during IDR. Garber et al. suggested that the fluid responsible for IDR was “a hydrous, saline brine with elevated F abundance.” Similar zoning patterns are seen in the titanite of this study, as well as those of Franz and Spear (1985), Spencer et al. (2013), Bonamici et al.

(2015), and Walters and Kohn (2017). IDR appear to be a primary mechanism by which titanite U–Pb dates and composition are reset, although in some cases (such as titanite replacement of rutile; Lucassen et al., 2010; 2012) the commonly observed “patchy” zoning that results might reflect differences in elemental availability during titanite growth.

Although IDR can be qualitatively argued to be an important process, the composition of the reacting fluid might also be significant. Marsh and Smye (2017) documented two distinct near-rim alteration textures (interpreted to be different fluid-mediated reactions) in titanite from mafic granulites of the Grenville Province. One texture consisted of lobate subdomains defined by compositional steps and was most prominently seen adjacent to plagioclase that was interpreted to have crystallized from former silicate melt. The edges of the subdomains were identified by bright μm -scale bands in BSE images interpreted to be preserved IDR fronts. The second type of near-rim zoning was characterized by gradual increases in trace elements toward titanite rims resorbed during the formation of clinopyroxene–ilmenite symplectites, aforementioned sub-grain boundaries, and BSE-bright titanite overgrowths adjacent to amphibole. The association of these features with reaction textures along titanite grain boundaries led Marsh and Smye to speculate that these were regions of “enhanced elemental mobility potentially resulting from the development of local micro-porosity pathways at some point in the recrystallization processes.” The two types of near-rim zoning attributed to fluid interaction were spatially associated with different minerals (plagioclase/former melt and amphibole) suggesting that the rates and efficiencies of fluid-mediated replacement might depend on fluid composition. Changes in F–Cl contents of the fluid will change the stable major-element composition of titanite (e.g., Franz and Spear, 1985) as well as the solubilities of REE and high-field-strength elements (e.g., Migdisov et

al., 2009; Rapp et al., 2010; Williams-Jones et al., 2012). As mentioned above, Garber et al. (2017) have shown that titanite IDR textures correlate with changes in F–Cl and REE content in titanite.

7: CONCLUSIONS

Elemental diffusivities in titanite were estimated from the length scales of compositional and isotopic heterogeneity in granulite-facies titanite from southern Madagascar. The calculated Pb diffusivities are similar to the experimental data for Sr (Cherniak, 1995), but are several orders of magnitude slower than the experimental data for Pb (Cherniak, 1993). Titanite U–Pb dates can be preserved through temperatures as high as 850°C and should not be interpreted as cooling ages unless grain-scale evidence for Fickian diffusion can be documented. Al, Fe, Nb, Zr (Zr-in-titanite thermobarometry), and Ce diffuse more slowly than Pb and reflect the conditions of titanite crystallization in all but the highest grade rocks (>900°C). Fluid-mediated dissolution–precipitation reactions, titanite growth, and titanite recrystallization are more important than volume diffusion for resetting titanite dates and composition. Differences between the diffusivities estimated from natural titanite and those determined experimentally might be related to physical and chemical differences between most natural titanite and near-end-member CaTiSiO_5 titanite used in experiments.

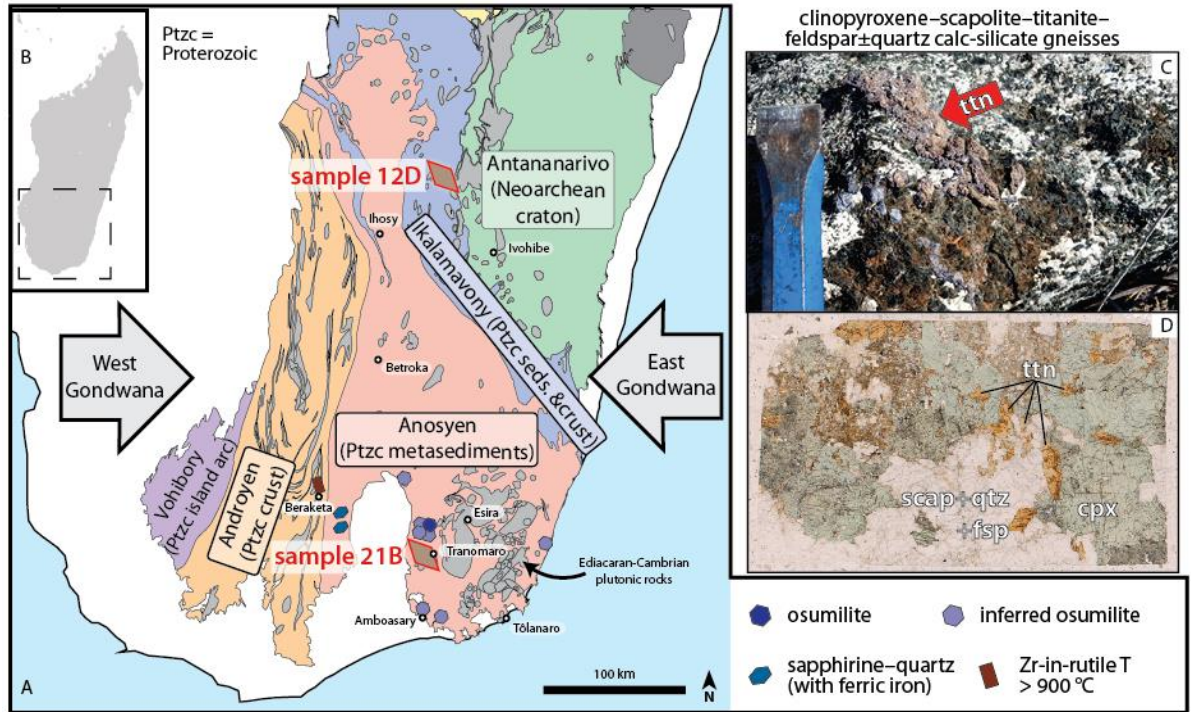


Figure 1. (A) Simplified geological map of the tectonometamorphic domains of southern Madagascar showing the locations of samples used in this study and other diagnostic high-temperature mineral assemblages (the assemblage spinel–quartz is also known throughout the Anosyen domain and Eastern Androyen domain). (B) Location of study area in Madagascar. (C) Photograph of a typical calc-silicate gneiss near Tranomaro with large titanite grains: 2 cm chisel for scale. (D) Thin section (2x4.5 cm) of typical calc-silicate gneiss.

titanite 12D

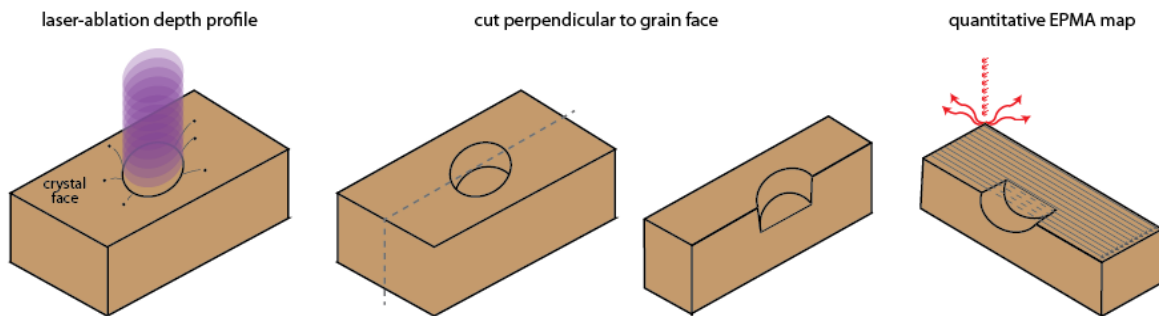


Figure 2. Near-rim compositional and isotopic zoning in titanite 12D was measured by LA-ICP-MS profiling of a crystal face followed by sectioning the grain perpendicular to the analyzed crystal face and mapping the sectioned plane by EPMA. Results of these analyses are shown in Figures 3–5. Elemental diffusivities calculated from near-rim zoning are shown in Figure 10.

titanite 12D

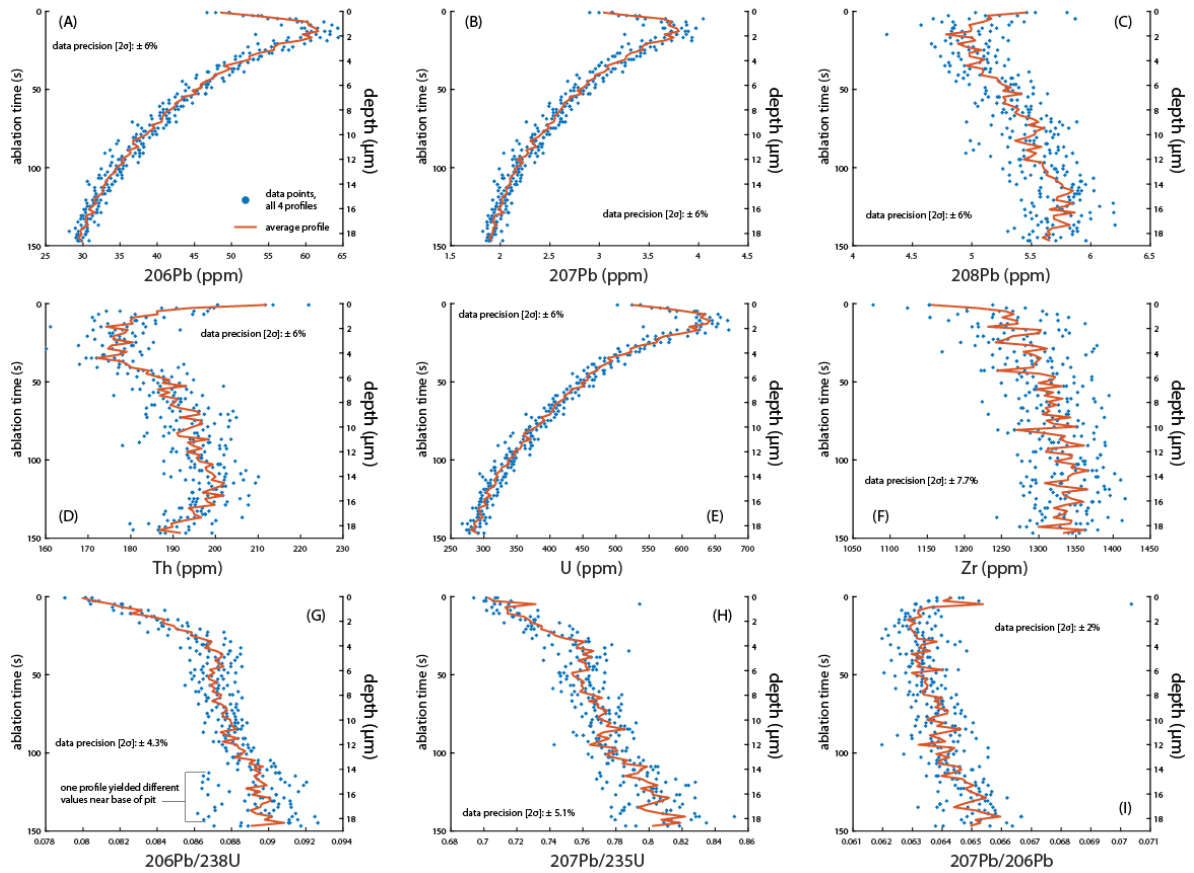


Figure 3. Near-rim concentration gradients of ^{206}Pb (A), ^{207}Pb (B), ^{208}Pb (C), Th (D), U (E), and Zr (F) as well as isotopic gradients of $^{206}\text{Pb}/^{238}\text{U}$ (G), $^{207}\text{Pb}/^{235}\text{U}$ (H), and $^{207}\text{Pb}/^{206}\text{Pb}$ (I) measured by LA-ICP-MS in titanite 12D. Points are the individual data from each of four depth profiles measured on the same crystal face. The line is the average of all four profiles. ^{206}Pb and ^{207}Pb profiles mimic U, as expected for a system that has remained closed since 500 Ma. ^{208}Pb also mimics Th. Decreases in Pb/U isotope ratios toward the grain rim could reflect protracted growth or diffusional Pb loss. Diffusional Pb loss is the favored interpretation for these data for reasons outlined in the text. See Figure 4 for the common-Pb corrected U–Pb date profile and corresponding concordia diagram.

titanite 12D

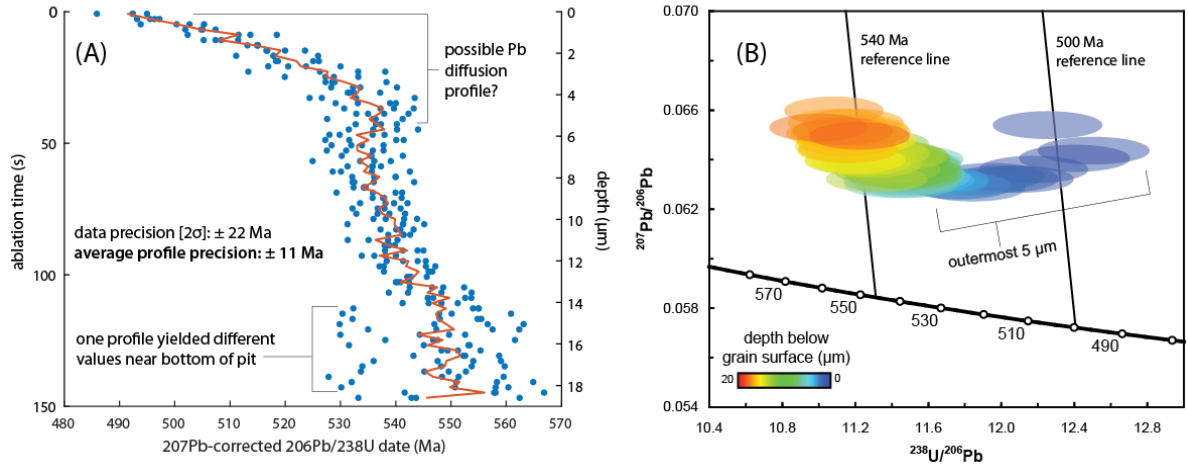


Figure 4. (A) Common-Pb-corrected $^{206}\text{Pb}/^{238}\text{U}$ date profile for LA-ICP-MS analyses of the crystal face of titanite 12D and (B) corresponding concordia diagram showing each datum of the averaged profile colored by depth from the crystal face. Data in (A) were corrected using the $^{207}\text{Pb}/^{206}\text{Pb}$ composition of clinopyroxene in the same rock. Reference lines in (B) point to this sample's common Pb composition. The abrupt decrease in U–Pb date in the outermost 5 μm is interpreted to reflect diffusion loss of Pb. Using 5 μm as the length-scale of Pb diffusion and the 30–40 Myr range of U–Pb dates preserved in proposed diffusion profile corresponds to an elemental Pb diffusivity ~ 1 order of magnitude slower than extrapolated values of Sr diffusivity in experiments. However, interpretation of this as a Pb diffusion profile is inconsistent with the results of Stearns et al. (2016), who found no evidence for Pb diffusion at the sub- μm scale in similar temperature rocks from the Pamir Mountains. See text for discussion.

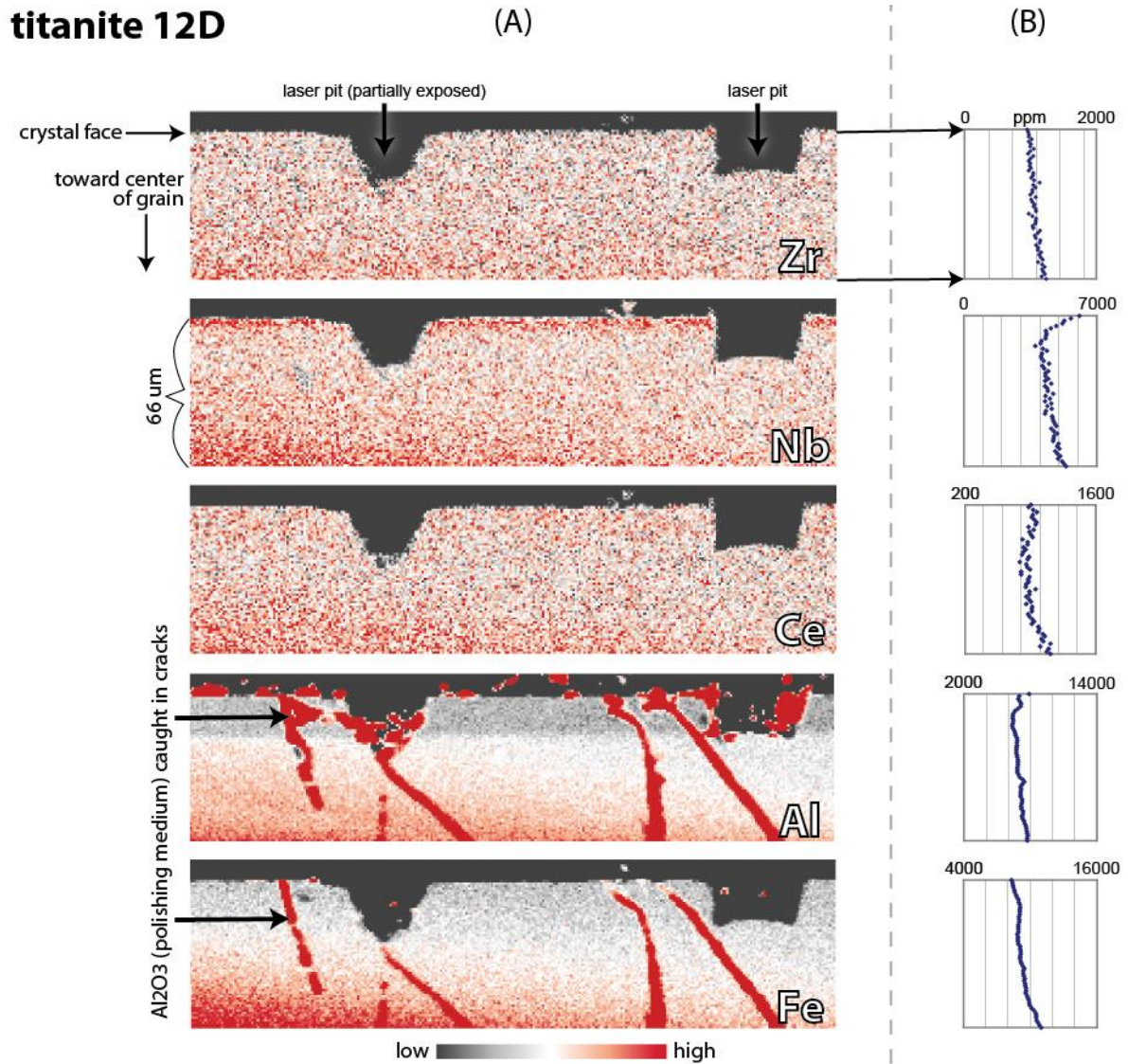


Figure 5. (A) Elemental concentration maps perpendicular to titanite 12D crystal face. Two of the four LA-ICP-MS depth-profiles are partially exposed. Irregularities in their shape are due to damage accrued during sectioning and polishing: qualitatively visible by the accumulation of polishing medium along fractures and the edges of the pits (Al and Fe maps). (B) Elemental concentration profiles extracted by swath transect of the area between the two LA-ICP-MS pits. Zr, Al, and Fe decrease monotonically toward the crystal face and show no evidence for near-rim diffusion. Possible diffusive influx of Nb and Ce are inferred from increases in their concentrations in the outermost 6 and 20 μm , respectively; however, the absence of any apparent diffusion profiles in Zr, Al, or Fe suggest this might be growth zoning, rather than diffusion. Maximum elemental diffusivities inferred from these possible lengthscales of elemental diffusion are shown in Figure 10.

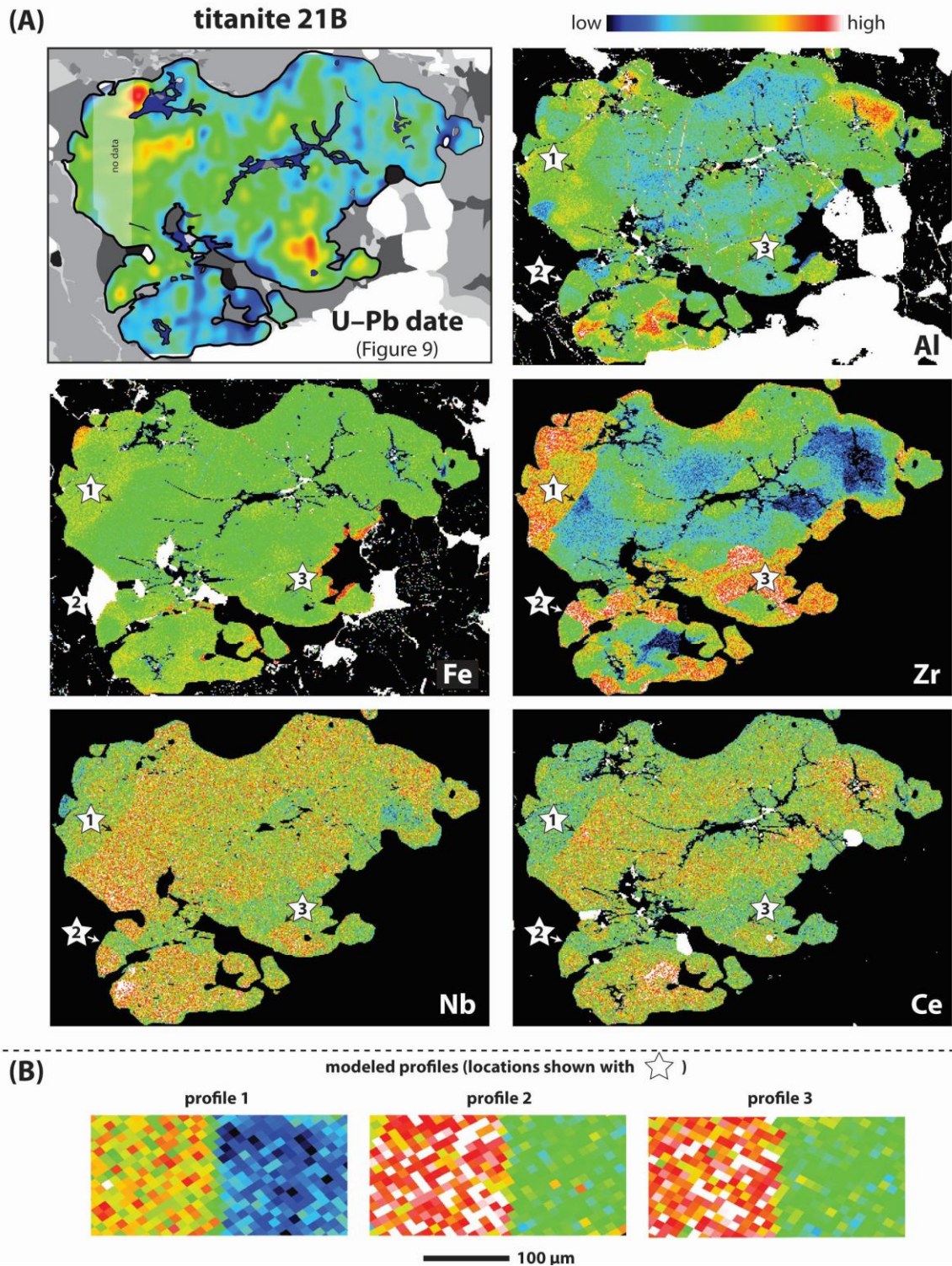


Figure 6. (A) LA-ICP-MS U-Pb map and EPMA Al, Fe, Zr, Nb, and Ce maps for titanite 21B. Steep compositional gradients in the EPMA maps, marked with stars, were modeled as diffusively relaxed step functions to estimate elemental diffusivities in titanite (Figures 7, 8, 10). LA-ICP-MS U-Pb map is shown in more detail in Figure 9. (B) Higher magnification images of steep compositional gradients in Zr used in diffusion modeling. Pixel size is 10 µm.

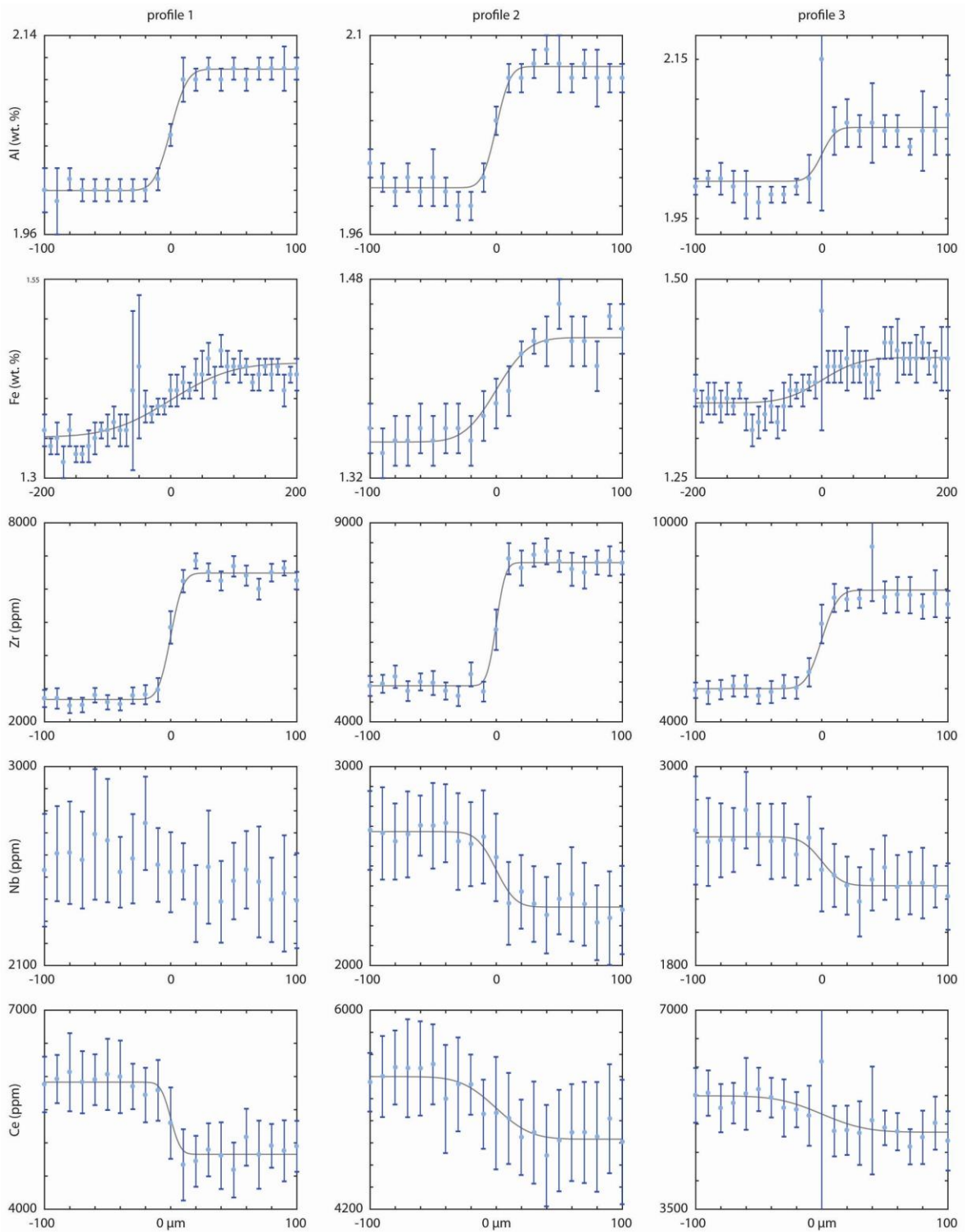


Figure 7. Swath profiles of each element in each transect from titanite 21B used to calculate elemental diffusivities along with best-fit error functions (grey lines). Blue error bars are means \pm 2SE for each swath profile sampled at 10 μm intervals perpendicular to the compositional steps shown in Figure 6. Calculated elemental diffusivities are shown in Figure 10.

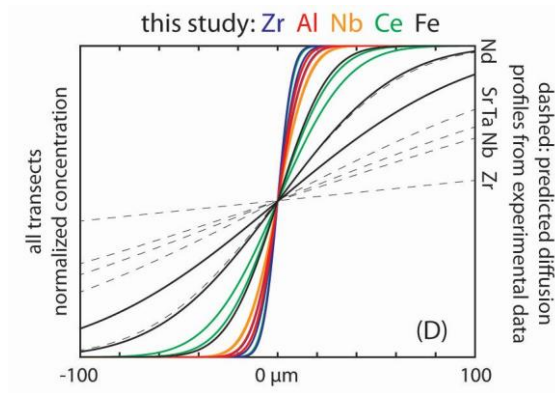
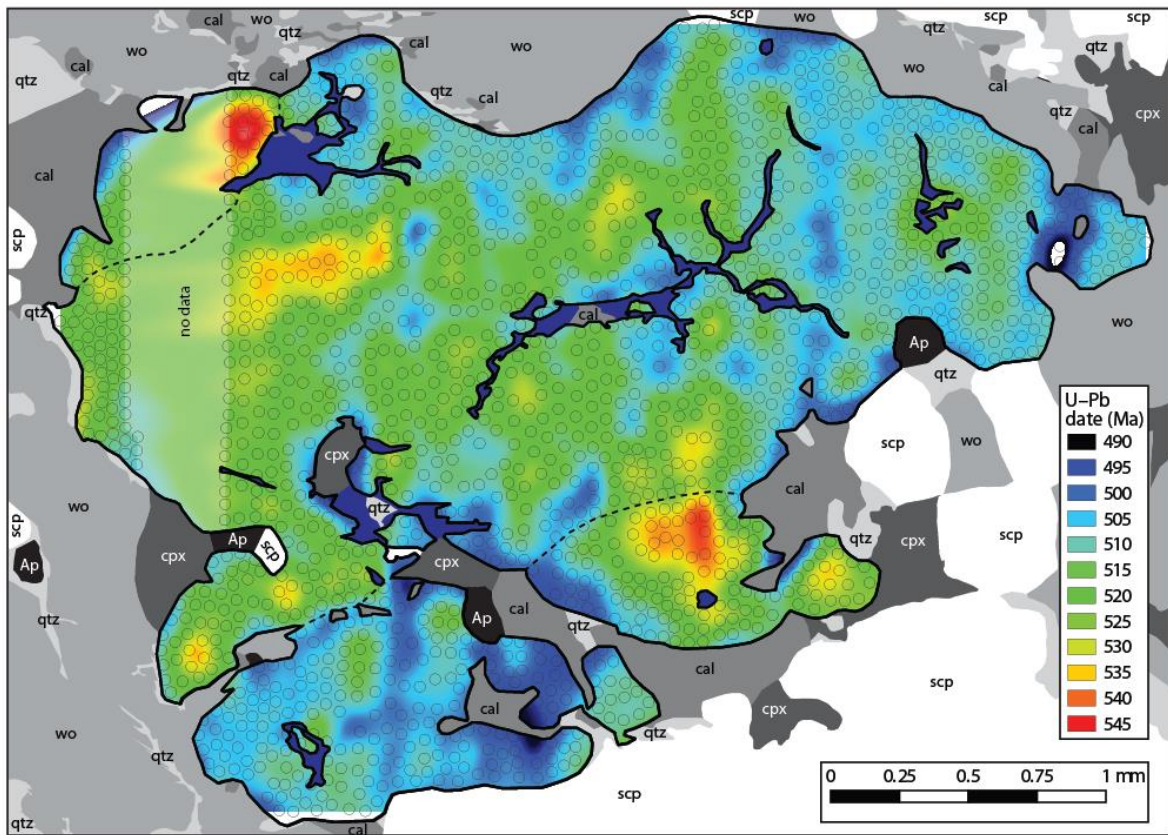


Figure 8. The length scales of elemental diffusion measured in this study are shorter than predicted by experiments. Colored lines are best-fit profiles from Figure 7. Dashed lines are the profiles predicted by experiments for a diffusively relaxed compositional step formed at 900°C and cooled at a rate of 10 K/Myr.

titanite 21B




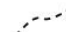

-  fractures in titanite with abundant inclusions of zircon (high Zr spots in Fig. 6 maps), allanite (high Fe–Al–Ce spots in Fig. 6 maps), and calcite (low Zr–Fe–Al–Ce–Nb in Fig. 6 maps)
-  subgrain boundaries (abrupt changes in extinction angle in cross-polarized light)
-  LA-ICP-MS spot analyses (40 μm diameter)

Figure 9. Map of LA-ICP-MS U–Pb dates in titanite 21B with nearby minerals indicated using the symbology of Kretz (1983). Dates are $^{206}\text{Pb}/^{238}\text{U}$ dates corrected for common Pb using the $^{207}\text{Pb}/^{206}\text{Pb}$ composition of nearby clinopyroxene. Dates correspond to the timing of peak metamorphism (550 Ma) and subsequent cooling, but do not define simple core–rim decrease as might be predicted for Pb loss by volume diffusion. Rather, old dates are preserved in two distinct regions near the grain boundaries. The radii of these isotopically old domains are consistent with the length scales predicted for Sr diffusion in experiments, suggesting that experimental Sr diffusion might reasonably approximate Pb diffusion in natural titanite. However, U–Pb dates along the titanite grain boundary differ by as much as 50 Ma, indicating that either (1) grain boundary conditions locally limited Pb diffusion out of titanite or (2) the grain experienced local resorption and growth in addition to Pb diffusion during cooling. See text for further discussion.

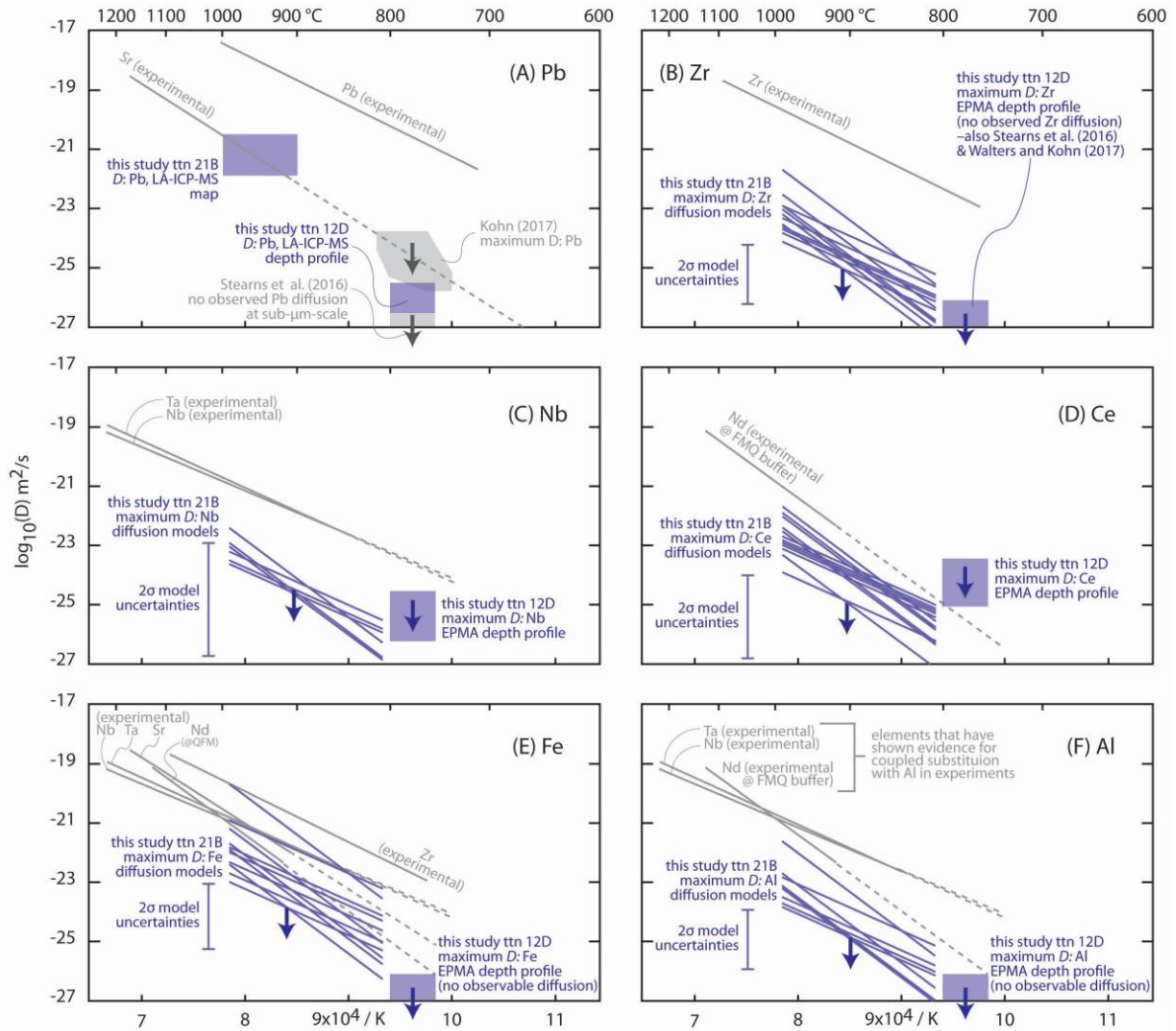


Figure 10. Diffusivity estimates from this study compared to experimental data. (A) Titanite Pb diffusion in rocks is predicted to be similar to or slower than Sr diffusion in experiments. For rocks that reached peak temperatures $\leq 850^{\circ}\text{C}$, titanite U–Pb dates likely reflect the timing of titanite (re)crystallization, not a cooling age. (B–F) Other cations diffuse more slowly than Pb; their compositions should reflect conditions of (re)crystallization in all but the smallest grain sizes in the highest grade rocks. Purple boxes show calculated elemental diffusivities based on the characteristic length scale of diffusion. Blue lines show calculated elemental diffusivities from relaxed compositional steps (assuming $E_a = 300$ and 500 kJ/mol). Experimental diffusivities are from Cherniak (1993, 1995, 2006, 2015) and Zhang et al. (2006). See text for additional discussion.

APPENDICES

APPENDIX S1: FINITE-DIFFERENCE RADIOGENIC-HEAT-PRODUCTION & LITHOSPHERIC-HEAT-CONDUCTION MODELS

Here I outline the details of the models used to generate the thermal gradients shown in Chapter 1, Figure 12. For the crust, the heat capacity and thermal diffusivity were temperature dependent, following the expressions of Whittington et al. (Whittington et al., 2009). The crustal heat capacity was further modified to account for the latent heat of crystallization following the parameterization of Stüwe (Stüwe, 1995). The solidus and liquidus were 750 and 1050°C for the upper crust, 800 and 1100°C for the middle crust, and 850 and 1150°C for the lower crust. The latent heat of crystallization was 320 J/g as recommended by Stüwe (1995). The fraction of melt was assumed to increase linearly between the solidus and liquidus. Melt transfer was not modeled. Mantle heat capacity and thermal diffusivity were temperature and pressure dependent according the parameterization of Xu et al. (2004). Partial melting was not modeled in the mantle. The density of the crust was 2700 kg/m³ and the mantle was 3300 kg/m³. Temperature at the surface was fixed at 0°C, and the base of the mantle lithosphere was 1300°C. Model resolutions were 250 m and 1.6875×10^{10} s. The model began with a 30 km thick crust and 140km thick mantle lithosphere in which the geothermal gradient was allowed to relax from an initially linear state for 100 Myr. The crust was then instantly thickened to 60 km by pure shear (new nodes were inserted at every other depth step within the crust and the temperature at these new nodes was interpolated from the adjacent nodes) and the geothermal gradient was allowed to relax for 100 Myr. The thermal gradients in Figure 11a are for $t = 40$ Myr: slightly longer

than the maximum duration of heating permissible by monazite geochronology (30 ± 8 Myr, see section 4.1.2 of Chapter 1).

Models using three different high-heat-production-rate profiles are presented: 1) a model with a homogenous heat-production rate of $2 \mu\text{W}/\text{m}^3$, 2) a model with a homogeneous heat-production rate of $3 \mu\text{W}/\text{m}^3$, and 3) a model using the average heat production profile of southeastern Madagascar from Horton et al. (Horton et al., 2016). Each of these models has a middle- to lower-crustal heat-production rate $>3\times$ the heat-production rate estimated for average cratons (Hacker, Kelemen, & Behn, 2011; Rudnick & Gao, 2013). The homogeneous $3 \mu\text{W}/\text{m}^3$ model and the Horton et al. model have middle-to-lower crustal heat-production rates slightly higher than average granite ($2.4 \mu\text{W}/\text{m}^3$) thus providing a maximum plausible heat-production rate for large portions of the crust.

APPENDIX S2: EMPLACEMENT TEMPERATURES OF THE ANOSYEN

BATHOLITH

To further investigate the role of heat advected during emplacement of the Anosyen Batholith, the emplacement temperatures of orthopyroxene-bearing granites and syenites were calculated by determining the fraction of melt as a function of temperature with the program rhyoliteMELTS (Gualda, Ghiorso, Lemons, & Carley, 2012). Seven bulk-rock compositions reported by GAF-BGR (2008) were modeled; these compositions and their corresponding sample numbers are shown in the supplementary data Table S8. They were modeled as anhydrous because of the dearth or absence of primary hydrous phases in these rocks (Paquette et al. 1994; GAF-BGR 2008). Calculations were made assuming a pressure

of 0.6 GPa. Emplacement temperatures are taken to be greater than the temperature required to produce 10 wt. % melt: $>1000^{\circ}\text{C}$ (Fig. S3).

APPENDIX S3: REFERENCE MATERIALS & REDUCTION OF LASS MONAZITE & ZIRCON DATA

Bananeira monazite was used as the primary reference material for monazite (Kylander-Clark et al., 2013; Palin et al., 2013), because it returned the most homogeneous raw values throughout all runs. Monazite 44069, Moacyr, FC-1, Trebilcock, and Manangotry monazites were run as secondary reference materials (Aleinikoff et al., 2006; Gonçalves et al., 2016; Horstwood, Foster, Parrish, Noble, & Nowell, 2003; Tomascak, Krogstad, & Walker, 1996). All monazite dates reported in this study are corrected by a factor of $-1.0 \pm 0.2\%$, based on the weighted mean offset between the LA-ICP-MS data and the reported TIMS values of FC-1, Moacyr, and 44069. Zircon 91500 (Wiedenbeck et al., 1995) was used as the primary reference material for U-Pb isotope ratios. GJ-1 zircon (Jackson, Pearson, Griffin, & Belousova, 2004) was used a secondary reference material for U-Pb analyses and the primary reference material for trace-element analyses. Plešovice zircon (Sláma et al., 2008) was used an as additional secondary reference material.

Monazite compositions measured by Agilent 7700x quadrupole ICP-MS were initially reduced assuming 12 wt. % P and then normalized to 100 wt. % total oxides of all measured elements. Monazite compositions measured by Nu AttoM ICP-MS included only lanthanide concentrations; data were reduced assuming $\text{Pr ppm} = 29,000$ (the average value returned by the former method). The logic behind this decision was that Pr concentrations vary the least among the measured lanthanides in the samples reduced by the former method.

In zircon, trace elements other than Ti were reduced assuming stoichiometric Zr as an internal standard. Ti concentrations were reduced by creating a calibration line of Ti counts per second vs. Ti concentration for GJ-1 and 91500 zircons; the calibration line was anchored to the origin. The zircon in this study had Ti concentrations 5–10 times greater than the reference materials; 2σ uncertainty in the calibration line was propagated into all unknown Ti concentrations. Ti-in-zircon temperatures were calculated using the experimental calibration of Ferry and Watson (Ferry & Watson, 2007) with $P = 0.6 \pm 0.1$ GPa and $a_{\text{TiO}_2} = 0.75 \pm 0.25$ (rutile is not present); the 2σ uncertainty in the Ti concentrations and the experimental calibration coefficients were also propagated into the calculated temperatures. Individual Ti-in-zircon temperatures have an accuracy of $\pm 60^\circ\text{C}$ (2σ).

APPENDIX S4: EXAMPLE SYSTEMS OF LINEAR EQUATIONS FOR OXYGEN ISOTOPE THERMOMETRY OF ROCKS WITH FOUR OR FIVE MINERALS

For a rock with four minerals, of which mineral “4” has the highest T_c , the set of linear equations to be used by *LinT* can be:

$$\delta^{18}\text{O}^{\text{at } T_{\text{min1}}} - (A_{\text{min4}} - A_{\text{min1}})/T^2 = \delta^{18}\text{O}^{\text{measured}}_{\text{min4}} \quad (1)$$

$$\delta^{18}\text{O}^{\text{at } T_{\text{min2}}} - (A_{\text{min4}} - A_{\text{min2}})/T^2 = \delta^{18}\text{O}^{\text{measured}}_{\text{min4}} \quad (2)$$

$$\delta^{18}\text{O}^{\text{at } T_{\text{min3}}} - (A_{\text{min4}} - A_{\text{min3}})/T^2 = \delta^{18}\text{O}^{\text{measured}}_{\text{min4}} \quad (3)$$

$$\begin{aligned} & X_{\text{min1}} * \delta^{18}\text{O}^{\text{at } T_{\text{min1}}} + X_{\text{min2}} * \delta^{18}\text{O}^{\text{at } T_{\text{min2}}} + X_{\text{min3}} * \delta^{18}\text{O}^{\text{at } T_{\text{min3}}} \\ &= X_{\text{min1}} * \delta^{18}\text{O}^{\text{measured}}_{\text{min1}} + X_{\text{min2}} * \delta^{18}\text{O}^{\text{measured}}_{\text{min2}} + X_{\text{min3}} * \delta^{18}\text{O}^{\text{measured}}_{\text{min3}} \quad (4) \end{aligned}$$

For a rock with five minerals, of which mineral “5” has the highest T_c , the set of linear equations to be used by *LinT* can be:

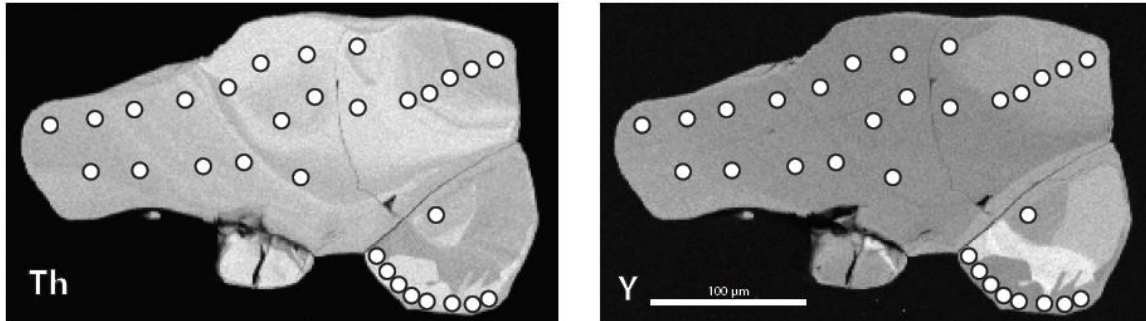
$$\delta^{18}\text{O}^{\text{at } T_{\text{min1}}} - (A_{\text{min5}} - A_{\text{min1}})/T^2 = \delta^{18}\text{O}^{\text{measured}}_{\text{min5}} \quad (1)$$

$$\delta^{18}\text{O}^{\text{at } T_{\text{min2}}} - (A_{\text{min5}} - A_{\text{min2}})/T^2 = \delta^{18}\text{O}^{\text{measured}}_{\text{min5}} \quad (2)$$

$$\delta^{18}\text{O}^{\text{at } T_{\text{min3}}} - (A_{\text{min5}} - A_{\text{min3}})/T^2 = \delta^{18}\text{O}^{\text{measured}}_{\text{min5}} \quad (3)$$

$$\delta^{18}\text{O}^{\text{at } T_{\text{min4}}} - (A_{\text{min5}} - A_{\text{min4}})/T^2 = \delta^{18}\text{O}^{\text{measured}}_{\text{min5}} \quad (4)$$

$$\begin{aligned} X_{\text{min1}} * \delta^{18}\text{O}^{\text{at } T_{\text{min1}}} + X_{\text{min2}} * \delta^{18}\text{O}^{\text{at } T_{\text{min2}}} + X_{\text{min3}} * \delta^{18}\text{O}^{\text{at } T_{\text{min3}}} \\ + X_{\text{min4}} * \delta^{18}\text{O}^{\text{at } T_{\text{min4}}} = X_{\text{min1}} * \delta^{18}\text{O}^{\text{measured}}_{\text{min1}} + X_{\text{min2}} * \delta^{18}\text{O}^{\text{measured}}_{\text{min2}} \\ + X_{\text{min3}} * \delta^{18}\text{O}^{\text{measured}}_{\text{min3}} + X_{\text{min4}} * \delta^{18}\text{O}^{\text{measured}}_{\text{min4}} \end{aligned} \quad (5)$$



monazite from leucocratic segregation in sample 23A.
 U–Pb date (all analyses) = 550 ± 6 Ma, MSWD = 1.1, n = 31 (Fig. 7g)

Figure S1. Monazite from a leucocratic segregation in sample 23A has oscillatory Th zoning and is nearly homogeneous in Y. This monazite is interpreted to have formed from crystallization of partial melt and thus provides a minimum date for the peak temperature of metamorphism. A concordia diagram of these dates is shown in Figure 7g of Chapter 1.

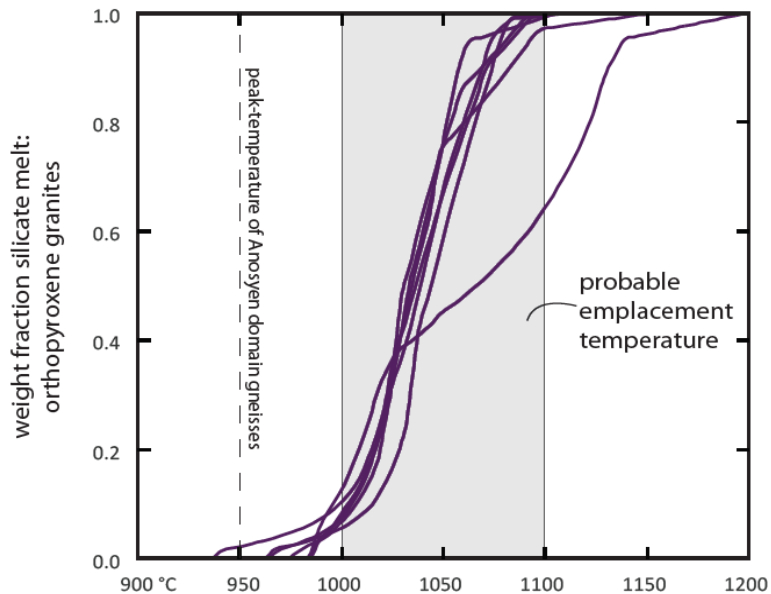


Figure S2. Weight fraction silicate melt as a function of temperature for seven orthopyroxene-bearing granitoids from the Anosyen Batholith. The granitoids were likely emplaced at temperatures $>1000^{\circ}\text{C}$, suggesting that they may have been an important heat source for metamorphism of the surrounding gneisses, which reached temperatures of $900\text{--}950^{\circ}\text{C}$. See Appendix S2 for more information about the calculations.

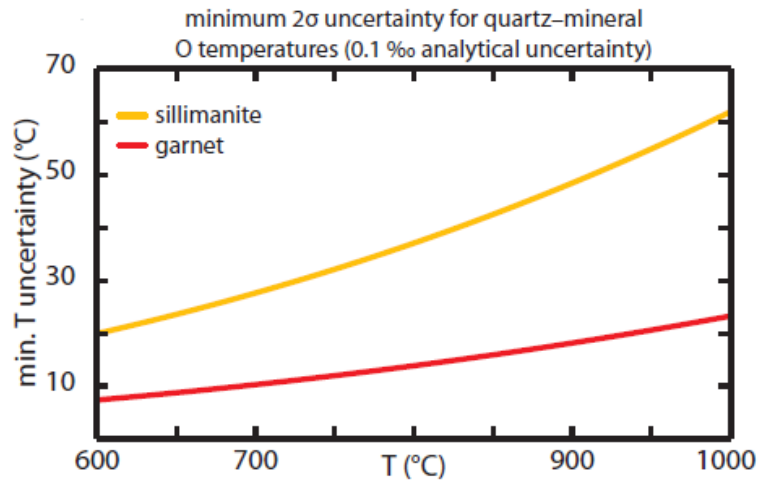


Figure S3. *LinT* (Chapter 2) will be most advantageous when applied to rocks with low-variance mineral assemblages in which the fractionation of oxygen isotopes among phases is large and there is at least one phase in which oxygen diffuses very slowly. Garnet and sillimanite are the most common phases that fit these criteria. This figure shows minimum thermometer uncertainties for quartz-garnet and quartz-sillimanite temperatures (assuming analytical uncertainties are 0.1‰ [2 σ]).

BIBLIOGRAPHY

- Ackermann, D. (1991). Kornerupine Breakdown Reactions in Paragneisses from Southern Madagascar. *Mineralogical Magazine*, 55(378), 71–80.
<https://doi.org/10.1180/minmag.1991.055.378.06>
- Aleinikoff, J. N., Schenck, W. S., Plank, M. O., Srogi, L. A., Fanning, C. M., Kamo, S. L., & Bosbyshell, H. (2006). Deciphering igneous and metamorphic events in high-grade rocks of the Wilmington complex, Delaware: Morphology, cathodoluminescence and backscattered electron zoning, and SHRIMP U-Pb geochronology of zircon and monazite. *Bulletin of the Geological Society of America*, 118(1–2), 39–64.
<https://doi.org/10.1130/B25659.1>
- Arima, M., & Gower, C. F. (1991). Osumilite-bearing granulites in the Eastern Grenville Province, eastern Labrador, Canada: Mineral parageneses and metamorphic conditions. *Journal of Petrology*, 32(1), 29–61.
<https://doi.org/https://doi.org/10.1093/petrology/32.1.29>
- Armbruster, T., & Oberhaesnsli, R. (1988). Crystal chemistry of double-ring silicates: Structural, chemical, and optical variation in osumilites. *American Mineralogist*, 73(5–6), 585–594.
- Baldwin, J. A., Powell, R., White, R. W., & Štípská, P. (2015). Using calculated chemical potential relationships to account for replacement of kyanite by symplectite in high pressure granulites. *Journal of Metamorphic Geology*, 33, 311–330.
<https://doi.org/10.1111/jmg.12122>
- Bea, F. (2012). The sources of energy for crustal melting and the geochemistry of heat-producing elements. *Lithos*, 153(2012), 278–291.
<https://doi.org/10.1016/j.lithos.2012.01.017>
- Benisek, A., Dachs, E., & Kroll, H. (2010). A ternary feldspar-mixing model based on calorimetric data: Development and application. *Contributions to Mineralogy and Petrology*, 160, 327–337. <https://doi.org/10.1007/s00410-009-0480-8>
- Benisek, A., Kroll, H., & Cemič, L. (2004). New developments in two-feldspar thermometry. *American Mineralogist*, 89(10), 1496–1504. <https://doi.org/10.2138/am-2004-1018>
- Berg, J. H., & Wheeler, E. P. (1976). Osumilite of deep-seated origin in the contact aureole of the anorthositic Nain Complex, Labrador. *American Mineralogist*, 61(1–2), 29–37.
- Blereau, E., Clark, C., Taylor, R. J. M., Johnson, T. E., Fitzsimons, I. C. W., & Santosh, M. (2016). Constraints on the timing and conditions of high-grade metamorphism, charnockite formation, and fluid-rock interaction in the Trivandrum Block, southern India. *Journal of Metamorphic Geology*, 34(6), 527–549.
<https://doi.org/10.1111/jmg.12192>
- Boger, S. D., Hirdes, W., Ferreira, C. A. M., Jenett, T., Dallwig, R., & Fanning, C. M. (2015). The 580–520 Ma Gondwana suture of Madagascar and its continuation into Antarctica and Africa. *Gondwana Research*, 28(3), 1048–1060.
<https://doi.org/10.1016/j.gr.2014.08.017>
- Boger, S. D., Hirdes, W., Ferreira, C. A. M., Schulte, B., Jenett, T., & Fanning, C. M. (2014). From passive margin to volcano–sedimentary forearc: The Tonian to Cryogenian evolution of the Anosyen Domain of southeastern Madagascar. *Precambrian Research*, 247, 159–186. <https://doi.org/10.1016/j.precamres.2014.04.004>
- Boger, S. D., White, R. W., & Schulte, B. (2012). The importance of iron speciation (Fe⁺²/Fe⁺³) in determining mineral assemblages: an example from the high-grade

- aluminous metapelites of southeastern Madagascar. *Journal of Metamorphic Geology*, 30(9), 997–1018. <https://doi.org/10.1111/jmg.12001>
- Bohlen, S. R. (1987). Pressure-Temperature-Time Paths and a Tectonic Model for the Evolution of Granulites. *The Journal of Geology*, 95(5), 617–632. <https://doi.org/10.1086/629159>
- Bonamici, C. E., Fanning, C. M., Kozdon, R., Fournelle, J. H., & Valley, J. W. (2015). Combined oxygen-isotope and U-Pb zoning studies of titanite: New criteria for age preservation. *Chemical Geology*, 398, 70–84. <https://doi.org/10.1016/j.chemgeo.2015.02.002>
- Bottinga, Y., & Javoy, M. (1973). Comments on oxygen isotope geothermometry. *Earth and Planetary Science Letters*, 20(2), 250–265. [https://doi.org/10.1016/0012-821X\(73\)90165-9](https://doi.org/10.1016/0012-821X(73)90165-9)
- Brown, M. (2006). Duality of thermal regimes is the distinctive characteristic of plate tectonics since the Neoproterozoic. *Geology*, 34(11), 961. <https://doi.org/10.1130/G22853A.1>
- Bunch, T. E., & Fuchs, L. H. (1969). Yagiite, a new sodium-magnesium analogue of osumilite. *American Mineralogist*, 54, 14–18.
- Carrington, D. P., & Harley, S. L. (1995). The Stability of Osumilite in Metapelitic Granulites. *Journal of Metamorphic Geology*, 13, 613–625. <https://doi.org/10.1111/j.1525-1314.1995.tb00246.x>
- Chambers, J. A., & Kohn, M. J. (2012). Titanium in muscovite, biotite, and hornblende: Modeling, thermometry, and rutile activities of metapelites and amphibolites. *American Mineralogist*, 97(4), 543–555. <https://doi.org/10.2138/am.2012.3890>
- Cherniak, D. J. (1993). Lead diffusion in titanite and preliminary results on the effects of radiation damage on Pb transport. *Chemical Geology*, 110, 177–194. [https://doi.org/10.1016/0009-2541\(93\)90253-F](https://doi.org/10.1016/0009-2541(93)90253-F)
- Cherniak, D. J. (1995). Sr and Nd diffusion in titanite. *Chemical Geology*, 125(3–4), 219–232. [https://doi.org/10.1016/0009-2541\(95\)00074-V](https://doi.org/10.1016/0009-2541(95)00074-V)
- Cherniak, D. J. (2006). Zr diffusion in titanite. *Contributions to Mineralogy and Petrology*, 152(5), 639–647. <https://doi.org/10.1007/s00410-006-0133-0>
- Cherniak, D. J. (2015). Nb and Ta diffusion in titanite. *Chemical Geology*, 413, 44–50. <https://doi.org/10.1016/j.chemgeo.2015.08.010>
- Cherniak, D. J., Watson, E. B., Grove, M., & Harrison, T. M. (2004). Pb diffusion in monazite: A combined RBS/SIMS study. *Geochimica et Cosmochimica Acta*, 68(4), 829–840. <https://doi.org/10.1016/j.gca.2003.07.012>
- Chinner, G. A., & Dixon, P. D. (1973). Irish osumilite. *Mineralogical Magazine*, 39(302), 189–192.
- Clark, C., Fitzsimons, I. C. W., Healy, D., & Harley, S. L. (2011). How does the continental crust get really hot? *Elements*, 7(4), 235–240. <https://doi.org/10.2113/gselements.7.4.235>
- Clark, C., Healy, D., Johnson, T., Collins, A. S., Taylor, R. J., Santosh, M., & Timms, N. E. (2015). Hot orogens and supercontinent amalgamation: A Gondwanan example from southern India. *Gondwana Research*, 28(4), 1310–1328. <https://doi.org/10.1016/j.gr.2014.11.005>
- Clayton, R. N., & Epstein, S. (1958). The Relationship between O18/O16 Ratios in Coexisting Quartz, Carbonate, and Iron Oxides from Various Geological Deposits. *The*

- Journal of Geology*, 66(4), 345–371.
- Clayton, R. N., Goldsmith, J. R., & Mayeda, T. K. (1989). Oxygen isotope fractionation in quartz, albite, anorthite and calcite. *Geochimica et Cosmochimica Acta*, 53(3), 725–733. [https://doi.org/10.1016/0016-7037\(89\)90015-X](https://doi.org/10.1016/0016-7037(89)90015-X)
- Clayton, R. N., O’Neil, J. R., & Mayeda, T. K. (1972). Oxygen isotope exchange between quartz and water. *Journal of Geophysical Research*, 77(17), 3057–3067. <https://doi.org/10.1029/JB077i017p03057>
- Collins, A. S., Kinny, P. D., & Razakamanana, T. (2012). Depositional age, provenance and metamorphic age of metasedimentary rocks from southern Madagascar. *Gondwana Research*, 21(2–3), 353–361. <https://doi.org/10.1016/j.gr.2010.12.006>
- Collins, A. S., & Windley, B. F. (2002). The Tectonic Evolution of Central and Northern Madagascar and Its Place in the Final Assembly of Gondwana. *The Journal of Geology*, 110(3), 325–339. <https://doi.org/10.1086/339535>
- Connolly, J. A. D. (2009). The geodynamic equation of state: What and how. *Geochemistry, Geophysics, Geosystems*, 10(10), 1–19. <https://doi.org/10.1029/2009GC002540>
- Corfu, F. (1996). Multistage zircon and titanite growth and inheritance in an Archean gneiss complex, Winnipeg River Subprovince, Ontario. *Earth and Planetary Science Letters*, 141, 175–186. [https://doi.org/10.1016/0012-821X\(96\)00064-7](https://doi.org/10.1016/0012-821X(96)00064-7)
- Corfu, F., Heaman, L. M., & Rogers, G. (1994). Polymetamorphic evolution of the Lewisian Complex, NW Scotland, as Recorded By U-Pb isotopic compositions of zircon, titanite and rutile. *Contributions to Mineralogy and Petrology*, 117, 215–228. <https://doi.org/10.1007/BF00310864>
- Corfu, F., & Muir, T. L. (1989). The Hemlo-Heron Bay greenstone belt and Hemlo Au-Mo deposit, Superior Province, Ontario, Canada: 2. Timing of metamorphism, alteration and Au mineralization from titanite, rutile, and monazite U–Pb geochronology. *Chemical Geology: Isotope Geoscience Section*, 79, 201–223.
- Cottle, J. M., Kylander-Clark, A. R. C., & Vrijmoed, J. C. (2012). U-Th/Pb geochronology of detrital zircon and monazite by single shot laser ablation inductively coupled plasma mass spectrometry (SS-LA-ICPMS). *Chemical Geology*, 332–333, 136–147. <https://doi.org/10.1016/j.chemgeo.2012.09.035>
- Das, K., Dasgupta, S., & Miura, H. (2001). Stability of osumilite coexisting with spinel solid solution in metapelitic granulites at high oxygen fugacity. *American Mineralogist*, 86, 1423–1434.
- Dodd, R. T., Schmus, W. R. V., & Marvin, U. B. (1965). Merrihueite, a new alkali-ferromagnesian silicate from the Mezö-Madaras Chondrite. *American Journal of Science*, 149(3687), 972–974.
- Dodson, M. H. (1973). Closure temperature in cooling geochronological and petrological systems. *Contributions to Mineralogy and Petrology*, 40(3), 259–274. <https://doi.org/10.1007/BF00373790>
- Donovan, J. J., Singer, J. W., & Armstrong, J. T. (2016). A new EPMA method for fast trace element analysis in simple matrices. *American Mineralogist*, 101(8), 1839–1853. <https://doi.org/10.2138/am-2016-5628>
- Dooley, D. F., & Patiño Douce, A. E. (1996). Fluid-absent melting of F-rich phlogopite + rutile + quartz. *American Mineralogist*, 81(1986), 202–212.
- Dyar, M. D., Lowe, E. W., Guidotti, C. V., & Delaney, J. S. (2002). Fe³⁺ and Fe²⁺ partitioning among silicates in metapelites: A synchrotron micro-XANES study.

- American Mineralogist*, 87, 514–522.
- Eiler, J. M., Baumgartner, L. P., & Valley, J. W. (1992). Intercrystalline stable isotope diffusion: a fast grain boundary model. *Contributions to Mineralogy and Petrology*, 112(1992), 543–557. <https://doi.org/10.1007/BF00310783>
- Elphick, S. C., & Graham, C. M. (1988). The effect of hydrogen on oxygen diffusion in quartz: evidence for fast proton transients? *Nature*, 335(6187), 243–245. <https://doi.org/10.1038/335243a0>
- Farquhar, J., Chacko, T., & Ellis, D. J. (1996). Preservation of oxygen isotope compositions in granulites from Northwestern Canada and Enderby Land, Antarctica: Implications for high-temperature isotopic thermometry. *Contributions to Mineralogy and Petrology*, 125(2–3), 213–224. <https://doi.org/10.1007/s004100050217>
- Farquhar, J., Chacko, T., & Frost, B. R. (1993). Strategies for high-temperature oxygen isotope thermometry: a worked example from the Laramie Anorthosite Complex, Wyoming, USA. *Earth and Planetary Science Letters*, 117(3–4), 407–422. [https://doi.org/10.1016/0012-821X\(93\)90093-O](https://doi.org/10.1016/0012-821X(93)90093-O)
- Ferry, J. M., & Watson, E. B. (2007). New thermodynamic models and revised calibrations for the Ti-in-zircon and Zr-in-rutile thermometers. *Contributions to Mineralogy and Petrology*, 154(4), 429–437. <https://doi.org/10.1007/s00410-007-0201-0>
- Finch, E. G., & Tomkins, A. G. (2017). Fluorine and chlorine behaviour during progressive dehydration melting: Consequences for granite geochemistry and metallogeny. *Journal of Metamorphic Geology*, 35, 739–757. <https://doi.org/10.1111/jmg.12253>
- Fitzsimons, I. C. W. (2016). Pan–African granulites of Madagascar and southern India: Gondwana assembly and parallels with modern Tibet. *Journal of Mineralogical and Petrological Sciences*, 111(2), 73–88. <https://doi.org/10.2465/jmps.151117>
- Franz, G., & Spear, F. S. (1985). Aluminous titanite (sphene) from the Eclogite Zone, south-central Tauern Window, Austria. *Chemical Geology*, 50, 33–46. [https://doi.org/10.1016/0009-2541\(85\)90110-X](https://doi.org/10.1016/0009-2541(85)90110-X)
- Frost, B. R., Chamberlain, K. R., & Schumacher, J. C. (2001). Sphene (titanite): Phase relations and role as a geochronometer. *Chemical Geology*, 17, 131–148. [https://doi.org/10.1016/S0009-2541\(00\)00240-0](https://doi.org/10.1016/S0009-2541(00)00240-0)
- Frost, B. R., & Frost, C. D. (2008). On charnockites. *Gondwana Research*, 13(1), 30–44. <https://doi.org/10.1016/j.gr.2007.07.006>
- Fuchs, L. H., Frondel, C., & Klein, C. J. (1966). Roedderite, a new mineral from the Indarch meteorite. *American Mineralogist*, 51, 949–955.
- Fuhrman, M. L., & Lindsley, D. H. (1988). Ternary-feldspar modeling and thermometry. *American Mineralogist*, 73, 201–215.
- GAF-BGR. (2008a). *Explanatory notes for the Anosyen Domain, southeast Madagascar*. Antananarivo: République de Madagascar, Ministère de L'énergie et des Mines (MEM/SG/DG/UCP/PGRM).
- GAF-BGR. (2008b). *Explanatory notes for the Itremo-Ikalamavony Domain, central and western Madagascar*. Réalisation des travaux de cartographie géologique de Madagascar, révision approfondie de la cartographie géologique et minière aux, 1–89.
- Gao, X.-Y., Zheng, Y.-F., Chen, Y.-X., & Guo, J. (2012). Geochemical and U–Pb age constraints on the occurrence of polygenetic titanites in UHP metagranite in the Dabie orogen. *Lithos*, 136–139, 93–108. <https://doi.org/10.1016/j.lithos.2011.03.020>
- Garber, J. M., Hacker, B. R., Kylander-Clark, A. R. C., Stearns, M. A., & Seward, G. (2017).

- Controls on trace element uptake in metamorphic titanite: Implications for petrochronology. *Journal of Petrology*, 58(6), 1031–1057. <https://doi.org/10.1093/petrology/egx046>
- Ghent, E. D., & Stout, M. Z. (1984). TiO₂ activity in metamorphosed pelitic and basic rocks: principles and applications to metamorphism in southeastern Canadian Cordillera. *Contributions to Mineralogy and Petrology*, 86(3), 248–255. <https://doi.org/10.1007/BF00373670>
- Giese, J., Berger, A., Schreurs, G., & Gnos, E. (2011). The timing of the tectono-metamorphic evolution at the Neoproterozoic–Phanerozoic boundary in central southern Madagascar. *Precambrian Research*, 185, 131–148. <https://doi.org/10.1016/j.precamres.2011.01.002>
- Giletti, B. J. (1986). Diffusion effects on oxygen isotope temperatures of slowly cooled igneous and metamorphic rocks. *Epsl*, 77(1986), 218–228.
- Glazner, A. F. (1994). Foundering of mafic plutons and density stratification of continental crust. *Geology*, 22(5), 435–438. [https://doi.org/10.1130/0091-7613\(1994\)022<0435:FOMPAD>2.3.CO](https://doi.org/10.1130/0091-7613(1994)022<0435:FOMPAD>2.3.CO)
- Gonçalves, G. O., Lana, C., Scholz, R., Buick, I. S., Gerdes, A., Kamo, S. L., ... Nalini Jr., H. A. (2016). An assessment of monazite from the Itambé pegmatite district for use as U–Pb isotope reference material for microanalysis and implications for the origin of the “Moacyr” monazite. *Chemical Geology*, 424(2016). <https://doi.org/10.1016/j.chemgeo.2015.12.019>
- Grégoire, V., Nédélec, A., Monié, P., Montel, J.-M., Ganne, J., & Ralison, B. (2009). Structural reworking and heat transfer related to the late-Panafrican Angavo shear zone of Madagascar. *Tectonophysics*, 477(3–4), 197–216. <https://doi.org/10.1016/j.tecto.2009.03.009>
- Gualda, G. A. R., Ghiorso, M. S., Lemons, R. V., & Carley, T. L. (2012). Rhyolite-MELTS: a Modified Calibration of MELTS Optimized for Silica-rich, Fluid-bearing Magmatic Systems. *Journal of Petrology*, 53(5), 875–890. <https://doi.org/10.1093/petrology/egr080>
- Guevara, V. E., & Caddick, M. J. (2016). Shooting at a moving target: Phase equilibria modelling of high-temperature metamorphism. *Journal of Metamorphic Geology*, 34(3), 209–235. <https://doi.org/10.1111/jmg.12179>
- Hacker, B. R., Gnos, E., Ratschbacher, L., Webb, L., Grove, M., McWilliams, M., ... Wu, Z. (2000). Hot and dry xenoliths from the lower crust of Tibet. *Science*, 287(March), 2463–2466.
- Hacker, B. R., Kelemen, P. B., & Behn, M. D. (2011). Differentiation of the continental crust by relamination. *Earth and Planetary Science Letters*, 307, 501–516. <https://doi.org/10.1016/j.epsl.2011.05.024>
- Hacker, B. R., Ritzwoller, M. H., & Xie, J. (2014). Partially melted, mica-bearing crust in central Tibet. *Tectonics*, 33(1), 1408–1424. <https://doi.org/10.1002/2014TC003545>
- Hagen, B., Hoernes, S., & Rötzler, J. (2008). Geothermometry of the ultrahigh-temperature Saxon granulites revisited. Part II: Thermal peak conditions and cooling rates inferred from oxygen-isotope fractionations. *European Journal of Mineralogy*, 20(6), 1117–1133. <https://doi.org/10.1127/0935-1221/2008/0020-1858>
- Harley, S. L. (2016). A matter of time: The importance of the duration of UHT metamorphism. *Journal of Mineralogical and Petrological Sciences*, 111(2), 50–72.

- <https://doi.org/10.2465/jmps.160128>
- Harlov, D. E., & Milke, R. (2002). Stability of corundum + quartz relative to kyanite and sillimanite at high temperature and pressure. *American Mineralogist*, 87(4), 424–432.
- Hayden, L. A., Watson, E. B., & Wark, D. A. (2008). A thermobarometer for sphene (titanite). *Contributions to Mineralogy and Petrology*, 155(4), 529–540. <https://doi.org/10.1007/s00410-007-0256-y>
- Hoernes, S., Hoffbauer, R., & Fiorentini, E. (1994). Oxygen isotope fractionation patterns in high-grade rocks of Sri Lanka as a key for the reconstruction of physical conditions during cooling. *Journal of the Geological Society of Sri Lanka*, 5, 59–68.
- Hoernes, S., Lichtenstein, U., Van Reenen, D. D., & Mokgatla, K. (1995). Whole-rock/mineral O-isotope fractionations as a tool to model fluid-rock interaction in deep seated shear zones of the Southern Marginal Zone of the Limpopo Belt, South Africa. *South African Journal of Geology*.
- Hoffbauer, R., Hoernes, S., & Fiorentini, E. (1994). Oxygen isotope thermometry based on a refined increment method and its application to granulite-grade rocks from Sri Lanka. *Precambrian Research*, 66(1–4), 199–220. [https://doi.org/10.1016/0301-9268\(94\)90051-5](https://doi.org/10.1016/0301-9268(94)90051-5)
- Holder, R. M., Hacker, B. R., Kylander-Clark, A. R. C., & Cottle, J. M. (2015). Monazite trace-element and isotopic signatures of (ultra)high-pressure metamorphism: Examples from the Western Gneiss Region, Norway. *Chemical Geology*, 409, 99–111. <https://doi.org/10.1016/j.chemgeo.2015.04.021>
- Holland, T. J. B., Babu, E. V. S. S. K., & Waters, D. J. (1996). Phase relations of osumilite and dehydration melting in pelitic rocks: a simple thermodynamic model for the KFMASH system. *Contributions to Mineralogy and Petrology*, 124(3–4), 383–394. <https://doi.org/10.1007/s004100050198>
- Holland, T. J. B., & Powell, R. (2011). An improved and extended internally consistent thermodynamic dataset for phases of petrological interest, involving a new equation of state for solids. *Journal of Metamorphic Geology*, 29(3), 333–383. <https://doi.org/10.1111/j.1525-1314.2010.00923.x>
- Horstwood, M. S. A., Foster, G. L., Parrish, R. R., Noble, S. R., & Nowell, G. M. (2003). Common-Pb corrected in situ U–Pb accessory mineral geochronology by LA-MC-ICP-MS. *The Royal Society of Chemistry*, 18, 837–846. <https://doi.org/10.1039/b304365g>
- Horton, F., Hacker, B. R., Kylander-Clark, A. R. C., Holder, R. M., & Jöns, N. (2016). Focused radiogenic heating of middle crust caused ultrahigh temperatures in southern Madagascar. *Tectonics*, 35, 293–314. <https://doi.org/10.1002/2015TC004040>
- Hyndman, R. D., Currie, C. A., & Mazzotti, S. P. (2005). Subduction zone backarcs, mobile belts, and orogenic heat. *GSA Today*, 15(2), 4–10. [https://doi.org/10.1130/1052-5173\(2005\)015](https://doi.org/10.1130/1052-5173(2005)015)
- Jackson, S. E., Pearson, N. J., Griffin, W. L., & Belousova, E. A. (2004). The application of laser ablation-inductively coupled plasma-mass spectrometry to in situ U–Pb zircon geochronology. *Chemical Geology*, 211(1–2), 47–69. <https://doi.org/10.1016/j.chemgeo.2004.06.017>
- Jaupart, C., Mareschal, J.-C., & Iarotsky, L. (2016). Radiogenic heat production in the continental crust. *Lithos*, 262, 398–427. <https://doi.org/10.1016/j.lithos.2016.07.017>
- Javoy, M. (1977). Stable isotopes and geothermometry. *Journal of the Geological Society*, 133(6), 609–636. <https://doi.org/10.1144/gsjgs.133.6.0609>

- Jiménez-Munt, I., Fernández, M., Vergés, J., & Platt, J. P. (2008). Lithosphere structure underneath the Tibetan Plateau inferred from elevation, gravity and geoid anomalies. *Earth and Planetary Science Letters*, 267(1–2), 276–289. <https://doi.org/10.1016/j.epsl.2007.11.045>
- Jiménez-Munt, I., & Platt, J. P. (2006). Influence of mantle dynamics on the topographic evolution of the Tibetan Plateau: Results from numerical modeling. *Tectonics*, 25(6). <https://doi.org/10.1029/2006TC001963>
- Johnson, T. E., Clark, C., Taylor, R. J. M., Santosh, M., & Collins, A. S. (2015). Prograde and retrograde growth of monazite in migmatites : An example from the Nagercoil Block , southern India. *Geoscience Frontiers*, 6(3), 373–387. <https://doi.org/10.1016/j.gsf.2014.12.003>
- Jöns, N., & Schenk, V. (2011). The ultrahigh temperature granulites of southern Madagascar in a polymetamorphic context: implications for the amalgamation of the Gondwana supercontinent. *European Journal of Mineralogy*, 23(2), 127–156. <https://doi.org/10.1127/0935-1221/2011/0023-2087>
- Kelsey, D. E. (2008). On ultrahigh-temperature crustal metamorphism. *Gondwana Research*, 13(1), 1–29. <https://doi.org/10.1016/j.gr.2007.06.001>
- Kelsey, D. E., & Hand, M. (2015). On ultrahigh temperature crustal metamorphism: Phase equilibria, trace element thermometry, bulk composition, heat sources, timescales and tectonic settings. *Geoscience Frontiers*, 6(3), 311–356. <https://doi.org/10.1016/j.gsf.2014.09.006>
- Kemp, A. I. S., Shimura, T., & Hawkesworth, C. J. (2007). Linking granulites, silicic magmatism, and crustal growth in arcs: Ion microprobe (zircon) U-Pb ages from the Hidaka metamorphic belt, Japan. *Geology*, 35(9), 807–810. <https://doi.org/10.1130/G23586A.1>
- Kilpatrick, J. A., & Ellis, D. J. (2011). C-type magmas: igneous charnockites and their extrusive equivalents. *Transactions of the Royal Society of Edinburgh: Earth Sciences*, 83(1–2), 155–164. <https://doi.org/10.1017/S0263593300007847>
- Kohn, M. J. (1999). Why most “dry” rocks should cool “wet.” *American Mineralogist*, 84(4), 570–580.
- Kohn, M. J., & Corrie, S. L. (2011). Preserved Zr-temperatures and U–Pb ages in high-grade metamorphic titanite: Evidence for a static hot channel in the Himalayan orogen. *Earth and Planetary Science Letters*, 311(1–2), 136–143. <https://doi.org/10.1016/j.epsl.2011.09.008>
- Kohn, M. J., Penniston-Dorland, S. C., & Ferreira, J. C. S. (2016). Implications of near-rim compositional zoning in rutile for geothermometry, geospeedometry, and trace element equilibration. *Contributions to Mineralogy and Petrology*. <https://doi.org/10.1007/s00410-016-1285-1>
- Kohn, M. J., & Valley, J. W. (1998). Obtaining equilibrium oxygen isotope fractionations from rocks: theory and examples. *Contributions to Mineralogy and Petrology*, 132(3), 209–224. <https://doi.org/10.1007/s004100050418>
- Korhonen, F. J., Brown, M., Clark, C., & Bhattacharya, S. (2013). Osumilite-melt interactions in ultrahigh temperature granulites: Phase equilibria modelling and implications for the P-T-t evolution of the eastern ghats province, India. *Journal of Metamorphic Geology*, 31(8), 881–907. <https://doi.org/10.1111/jmg.12049>
- Kroll, H., Evangelakakis, C., & Voll, G. (1993). Two-feldspar geothermometry: a review and

- revision for slowly cooled rocks. *Contributions to Mineralogy and Petrology*, 114(4), 510–518. <https://doi.org/10.1007/BF00321755>
- Kylander-Clark, A. R. C. (2017). Petrochronology by Laser-Ablation Inductively Coupled Plasma Mass Spectrometry. *Reviews in Mineralogy and Geochemistry*, 83, 183–196. <https://doi.org/10.2138/rmg.2017.83.6>
- Kylander-Clark, A. R. C., Hacker, B. R., & Cottle, J. M. (2013). Laser-ablation split-stream ICP petrochronology. *Chemical Geology*, 345, 99–112. <https://doi.org/10.1016/j.chemgeo.2013.02.019>
- Kylander-Clark, A. R. C., Hacker, B. R., & Mattinson, J. M. (2008). Slow exhumation of UHP terranes: Titanite and rutile ages of the Western Gneiss Region, Norway. *Earth and Planetary Science Letters*, 272(3–4), 531–540. <https://doi.org/10.1016/j.epsl.2008.05.019>
- Liang, X., Sandvol, E., Chen, Y. J., Hearn, T., Ni, J., Klemperer, S., ... Tilmann, F. (2012). A complex Tibetan upper mantle: A fragmented Indian slab and no south-verging subduction of Eurasian lithosphere. *Earth and Planetary Science Letters*, 333–334, 101–111. <https://doi.org/10.1016/j.epsl.2012.03.036>
- Lin, T. H., & Yund, R. A. (1972). Potassium and sodium self-diffusion in alkali feldspar. *Contributions to Mineralogy and Petrology*, 34(3), 177–184. <https://doi.org/10.1007/BF00373289>
- Lucassen, F., Franz, G., & Rhede, D. (2012). Small-scale transport of trace elements Nb and Cr during growth of titanite: An experimental study at 600 °C, 0.4 GPa. *Contributions to Mineralogy and Petrology*, 164(6), 987–997. <https://doi.org/10.1007/s00410-012-0784-y>
- Lucassen, F., Franz, G., Rhede, D., & Wirth, R. (2010). Ti-Al zoning of experimentally grown titanite in the system CaO-Al₂O₃-TiO₂-SiO₂-NaCl-H₂O-(F): Evidence for small-scale fluid heterogeneity. *American Mineralogist*, 95(10), 1365–1378. <https://doi.org/10.2138/am.2010.3518>
- Marsh, J. H., & Smye, A. J. (2017). U-Pb systematics and trace element characteristics in titanite from a high-pressure mafic granulite. *Chemical Geology*, 466(June), 403–416. <https://doi.org/10.1016/j.chemgeo.2017.06.029>
- Martelat, J.-E., Lardeaux, J.-M., Nicollet, C., & Rakotondrazafy, R. (2000). Strain pattern and late Precambrian deformation history in southern Madagascar. *Precambrian Research*, 102(1–2), 1–20. [https://doi.org/10.1016/S0301-9268\(99\)00083-2](https://doi.org/10.1016/S0301-9268(99)00083-2)
- Martelat, J.-E., Malamoud, K., Cordier, P., Randrianasolo, B., Schulmann, K., & Lardeaux, J.-M. (2012). Garnet crystal plasticity in the continental crust, new example from south Madagascar. *Journal of Metamorphic Geology*, 30(4), 435–452. <https://doi.org/10.1111/j.1525-1314.2012.00974.x>
- Martelat, J.-E., Randrianasolo, B., Schulmann, K., Lardeaux, J.-M., & Devidal, J.-L. (2014). Airborne magnetic data compared to petrology of crustal scale shear zones from southern Madagascar: A tool for deciphering magma and fluid transfer in orogenic crust. *Journal of African Earth Sciences*, 94, 74–85. <https://doi.org/10.1016/j.jafrearsci.2013.07.003>
- Mattinson, J. M. (1978). Age, origin, and thermal histories of some plutonic rocks from the Salinian block of California. *Contributions to Mineralogy and Petrology*, 67(3), 233–245. <https://doi.org/10.1007/BF00381451>
- Mattinson, J. M. (2005). Zircon U–Pb chemical abrasion (“CA-TIMS”) method: Combined

- annealing and multi-step partial dissolution analysis for improved precision and accuracy of zircon ages. *Chemical Geology*, 220(1–2), 47–66.
<https://doi.org/10.1016/j.chemgeo.2005.03.011>
- McDonough, W. F., & Sun, S. -s. (1995). The composition of the Earth. *Chemical Geology*, 120(3–4), 223–253. [https://doi.org/10.1016/0009-2541\(94\)00140-4](https://doi.org/10.1016/0009-2541(94)00140-4)
- McFarlane, C. R. M., & Harrison, T. M. (2006). Pb-diffusion in monazite: Constraints from a high-T contact aureole setting. *Earth and Planetary Science Letters*, 250, 376–384.
<https://doi.org/10.1016/j.epsl.2006.06.050>
- McNamara, D. E., Walter, W. R., Owens, T. J., & Ammon, C. J. (1997). Upper mantle velocity structure beneath the Tibetan Plateau from Pn travel time tomography. *Journal of Geophysical Research*, 102(B1), 493–505. <https://doi.org/10.1029/96JB02112>
- Meert, J. G., & Lieberman, B. S. (2008). The Neoproterozoic assembly of Gondwana and its relationship to the Ediacaran-Cambrian radiation. *Gondwana Research*, 14(1–2), 5–21.
<https://doi.org/10.1016/j.gr.2007.06.007>
- Mezger, K., Essene, E. J., van der Pluijm, B. A., & Halliday, A. N. (1993). U-Pb geochronology of the Grenville Orogen of Ontario and New York: constraints on ancient crustal tectonics. *Contributions to Mineralogy and Petrology*, 114(1), 13–26.
<https://doi.org/10.1007/BF00307862>
- Mezger, K., Rawnsley, C. M., Bohlen, S. R., & Hanson, G. N. (1991). U-Pb Garnet, Spinel, Monazite, and Rutile Ages: Implications for the Duration of High-Grade Metamorphism and Cooling Histories, Adirondack Mts., New York. *Journal of Geology*, 99(3), 415–428. <https://doi.org/10.1086/629503>
- Migdisov, A. A., Williams-Jones, A. E., & Wagner, T. (2009). An experimental study of the solubility and speciation of the Rare Earth Elements (III) in fluoride- and chloride-bearing aqueous solutions at temperatures up to 300 °C. *Geochimica et Cosmochimica Acta*, 73(23), 7087–7109. <https://doi.org/10.1016/j.gca.2009.08.023>
- Molnar, P., England, P., & Martinod, J. (1993). Mantle dynamics, uplift of the Tibetan plateau, and the Indian monsoon. *Reviews of Geophysics*, 31(4), 357–396. Retrieved from <http://www.agu.org/pubs/crossref/1993/93RG02030.shtml>
- Montel, J.-M., Razafimahatratra, D., de Parseval, P., Poitrasson, F., Moine, B., Seydoux-Guillaume, A.-M., ... Gibert, F. (2018). The giant monazite crystals from Manangotry (Madagascar). *Chemical Geology*, 484, 36–50.
<https://doi.org/10.1016/j.chemgeo.2017.10.034>
- Motoyoshi, Y., & Hensen, B. J. (2001). F-rich phlogopite stability in ultra-high-temperature metapelites from the Napier Complex, East Antarctica. *American Mineralogist*, 86, 1404–1413.
- Mottram, C. M., Warren, C. J., Regis, D., Roberts, N. M. W., Harris, N. B. W., Argles, T. W., & Parrish, R. R. (2014). Developing an inverted barrovian sequence; insights from monazite petrochronology. *Earth and Planetary Science Letters*, 403, 418–431.
<https://doi.org/10.1016/j.epsl.2014.07.006>
- Nabelek, P. I., Whittington, A. G., & Hofmeister, A. M. (2010). Strain heating as a mechanism for partial melting and ultrahigh temperature metamorphism in convergent orogens: Implications of temperature-dependent thermal diffusivity and rheology. *Journal of Geophysical Research: Solid Earth*, 115(12), 1–17.
<https://doi.org/10.1029/2010JB007727>
- Nelson, K. D., Zhao, W., Brown, L. D., Kuo, J., Che, J., Liu, X., ... Edwards, M. (1996).

- Partially Molten Middle Crust Beneath Southern Tibet: Synthesis of Project INDEPTH Results. *Science*, 274, 1684–1688. <https://doi.org/10.1126/science.274.5293.1684>
- Nichols, G. T., Berry, R. F., & Green, D. H. (1992). Internally consistent gahnitic spinel-cordierite-garnet equilibria in the FMASHZn system: geothermobarometry and applications. *Contributions to Mineralogy and Petrology*, 111(3), 362–377. <https://doi.org/10.1007/BF00311197>
- Nicollet, C. (1985). Les gneiss rubanés à cordiérite et grenat d'ihosy: Un marqueur thermobarométrique dans le sud de Madagascar. *Precambrian Research*, 28(2), 175–185. [https://doi.org/10.1016/0301-9268\(85\)90079-8](https://doi.org/10.1016/0301-9268(85)90079-8)
- O'Neil, J., & Taylor, H. (1967). The oxygen isotope and cation exchange chemistry of feldspars. *American Mineralogist*, 52, 1414–1437. Retrieved from <http://www.bcin.ca/Interface/openbcin.cgi?submit=submit&Chinkey=34397>
- Oberti, R., Smith, D. C., Rossi, G., & Caucia, F. (1991). The crystal-chemistry of high-aluminium titanites. *European Journal of Mineralogy*, 3(5), 777–792. <https://doi.org/10.1127/ejm/3/5/0777>
- Olsen, E. (1967). A new Occurrence of Roedderite and its Bearing on Osumilite-Type Minerals. *American Mineralogist*, 52, 1519–1523.
- Olsen, E., & Bunch, T. E. (1970). Compositions of Natural Osumilites. *American Mineralogist*, 55, 875–879.
- Palin, R. M., Searle, M. P., Waters, D. J., Parrish, R. R., Roberts, N. M. W., Horstwood, M. S. A., ... Anh, T. T. (2013). A geochronological and petrological study of anatectic paragneiss and associated granite dykes from the Day Nui Con Voi metamorphic core complex, North Vietnam: Constraints on the timing of metamorphism within the Red River shear zone. *Journal of Metamorphic Geology*, 31(4), 359–387. <https://doi.org/10.1111/jmg.12025>
- Paquette, J.-L., Nédélec, A., Moine, B., & Rakotondrazafy, A. F. M. (1994). U-Pb, Single Zircon Pb-Evaporation, and Sm-Nd Isotopic Study of a Granulite Domain in SE Madagascar. *The Journal of Geology*, 102(5), 523–538. <https://doi.org/10.1086/629696>
- Paton, C., Hellstrom, J., Paul, B., Woodhead, J., & Hergt, J. (2011). Iolite: Freeware for the visualisation and processing of mass spectrometric data. *Journal of Analytical Atomic Spectrometry*, 26(12), 2508. <https://doi.org/10.1039/c1ja10172b>
- Peacock, S. M. (1989). Thermal modeling of metamorphic pressure-temperature-time paths: A forward approach. In F. S. Spear & S. M. Peacock (Eds.), *Metamorphic Pressure-Temperature-Time Paths* (pp. 57–102). Washington, D. C.: American Geophysical Union. <https://doi.org/10.1029/SC007p0057>
- Pidgeon, R. T., Bosch, D., & Bruguier, O. (1996). Inherited zircon and titanite U–Pb systems in an Archean syenite from southwestern Australia: implications for U–Pb stability of titanite. *Earth and Planetary Science Letters*, 141, 187–198. [https://doi.org/10.1016/0012-821X\(95\)00237-7](https://doi.org/10.1016/0012-821X(95)00237-7)
- Pili, É., Ricard, Y., Lardeaux, J.-M., & Sheppard, S. M. F. (1997). Lithospheric shear zones and mantle-crust connections. *Tectonophysics*, 280(1–2), 15–29. [https://doi.org/10.1016/S0040-1951\(97\)00142-X](https://doi.org/10.1016/S0040-1951(97)00142-X)
- Pili, É., Sheppard, S. M. F., Lardeaux, J.-M., Martelat, J.-E., & Nicollet, C. (1997). Fluid flow vs. scale of shear zones in the lower continental crust and the granulite paradox. *Geology*, 25(1), 15–18. [https://doi.org/10.1130/0091-7613\(1997\)025<0015:FFVSOS>2.3.CO;2](https://doi.org/10.1130/0091-7613(1997)025<0015:FFVSOS>2.3.CO;2)

- Porter, D. A., & Easterling, K. E. (1990). Diffusion. In *Phase Transformations in Metals and Alloys* (pp. 60–109). New York: Chapman and Hall.
- Pownall, J. M. (2014). Earth's youngest known ultrahigh-temperature granulites discovered on Seram, Eastern Indonesia. *Geology*, *42*(4), 279–282. <https://doi.org/10.1130/G35230.1>
- Prowatke, S., & Klemme, S. (2005). Effect of melt composition on the partitioning of trace elements between titanite and silicate melt. *Geochimica et Cosmochimica Acta*, *69*(3), 695–709. <https://doi.org/10.1016/j.gca.2004.06.037>
- Putnis, A. (2009). Mineral Replacement Reactions. *Reviews in Mineralogy and Geochemistry*, *70*(1), 87–124. <https://doi.org/10.2138/rmg.2009.70.3>
- Raith, M. M., Rakotondrazafy, R., & Sengupta, P. (2008). Petrology of corundum-spinel-sapphirine-anorthite rocks (sakenites) from the type locality in southern Madagascar. *Journal of Metamorphic Geology*, *26*(6), 647–667. <https://doi.org/10.1111/j.1525-1314.2008.00779.x>
- Rakotonandrasana, N. O. T., Arima, M., Miyawaki, R., & Rambelison, R. A. (2010). Widespread Occurrences of Highbomite-2N2S in UHT Metapelites from the Betroka Belt, Southern Madagascar: Implications on Melt or Fluid Activity during Regional Metamorphism. *Journal of Petrology*, *51*(4), 869–895. <https://doi.org/10.1093/petrology/egq004>
- Rakotondrazafy, A. F. M., Moine, B., & Cuney, M. (1996). Mode of formation of hibonite (CaAl₁₂O₁₉) within the U-Th skarns from the granulites of S-E Madagascar. *Contributions to Mineralogy and Petrology*, *123*(2), 190–201. <https://doi.org/10.1007/s004100050150>
- Rapp, J. F., Klemme, S., Butler, I. B., & Harley, S. L. (2010). Extremely high solubility of rutile in chloride and fluoride-bearing metamorphic fluids: An experimental investigation. *Geology*, *38*(4), 323–326. <https://doi.org/10.1130/G30753.1>
- Rubatto, D., Hermann, J., & Buick, I. S. (2006). Temperature and bulk composition control on the growth of monazite and zircon during low-pressure anatexis (Mount Stafford, Central Australia). *Journal of Petrology*, *47*(10), 1973–1996. <https://doi.org/10.1093/petrology/egl033>
- Rudnick, R. L., & Gao, S. (2013). Composition of the Continental Crust. In *Treatise on Geochemistry: Second Edition*. <https://doi.org/10.1016/B978-0-08-095975-7.00301-6>
- Rumble, D. (1978). Mineralogy, petrology, and oxygen isotopic geochemistry of the Clough Formation, Mountain, W. New Hampshire, USA. *Journal of Petrology*, *19*, 317–340.
- Sandiford, M., & McLaren, S. (2002). Tectonic feedback and the ordering of heat producing elements within the continental lithosphere. *Earth and Planetary Science Letters*, *204*(1–2), 133–150. [https://doi.org/10.1016/S0012-821X\(02\)00958-5](https://doi.org/10.1016/S0012-821X(02)00958-5)
- Sandiford, M., McLaren, S., & Neumann, N. (2002). Long-term thermal consequences of the redistribution of heat-producing elements associated with large-scale granitic complexes. *Journal of Metamorphic Geology*, *20*(1), 87–98. <https://doi.org/10.1046/j.0263-4929.2001.00359.x>
- Sandiford, M., & Powell, R. (1986). Deep crustal metamorphism during crustal extension: modern and ancient examples. *Earth and Planetary Science Letters*, *79*, 151–158. [https://doi.org/10.1016/0012-821X\(86\)90048-8](https://doi.org/10.1016/0012-821X(86)90048-8)
- Sawyer, E. W., Cesare, B., & Brown, M. (2011). When the continental crust melts. *Elements*, *7*(4), 229–234. <https://doi.org/10.2113/gselements.7.4.229>

- Schärer, U., Zhang, L.-S., & Tapponnier, P. (1994). Duration of strike-slip movements in large shear zones: The Red River belt, China. *Earth and Planetary Science Letters*. [https://doi.org/10.1016/0012-821X\(94\)90119-8](https://doi.org/10.1016/0012-821X(94)90119-8)
- Schorn, S., & Diener, J. F. A. (2017). Details of the gabbro-to-eclogite transition determined from microtextures and calculated chemical potential relationships. *Journal of Metamorphic Geology*, *35*(1), 55–75. <https://doi.org/10.1111/jmg.12220>
- Scott, D. J., & St-Onge, M. R. (1995). Constraints on Pb closure temperature in titanite based on rocks from the Ungava orogen, Canada: Implications for U-Pb geochronology and P-T-t path determinations. *Geology*, *23*, 1123–1126.
- Sharp, Z. (1990). A laser-based microanalytical method for the in situ determination of oxygen isotope ratios of silicates and oxides. *Geochimica et Cosmochimica Acta*, *54*, 1353–1357. Retrieved from <http://www.sciencedirect.com/science/article/pii/001670379090160M>
- Sharp, Z. D. (1991). Determination of oxygen diffusion rates in magnetite from natural isotopic variations. *Geology*, *19*(6), 653–656. [https://doi.org/10.1130/0091-7613\(1991\)019<0653:DOODRI>2.3.CO](https://doi.org/10.1130/0091-7613(1991)019<0653:DOODRI>2.3.CO)
- Sharp, Z. D. (1995). Oxygen isotope geochemistry of the Al₂SiO₅ polymorphs. *American Journal of Science*, *295*(9), 1058–1076. <https://doi.org/10.2475/ajs.295.9.1058>
- Sharp, Z. D., Giletti, B. J., & Yoder, H. S. (1991). Oxygen diffusion rates in quartz exchanged with CO₂. *Earth and Planetary Science Letters*, *107*(2), 339–348. [https://doi.org/10.1016/0012-821X\(91\)90081-R](https://doi.org/10.1016/0012-821X(91)90081-R)
- Sláma, J., Košler, J., Condon, D. J., Crowley, J. L., Gerdes, A., Hanchar, J. M., ... Whitehouse, M. J. (2008). Plešovice zircon — A new natural reference material for U–Pb and Hf isotopic microanalysis. *Chemical Geology*, *249*(1–2), 1–35. <https://doi.org/10.1016/j.chemgeo.2007.11.005>
- Smit, M. A., Scherer, E. E., & Mezger, K. (2013). Lu–Hf and Sm–Nd garnet geochronology: Chronometric closure and implications for dating petrological processes. *Earth and Planetary Science Letters*, *381*, 222–233. <https://doi.org/10.1016/j.epsl.2013.08.046>
- Spandler, C., Hammerli, J., Sha, P., Hilbert-Wolf, H., Hu, Y., Roberts, E., & Schmitz, M. (2016). MKED1: A new titanite standard for in situ analysis of Sm–Nd isotopes and U–Pb geochronology. *Chemical Geology*, *425*, 110–126. <https://doi.org/10.1016/j.chemgeo.2016.01.002>
- Spear, F. S. (2010). Monazite-allanite phase relations in metapelites. *Chemical Geology*, *279*(1–2), 55–62. <https://doi.org/10.1016/j.chemgeo.2010.10.004>
- Spencer, K. J., Hacker, B. R., Kylander-Clark, A. R. C., Andersen, T. B., Cottle, J. M., Stearns, M. A., ... Seward, G. G. E. (2013). Campaign-style titanite U–Pb dating by laser-ablation ICP: Implications for crustal flow, phase transformations and titanite closure. *Chemical Geology*, *341*, 84–101. <https://doi.org/10.1016/j.chemgeo.2012.11.012>
- Stacey, J. S., & Kramers, J. D. (1975). Approximation of terrestrial lead isotope evolution by a two-stage model. *Earth and Planetary Science Letters*, *26*(2), 207–221. [https://doi.org/10.1016/0012-821X\(75\)90088-6](https://doi.org/10.1016/0012-821X(75)90088-6)
- Stearns, M. A., Cottle, J. M., Hacker, B. R., & Kylander-Clark, A. R. C. (2016). Extracting thermal histories from the near-rim zoning in titanite using coupled U–Pb and trace-element depth profiles by single-shot laser-ablation split stream (SS-LASS) ICP-MS. *Chemical Geology*, *422*(2016), 13–24. <https://doi.org/10.1016/j.chemgeo.2015.12.011>

- Stearns, M. A., Hacker, B. R., Ratschbacher, L., Lee, J., Cottle, J. M., & Kylander-Clark, A. R. C. (2013). Synchronous Oligocene-Miocene metamorphism of the Pamir and the north Himalaya driven by plate-scale dynamics. *Geology*, *41*(10), 1071–1074. <https://doi.org/10.1130/G34451.1>
- Stearns, M. A., Hacker, B. R., Ratschbacher, L., Rutte, D., & Kylander-Clark, A. R. C. (2015). Titanite petrochronology of the Pamir gneiss domes: Implications for middle to deep crust exhumation and titanite closure to Pb and Zr diffusion. *Tectonics*, *34*(4), 784–802. <https://doi.org/10.1002/2014TC003774>
- Stepanov, A. S., Hermann, J., Rubatto, D., & Rapp, R. P. (2012). Experimental study of monazite/melt partitioning with implications for the REE, Th and U geochemistry of crustal rocks. *Chemical Geology*, *300–301*, 200–220. <https://doi.org/10.1016/j.chemgeo.2012.01.007>
- Štípská, P., Powell, R., Hacker, B. R., Holder, R. M., & Kylander-Clark, A. R. C. (2016). Uncoupled U/Pb and REE response in zircon during the transformation of eclogite to mafic and intermediate granulite (Blanský les, Bohemian Massif). *Journal of Metamorphic Geology*, *34*(6). <https://doi.org/10.1111/jmg.12193>
- Štípská, P., Powell, R., & Racek, M. (2014). Rare eclogite-mafic granulite in felsic granulite in Blanský les: precursor of intermediate granulite in the Bohemian Massif? *Journal of Metamorphic Geology*, *32*(4), 325–345. <https://doi.org/10.1111/jmg.12075>
- Štípská, P., Powell, R., Racek, M., & Lexa, O. (2014). Intermediate granulite produced by transformation of eclogite at a felsic granulite contact, in Blanský les, Bohemian Massif. *Journal of Metamorphic Geology*, *32*(4), 347–370. <https://doi.org/10.1111/jmg.12079>
- Štípská, P., Powell, R., White, R. W., & Baldwin, J. A. (2010). Using calculated chemical potential relationships to account for coronas around kyanite: An example from the Bohemian Massif. *Journal of Metamorphic Geology*, *28*(1), 97–116. <https://doi.org/10.1111/j.1525-1314.2009.00857.x>
- Stüwe, K. (1995). Thermal buffering effects at the solidus. Implications for the equilibration of partially melted metamorphic rocks. *Tectonophysics*, *248*(1–2), 39–51. [https://doi.org/10.1016/0040-1951\(94\)00282-E](https://doi.org/10.1016/0040-1951(94)00282-E)
- Taylor, H. P. J., Albee, A. L., & Epstein, S. (1963). 18O /16O ratios of coexisting minerals in three assemblages of kyanite-zone pelitic schist. *J. Geology*, *71*(4), 513–522.
- Taylor, R. J. M., Clark, C., Fitzsimons, I. C. W., Santosh, M., Hand, M., Evans, N., & McDonald, B. (2014). Post-peak, fluid-mediated modification of granulite facies zircon and monazite in the Trivandrum Block, southern India. *Contributions to Mineralogy and Petrology*, *168*(2), 1–17. <https://doi.org/10.1007/s00410-014-1044-0>
- Tomascak, P. B., Krogstad, E. J., & Walker, R. J. (1996). U-Pb Monazite Geochronology of Granitic Rocks from Maine : Implications for Late Paleozoic Tectonics in the Northern Appalachians. *The Journal of Geology*, *104*, 185–195.
- Tucker, R. D., Krogh, T. E., & Råheim, A. (1990). Proterozoic Evolution and Age-Province Boundaries in the Central Part of the Western Gneiss Region, Norway: Results of U-Pb Dating of Accessory Minerals from Trondheimsfjord to Geiranger. In C. F. Gower, T. Rivers, & B. Ryan (Eds.), *Mid-Proterozoic Laurentia-Baltica 38* (pp. 149–173). St. Johns (Newfoundland): Geological Association of Canada.
- Tucker, R. D., Råheim, A., Krogh, T. E., & Corfu, F. (1987). Uranium-lead zircon and titanite ages from the northern portion of the Western Gneiss Region, south-central Norway. *Earth and Planetary Science Letters*, *81*, 203–211.

- [https://doi.org/10.1016/0012-821X\(87\)90156-7](https://doi.org/10.1016/0012-821X(87)90156-7)
- Tucker, R. D., Robinson, P., Solli, A., Gee, D. G., Thorsnes, T., Krogh, T. E., ... Bickford, M. E. (2004). Thrusting and extension in the Scandian hinterland, Norway: New U-Pb ages and tectonostratigraphic evidence. *American Journal of Science*, 304(June), 477–532. <https://doi.org/10.2475/03.2011.01>
- Tucker, R. D., Roig, J.-Y., Delor, C., Amelin, Y., Goncalves, P., Rabarimanana, M. H., ... Belcher, R. W. (2011). Neoproterozoic extension in the Greater Dharwar Craton: a reevaluation of the “Betsimisaraka suture” in Madagascar. *Canadian Journal of Earth Sciences*, 48(2), 389–417. <https://doi.org/10.1139/E10-034>
- Tucker, R. D., Roig, J. Y., Macey, P. H., Delor, C., Amelin, Y., Armstrong, R. a., ... Ralison, A. V. (2011). A new geological framework for south-central Madagascar, and its relevance to the “out-of-Africa” hypothesis. *Precambrian Research*, 185(3–4), 109–130. <https://doi.org/10.1016/j.precamres.2010.12.008>
- Tucker, R. D., Roig, J. Y., Moine, B., Delor, C., & Peters, S. G. (2014). A geological synthesis of the Precambrian shield in Madagascar. *Journal of African Earth Sciences*, 94, 9–30. <https://doi.org/10.1016/j.jafrearsci.2014.02.001>
- Tunini, L., Jiménez-Munt, I., Fernandez, M., Vergés, J., Villaseñor, A., Melchiorre, M., & Afonso, J. C. (2016). Geophysical-petrological model of the crust and upper mantle in the India-Eurasia collision zone. *Tectonics*, 35(7), 1642–1669. <https://doi.org/10.1002/2016TC004161>
- Urey, H. C. (1947). The thermodynamic properties of isotopic substances. *Journal of the Chemical Society*, 562–581. Retrieved from <http://www.ncbi.nlm.nih.gov/pubmed/20249764>
- Urey, H. C., Lowenstam, H. A., Epstein, S., & McKinney, C. R. (1951). Measurement of Paleotemperatures and Temperatures and the Southeastern United States. *Bulletin of the Geological Society of America*, 62(April 1951), 399–416. [https://doi.org/10.1130/0016-7606\(1951\)62](https://doi.org/10.1130/0016-7606(1951)62)
- Valley, J. W. (2003). Oxygen Isotopes in Zircon. *Reviews in Mineralogy and Geochemistry*, 53(1), 343–385. <https://doi.org/10.2113/0530343>
- Valley, J. W., Bindeman, I. N., & Peck, W. H. (2003). Empirical calibration of oxygen isotope fractionation in zircon. *Geochimica et Cosmochimica Acta*. [https://doi.org/10.1016/S0016-7037\(00\)00090-5](https://doi.org/10.1016/S0016-7037(00)00090-5)
- Verts, L. A., Chamberlain, K. R., & Frost, C. D. (1996). U-Pb sphene dating of metamorphism: the importance of sphene growth in the contact aureole of the Red Mountain pluton, Laramie Mountains, Wyoming. *Contributions to Mineralogy and Petrology*, 125, 186–199. <https://doi.org/10.1007/s004100050215>
- Viete, D. R., Kylander-Clark, A. R. C., & Hacker, B. R. (2015). Single-shot laser ablation split stream (SS-LASS) petrochronology deciphers multiple, short-duration metamorphic events. *Chemical Geology*, 415, 70–86. <https://doi.org/10.1016/j.chemgeo.2015.09.013>
- Walters, J. B., & Kohn, M. J. (2017). Protracted thrusting followed by late rapid cooling of the Greater Himalayan Sequence, Annapurna Himalaya, Central Nepal: Insights from titanite petrochronology. *Journal of Metamorphic Geology*, 35(8), 897–917. <https://doi.org/10.1111/jmg.12260>
- Watson, E. B., & Cherniak, D. J. (2015). Quantitative cooling histories from stranded diffusion profiles. *Contributions to Mineralogy and Petrology*, 169(6), 1–14.

- <https://doi.org/10.1007/s00410-015-1153-4>
- Wendt, I., & Carl, C. (1991). The statistical distribution of the mean squared weighted deviation. *Chemical Geology: Isotope Geoscience Section*, 86(4), 275–285. [https://doi.org/10.1016/0168-9622\(91\)90010-T](https://doi.org/10.1016/0168-9622(91)90010-T)
- White, R. W., Powell, R., & Baldwin, J. A. (2008). Calculated phase equilibria involving chemical potentials to investigate the textural evolution of metamorphic rocks. *Journal of Metamorphic Geology*, 26(2), 181–198. <https://doi.org/10.1111/j.1525-1314.2008.00764.x>
- White, R. W., Powell, R., & Clarke, G. L. (2002). The interpretation of reaction textures in Fe-rich metapelitic granulites of the Musgrave Block, Central Australia: Constraints from mineral equilibria calculations in the system. *Journal of Metamorphic Geology*, 20(1), 41–55. <https://doi.org/10.1046/j.0263-4929.2001.00349.x>
- White, R. W., Powell, R., & Holland, T. J. B. (2007). Progress relating to calculation of partial melting equilibria for metapelites. *Journal of Metamorphic Geology*, 25(5), 511–527. <https://doi.org/10.1111/j.1525-1314.2007.00711.x>
- White, R. W., Powell, R., Holland, T. J. B., Johnson, T. E., & Green, E. C. R. (2014). New mineral activity-composition relations for thermodynamic calculations in metapelitic systems. *Journal of Metamorphic Geology*, 32(3), 261–286. <https://doi.org/10.1111/jmg.12071>
- White, R. W., Powell, R., Holland, T. J. B., & Worley, B. (2000). The effect of TiO₂ and Fe₂O₃ on metapelitic assemblages at greenschist and amphibolite facies conditions: mineral equilibria calculations in the system K₂O–FeO–MgO–Al₂O₃–SiO₂–H₂O–TiO₂–Fe₂O₃. *Journal of Metamorphic Geology*, 18, 497–511.
- White, R. W., Powell, R., & Johnson, T. E. (2014). The effect of Mn on mineral stability in metapelites revisited: New a-x relations for manganese-bearing minerals. *Journal of Metamorphic Geology*, 32(8), 809–828. <https://doi.org/10.1111/jmg.12095>
- Whittington, A. G., Hofmeister, A. M., & Nabelek, P. I. (2009). Temperature-dependent thermal diffusivity of the Earth’s crust and implications for magmatism. *Nature*, 458, 319–321. <https://doi.org/10.1038/nature07818>
- Wiedenbeck, M., Allé, P., Corfu, F., Griffin, W. L., Meier, M., Oberli, F., ... Spiegel, W. (1995). Three natural zircon standards for U-Th-Pb, Lu-Hf, trace-element and REE analyses. *Geostandards and Geoanalytical Research*, 19(1), 1–23. <https://doi.org/10.1111/j.1751-908X.1995.tb00147.x>
- Williams-Jones, A. E., Migdisov, A. A., & Samson, I. M. (2012). Hydrothermal mobilisation of the rare earth elements—a tale of “ceria” and “yttria.” *Elements*, 8(5), 355–360. <https://doi.org/10.2113/gselements.8.5.355>
- Xu, Y., Shankland, T. J., Linhardt, S., Rubie, D. C., Langenhorst, F., & Klasinski, K. (2004). Thermal diffusivity and conductivity of olivine, wadsleyite and ringwoodite to 20 GPa and 1373 K. *Physics of the Earth and Planetary Interiors*, 143(1–2), 321–336. <https://doi.org/10.1016/j.pepi.2004.03.005>
- Yund, R. A., & Tullis, J. (1980). The Effect of Water, Pressure, and Strain on Al/Si Order-Disorder Kinetics in Feldspar. *Contributions to Mineralogy and Petrology*, 72(297).
- Zhang, L.-S., & Schärer, U. (1996). Inherited Pb components in magmatic titanite and their consequence for the interpretation of U–Pb ages. *Earth and Planetary Science Letters*, 138, 57–65.
- Zheng, Y. F., & Fu, B. (1998). Estimation of oxygen diffusivity from anion porosity in

minerals. *Geochemical Journal*, 32(2), 71–89. <https://doi.org/10.2343/geochemj.32.71>